ABSTRACT

Title of dissertation:	STRUCTURE OF Fe ISOTOPES AT THE LIMITS OF THE *pf* SHELL
	Nathan Hoteling Doctor of Philosophy, 2008
Dissertation directed by:	Professor William B. Walters Department of Chemistry and Biochemistry

An investigation of the structure of Fe isotopes up to neutron number 40 has been carried out at Argonne National Laboratory with the application of a thick-target deep-inelastic reaction experiment. A beam of 450 MeV ^{64}Ni was incident on a 55 mg/cm^2 target of enriched ^{238}U located at the center of the Gammasphere spectrometer. Triple coincidence data obtained from the experiment were sorted into four time-correlated cubes and used to identify new levels in ^{61,62,64}Fe. Angular correlations were used to both confirm previously-assigned spin and parity assignments and to assign values to excited states established in this work for the first time. The effect of $g_{9/2}$ neutron excitations on the structure of low-lying yrast states in these isotopes was studied with a comparison of experimental levels with the results from shell model calculations within both pf and truncated pfg configuration spaces. The effective interactions used in this work were derived from the N3LO nucleon-nucleon potential. These calculations indicate a strong influence from the $g_{9/2}$ orbital, beginning at moderate energy and spin in ^{62}Fe and extending to the low-lying states of

^{64}Fe. New levels identified above a 239-ns, $9/2^+$ isomer in ^{61}Fe appear to be consistent within a rotation-aligned coupling scheme, with prolate deformation $\beta \sim 0.24$, a value supported with both the shell model and Particle-triaxial rotor model. The data from this work mark a significant achievement in terms of understanding the evolution of nuclear structure in this region and the possible onset of deformation near $N = 40$. Still, more theoretical work is needed in order to better characterize experimentally observed features of this region. In addition to the Fe experiments described in the body of this thesis, another measurement was carried out in which the structure of ^{128}Cd was investigated. This nucleus, like ^{64}Fe, can be viewed as two proton and two neutron holes in a double-magic system. The identification of isomeric decay, and a confirmation of 2^+ and 4^+ level energies is described.

STRUCTURE OF Fe ISOTOPES AT THE LIMITS OF THE *pf* SHELL

by
Nathan Hoteling

Dissertation submitted to the Faculty of the Graduate School of the
University of Maryland, College Park in partial fulfillment
of the requirements for the degree of
Doctor of Philosophy
2008

Advisory Committee:

Professor William B. Walters, Chair/Advisor
Professor Alice Mignerey
Professor John Ondov
Professor Doug English
Professor Elizabeth Beise, Graduate School Representative

Education, I fear, is learning to see one thing by going blind to another.

Aldo Leopold, **A Sand County Almanac**

ACKNOWLEDGMENTS

First and foremost, let me thank my supervisor, Bill Walters, for giving me an absolutely fantastic experience in graduate school. He gave me freedom and independence and the opportunity to follow my own interests, be it in coursework, conferences, summer schools, experiments, or just about anything else. I attribute a large part of my continued enthusiasm for science to the encouragement and opportunity that he offered during my tenure as a graduate student.

My on-site supervisor at Argonne National Laboratory, Robert Janssens, also had a profound influence on my success as a student. Often busy with administrative responsibilities, Robert would always make time for scientific discussions or to review the latest iteration of whatever paper I was working on at the time. His infamously critical editing was a valuable asset that contributed significantly to my own scientific writing skills.

With my presence at Argonne, I was exposed to an incredible and diverse array of scientists. Of the staff at the lab, I owe the most thanks to Shaofei Zhu, without whom any data sorting and analysis on my part would not have made it past the preliminary stages. I owe a debt of gratitude, as well, to the remainder of the Gammasphere group, who seem to make all Gammasphere experiments run smoothly, which is by no means a small feat.

I would be remiss to neglect the contributions of the group from Krakow,

including Bogdan Fornal and Rafal Broda, who always took a careful look at my analysis, and without whom key features of our data may never have been revealed. Morten Hjorth-Jensen, from the University of Oslo, also deserves recognition, as his patience in teaching me to run the Oslo shell model codes was invaluable to the success of this thesis.

I thank Paul Mantica, from Michigan State University, for the use of his Beta Counting System at the NSCL. His support and patience as I slogged through the data from our Cd experiment was absolutely critical; without his help I would probably still be staring at a computer screen in confusion.

Last, I would like to thank my wife, Crystal, just for being there for me right from the beginning. I often wonder if I could have kept my sanity if weren't for Crystal telling me to *snap out of it!* when I drifted into deep thought at the dinner table, or lending a (usually) patient ear when I went on tangents about science. Thanks!

Table of Contents

List of Tables

List of Figures

Chapter 1

Background and Motivation

1.1 Shell structure in nuclei

One of the most important developments in the history of nuclear structure research was the recognition that nucleons occupy discrete orbitals, which themselves make up shells and are, in turn, distinguishable by many observable properties. Of these properties, one of the most easily recognizable is the energy of the first excited 2^+ state in a nucleus with even neutron and proton numbers, as illustrated in Figure 1.1a. Here, the 2^+ energy, plotted as a function of neutron number, exhibits clear peaks at $N = 2$, 8, 20, 28, 50, and 82 (an additional peak at 126 is not shown in this plot). A similar trend could be demonstrated if the data were plotted as a function of proton number, or if other quantities were plotted such as transition rates, nucleon separation energies, nuclear radii, neutron absorption cross sections or gross number of stable isotopes (or isotones). All of this rings with a tone similar to that of atomic physics, where some elements exhibit increased ionization energies due to the shell

structure which characterizes the filling of electronic orbitals, as depicted in Fig. 1.1b. In spite of the similarity between the two cases, it is clear that the shells differ since the peaks in Fig. 1.1a and b are, for the most part, different. The challenge of reproducing what became known as the "magic numbers" puzzled scientists for years until Maria Goeppert-Mayer [1] and, independently, J. Hans D. Jensen *et al.* [2], proposed a shell model based on strong spin-orbit coupling. Not only was this new model able to reproduce the magic numbers, it provided the foundation necessary for the development of much of what is understood about nuclear physics today.

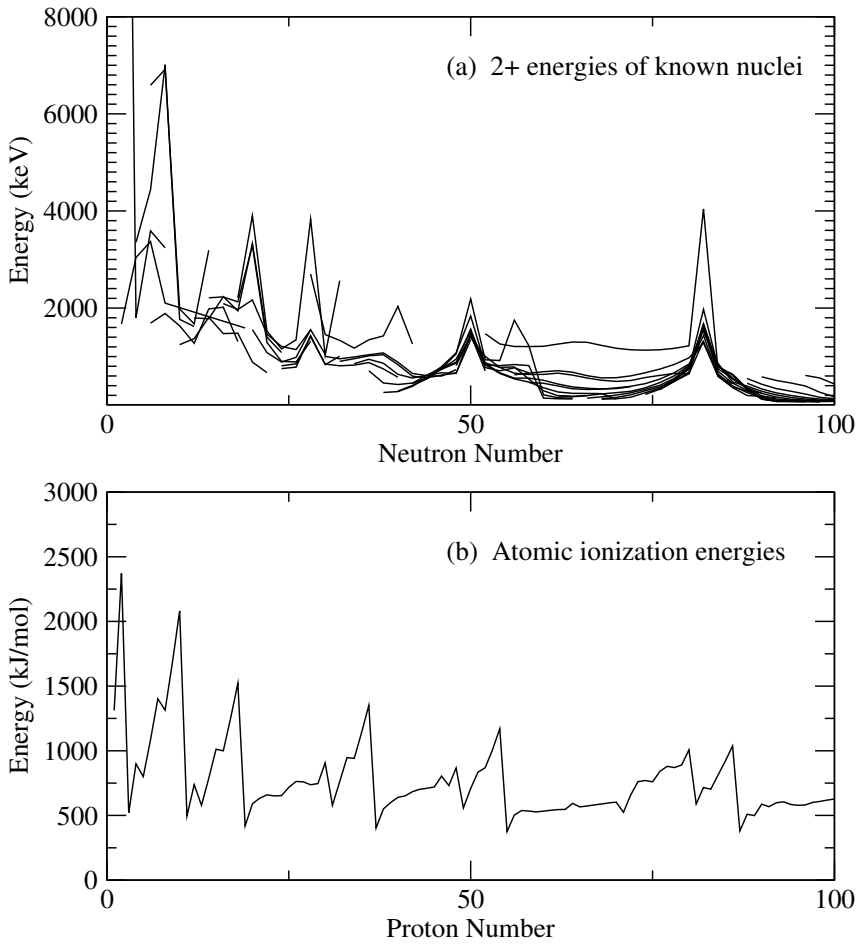

Figure 1.1: (a) Systematics of 2^+ energies in known nuclei, adapted from Ref. [3], and (b) atomic ionization energies, from Ref. [4]. Both give a clear indication of shell structure in the respective systems.

1.1.1 Shell model formalism

Any quantum mechanical problem will generally involve some kind of solution to the Schrödinger equation. As such, one of the most important steps is to determine a proper Hamiltonian. In a many-body problem such as the one faced with in nuclear physics, it is useful to begin with the assumption of independent particle motion, so that the Hamiltonian is written as the sum of individual components from each particle in the nucleus,

$$H^{(0)} = \sum_{i=1}^{A} [T_i + U(r_i)]. \tag{1.1}$$

Since the Pauli Exclusion Principle mandates that the wave functions for identical particles be antisymmetric, the eigenfunctions to the above equation are given by the Slater determinant which, for a two-particle system, is written,

$$\Phi_{\alpha_1,\alpha_2} = \frac{1}{\sqrt{2!}} \begin{vmatrix} \phi_{\alpha_1}(1) & \phi_{\alpha_1}(2) \\ \phi_{\alpha_2}(1) & \phi_{\alpha_2}(2) \end{vmatrix} = \frac{1}{\sqrt{2!}} [\phi_{\alpha_1}(1)\phi_{\alpha_2}(2) - \phi_{\alpha_1}(2)\phi_{\alpha_2}(1)], \tag{1.2}$$

where ϕ_{α_i} are the single-particle wave functions, given by the product of radial and angular components. This leads to a rather complex expression which includes Clebsch-Gordon coefficients, spherical harmonics, and the radial component. However, the only part of this expression that is not explicitly defined is the radial part, $R_{n,\ell}(r)$. The details of this function depend on the form of the potential $U(r)$ of eqn. (1.1). It turns out that the choice of this potential is not straightforward. It must reproduce the known features of the nuclear force, namely short-range, strong, and relatively constant within the bounds of the nuclear radius (*ie:* a flat bottom). The potential used most often in this case is the harmonic oscillator, although it is

neither short-range nor constant within the bounds of the nuclear radius (although one typically uses a modified HO potential, which includes the addition of an ℓ^2 terms which "flattens" the bottom of the potential). Still, the choice of a harmonic oscillator potential is beneficial since the eigenfunctions ϕ_{α_i} are well-known and integrable. On the other hand, a more realistic potential given by Woods-Saxon vanishes at large r, and possesses a flat bottom, but is not integrable.

$$U(r) = \frac{1}{2}m\omega^2 r^2 \qquad \text{harmonic oscillator} \tag{1.3}$$

$$U(r) = \frac{U_0}{1 + exp(\frac{r-R_0}{a})} \qquad \text{Woods-Saxon.} \tag{1.4}$$

Inserting either of these equations into the Schrödinger equation does not reproduce the shell gaps observed from nuclear data. To properly account for these "magic numbers" necessitates the introduction of a strong spin-orbit component.

The concept of spin-orbit coupling is somewhat abstract. It arises from the fact that, from the perspective of a single nucleon moving about the nucleus, the intrinsic nucleon spin causes an apparent motion of the nucleus around the nucleon. This apparent motion produces a magnetic field that interacts with the magnetic moment of the nucleon. The interaction energy of a magnetic moment with a magnetic field is given by the dot product of the two. Since the magnetic moment of the nucleon is proportional its spin, and the magnetic field arising from the apparent motion of the nucleus is proportional to the orbital angular momentum, the spin-orbit interaction energy must be proportional to the dot product $\vec{\ell} \cdot \vec{s}$ [5],

$$U_{SO} = f(r)\vec{\ell} \cdot \vec{s}, \tag{1.5}$$

where the function $f(r)$ contains the dependence on the radial coordinate r and can be related to the central potential.

Based on experimental observations the expectation value $< f(r) >_{n,\ell}$ is estimated to be of the order $-20A^{-2/3}$ MeV [6]. Within the harmonic oscillator picture, the shell gaps are given by the oscillator frequency $\hbar\omega_0 \sim 41A^{-1/3}$ MeV. Hence, from these relations and eqn. (1.5), it is apparent why the spin-orbit force becomes important at higher mass and angular momentum, and in particular why the harmonic oscillator shell gaps persist up to nucleon number 20 but no further. It should be emphasized that a microscopic understanding of the quantitative features of the spin-orbit force are as yet not well understood, although its presence as a strong force is clearly required in order to reproduce the observed magic numbers.

The Slater determinant of eqn. (1.2) gave the normalized, antisymmetrized wave functions of a two-particle system of identical fermions. Since the nucleus contains both protons and neutrons that interact with one another, these wave functions cannot be used in their present form. Instead, it is useful to introduce a new quantum number, the isospin τ (referred to later as T), which facilitates the distinction between protons and neutrons. Note that this formalism can only be introduced here because of the similarity between protons and neutrons, namely that pp, nn, and pn interactions are identical except for the Coulomb interaction between protons. This is an experimental observation, most evident in the nearly identical level structures observed in mirror nuclei (*ie:* nuclei for which proton and neutron numbers are exchanged). In the isospin formalism, protons and neutrons are viewed as different manifestations of the same particle, protons having $m_\tau = -\frac{1}{2}$

and neutrons $m_\tau = +\frac{1}{2}$. The choice of $\pm\frac{1}{2}$ is arbitrary but the adopted values were chosen so that most nuclei would have positive isospin, since most nuclei have more neutrons than protons.

Up to this point, the focus of this discussion has been exclusively on the two-particle system. It is easy to see that the complexity of the wave function increases dramatically with the number of particles in a system. As noted above, this can be illustrated by calculating the Slater determinant of eqn. (1.2) for 3-particle, 4-particle, *etc.* systems. This growing complexity quickly challenges the practicality of carrying out shell model calculations for anything but the lightest nuclei. To address this problem, any medium or heavy nucleus is typically viewed with respect to the nearest double-closed shell. The aptly termed *core* is then taken to be an inert system and the valence nucleons are treated independently,

$$\Phi_{J,\tau} \sim \Phi_{0,\tau}^{core} \times \Phi_{J,\tau}(\alpha_1, \alpha_2, ...)]. \tag{1.6}$$

Returning to the independent-particle Hamiltonian given by eqn. (1.1), it is now possible to choose a potential $U(r)$ so that the problem can be solved. A caveat here is that the assumption of independent-particle motion is unrealistic, since the orbiting particles must surely interact with one another. Hence, the independent-particle Hamiltonian of an A-particle system can be written in terms two-particle interactions as,

$$H = \sum_{k=1}^{A} T_k + \sum_{k=1}^{A} \sum_{\ell=k+1}^{A} W(\vec{r_k}, \vec{r_\ell}), \tag{1.7}$$

where $W(\vec{r_k}, \vec{r_\ell})$ is the two-body interaction between the k^{th} and ℓ^{th} nucleons. Choos-

ing an average potential $U(r_k)$, the Hamiltonian becomes,

$$H = \sum_{k=1}^{A}[T_k + U(r_k)] + \sum_{k=1}^{A}\sum_{\ell=k+1}^{A} W(\vec{r_k}, \vec{r_\ell}) - \sum_{k=1}^{A} U(r_k), \tag{1.8}$$

where the first term is identical to the independent-particle Hamiltonian given by eqn. (1.1), and the second and third account for the deviation from independent particle motion, known as the residual interaction. Separating the summations into core and valence contributions, eqn. (1.8) can be re-written,

$$H = H_{core} + H_1 + H_2 + V(\vec{r_1}, \vec{r_2}). \tag{1.9}$$

In the above equation, H_{core} contains all of the interactions of nucleons making up the core, H_1 and H_2 are the single-particle contributions from particles 1 and 2, and $V(\vec{r_1}, \vec{r_2})$ is the residual interaction describing all interactions between particles 1 and 2, as well as any interaction with core nucleons. Inserting this form of the Hamiltonian into the Schródinger equation yields an analogous expression for the energy,

$$E = E_{core} + E_1 + E_2 + \langle \Phi_{J,\tau} | V(r_1, \vec{r}_2) | \Phi_{J,\tau} \rangle . \tag{1.10}$$

Here, E_{core} is the binding energy of the core nucleus, E_1 and E_2 are defined as the single-particle energies of orbitals outside the core, and $\langle \Phi_{J,\tau} | V(r_1, \vec{r}_2) | \Phi_{J,\tau} \rangle$ is the residual interaction which needs to be defined by theory.

It is important to note that the energy given by eqn. (1.10) is for pure configurations only. In principle, any close-lying state with the same total angular momentum J and total isospin τ will mix. The mixed eigenstates are given by

linear combinations of the unperturbed wave functions,

$$(\Psi_{J,\tau})_p = \sum_{k=1}^{g} a_{kp} (\Phi_{J,\tau})_k, \tag{1.11}$$

where g is the number of configurations that mix and the label $p = 1, 2, \cdots, g$. The coefficients a_{kp} fulfill the condition,

$$\sum_{k=1}^{g} |a_{kp}|^2 = 1. \tag{1.12}$$

Inserting eqn. (1.11) into the Schrödinger equation gives,

$$H(\Psi_{J,\tau})_p = E_p (\Psi_{J,\tau})_p, \tag{1.13}$$

which leads to a system of linear equations,

$$\begin{pmatrix} H_{11} & H_{12} & \cdots & H_{1g} \\ H_{21} & H_{22} & \cdots & H_{2g} \\ \vdots & \vdots & \ddots & \vdots \\ H_{g1} & H_{g2} & \cdots & H_{gg} \end{pmatrix} \begin{pmatrix} a_{1p} \\ a_{2p} \\ \vdots \\ a_{gp} \end{pmatrix} = E_p \begin{pmatrix} a_{1p} \\ a_{2p} \\ \vdots \\ a_{gp} \end{pmatrix}, \tag{1.14}$$

where $H_{\ell,k}$ are given by the summations of all single-particle and residual interaction terms for particles ℓ and k. Equation (1.14) represents a classic eigenvalue problem, which is solved by setting the determinant equal to zero,

$$\begin{vmatrix} H_{11} - E_p & H_{12} & \cdots & H_{1g} \\ H_{21} & H_{22} - E_p & \cdots & H_{2g} \\ \vdots & \vdots & \ddots & \vdots \\ H_{g1} & H_{g2} & \cdots & H_{gg} - E_p \end{vmatrix} = 0. \tag{1.15}$$

The result is a polynomial of order g in E_p, which has g solutions corresponding to the perturbed energies of each state involved in the mixing. Each state possesses a

unique set of coefficients a_{kp} which must be determined to obtain the wave functions $\Psi_{J,\tau}$. Thus, for each of the g solutions to E_p, eqn. (1.14) must be solved to obtain the coefficients a_{kp} and therefore the perturbed wave functions $\Psi_{J,\tau}$.

1.1.2 Model space

The complexity of the problem outlined by eqns. (1.14) and (1.15) above clearly scales with the number of states that mix. The number of states of a given J and τ that can mix largely depends on the model space used for the calculation, and for realistic calculations this can be quite large, even with the assumption of an inert core. For example, in the relatively small pf model space built upon a ^{48}Ca core and consisting of $f_{7/2}$, $p_{3/2}$, $p_{1/2}$, and $f_{5/2}$ proton orbitals and $p_{3/2}$, $p_{1/2}$, $f_{5/2}$ neutron orbitals, there are nearly 3×10^5 2^+ states that can be formed. The *total m-scheme dimension* refers to the total number of states of all J that can be formed in a given nucleus within a particular model space. This is illustrated in the upper panel of Figure 1.2 for Ca, Ti, Cr, and Fe isotopes within the pf model space. What is immediately clear from this picture is the parabolic shape of the dimension curve, indicating that the most complex calculations will occur at mid-shell. Displayed in the lower panel of Fig. 1.2 are the exact dimension as a function of J for different isotopes of Fe. This gives a more realistic depiction of the the matrices that need to be diagonalized, as each value of J must be solved according to eqn. (1.15).

As disconcerting as the data in Figure 1.2 are, they are somewhat misleading since most shell model codes do not require full diagonalization to obtain reasonable

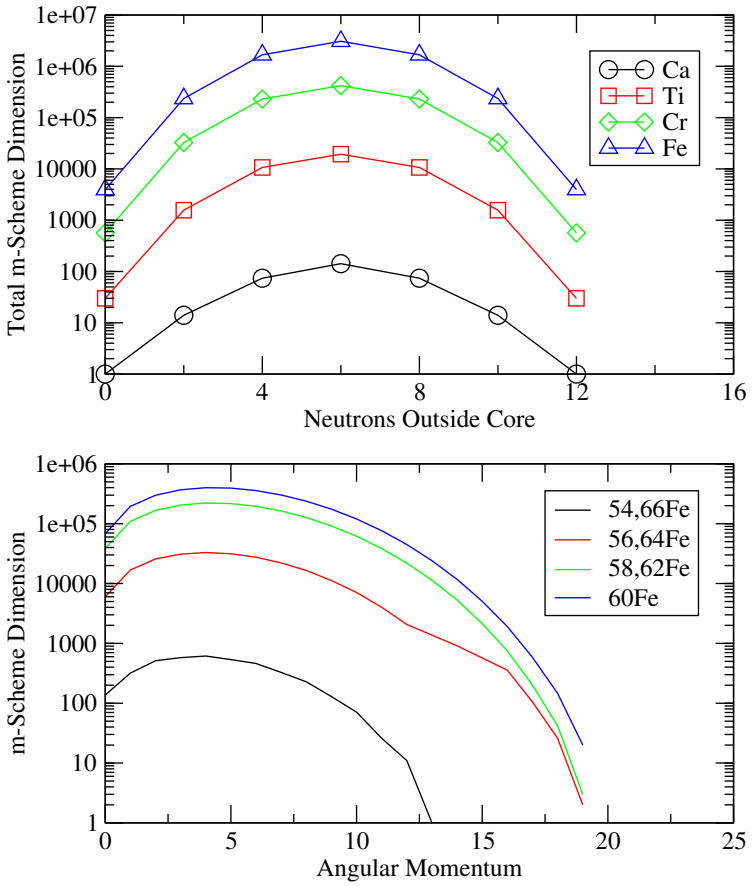

Figure 1.2: (Upper panel) The total m-scheme dimension of different nuclei assuming a ^{48}Ca core and pf model space (see text), and (lower panel) a breakdown of dimensionality as a function of J for the Fe isotopes.

results. Instead, the standard procedure, known as the Lanczos method, uses an iterative tri-diagonalization procedure to numerically obtain approximate values for a given set of eigenvalues [7]. A detailed discussion of this method is beyond the scope of this thesis, but it is worthwhile to note that some practical limitation nevertheless exists, which will be encountered later in the discussions of shell model calculations, that relates to the storage of temporary files during the calculation. For the calculations reported in this work, the limitation is manifested in the 2-Gigabyte file size limitation in the Linux operating system. This can, of course, be

surmounted but work in that direction was not undertaken here.

To facilitate more efficient and practicable calculations in large configuration spaces, it is necessary to apply truncations beyond the assumption of an inert core. There are a number of different strategies that one can adopt here, and when properly applied they can vastly simplify the calculation and still produce excellent results. One strategy is similar to the idea of treating the core as inert: by disallowing excitations from a particular orbital (*ie:* "freezing" the orbital), the size of the core can be effectively enlarged and the configuration space thus reduced. This procedure is useful if the model space covers more than one major shell gap, or if the existence of a subshell gap lends credence to this assumption. A second possibility is to restrict the total number of particles allowed in a particular orbital. For instance, if an orbital has a large single-particle energy then it could be reasonable to expect multi-particle excitations beyond a certain level to exist at very high energy only, so these states would have negligible admixtures in the low-lying states sought in a particular calculation. In a similar vein, one can restrict multi-particle excitations from and into all orbitals, assuming that anything beyond, say, 3-particle excitations can be neglected. Each of the truncation methods described here has its merits, but a note of caution should be expressed for their unmitigated use, as the temptation to use such methods as a free parameter to fit to data can be high; such a procedure would seem to, in some way, undermine the role of the two-body matrix elements to be described in the next section.

1.1.3 Effective interactions

Recall from eqn. (1.10) that the energy of a particular state is given by the sum of core, single-particle, and two-body interaction energies. Of these terms, only the last cannot be trivially determined. In fact, the problem of obtaining realistic values for this term is one of the fundamental goals of nuclear structure research. Since the microscopic properties of this interaction can only be established with consideration of the quark structure of the nucleon and the application of QCD, a successful quantitative approach has not yet been attained. However, the microscopic nature of this force is not necessarily needed since semi-empirical approaches have seen much success in this arena. The three main categories of the semi-empirical approach, as defined by Brown [8], are: 1) the *potential model fit*, in which data are fit to some pre-defined model that is then used to compute two-body matrix elements; 2) the *model-independent fit*, whereby a selected group of linear combinations of well-determined two-body matrix elements are fit to data, and for the remaining matrix elements the results from some bare nucleon-nucleon interaction are used; and 3) the *G plus monopole method*, in which the matrix elements are computed from some bare nucleon-nucleon force and then adjusted to fit observed monopole behavior (the monopole interaction will be described in section 1.2.1). In the latter two, the bare nucleon-nucleon interaction is generally adopted from a fit to the phase-shift analyses of nucleon scattering experiments, assuming some meson exchange potential. Since these methods are becoming increasingly sophisticated, there is a fourth category that can be added to the list above, in which the effective interaction is derived from

some bare nucleon-nucleon force without further empirical modification. This will be termed the *G-matrix method*, although other techniques do exist.

The phase shift analyses alluded to above show a strong repulsion at higher energy which is interpreted as the effect of a hard core, on the order of 0.5 fm. This means that the residual interaction $V(1,2)$ cannot be treated in terms of perturbation theory; instead, the bare interaction must be renormalized before it can be used in a straightforward manner in shell model calculations. The resulting effective interaction, then, comes from the accumulation of these short-range correlations and, as such, will be very dependent on the model space used for the renormalization procedure. The most commonly used procedure for this is currently the G-matrix method, which is mathematically quite cumbersome and will not be discussed in any detail here. Further information can be found in Refs. [9–11]. Described below are some examples of pf-shell effective interactions from each of the three empirical approaches denoted above plus the fourth category of pure G-matrix interactions.

Potential model fit: *FPD6* interaction

The principle behind the potential model fit is that the effective interaction can be derived from some empirical potential consisting of parameters determined from experimental data. The main idea is to obtain an empirical interaction with a minimal number of parameters which can be applied to different mass regions. Most of this type of interaction currently in use assumes central, spin-orbit, and tensor components, each of which is expressed in terms of one-boson-exchange potentials.

For example, the *FPD6* effective interaction was derived in this manner by fitting to 61 experimental levels, binding energies, and single-particle energies [12]. The fitting procedure included 22 parameters, 10 of which were fixed to values determined from a similar fit to levels in the *sd* shell [13]. The empirical data used in the fitting procedure came from Ca, Sc, and Ti isotopes with $A = 41 - 49$. A mass dependence $TBME(A) = TBME(A = 42) \times \left(\frac{42}{A}\right)^{-0.35}$ was introduced so that the resulting matrix elements could be applied to a broader mass range, and a modified version of the Kuo-Brown matrix elements (discussed below) was used as a starting point in the fitting procedure [14].

Model-independent fit: *GXPF1* and *GXPF1A* interactions

In the model-independent fit, matrix elements are calculated directly during the fitting procedure; that is, each matrix element is treated as a free parameter. To cope with troublesome parameter-to-data ratios, then, the fit is made to linear combinations of matrix elements. For example, in the *GXPF1* effective interaction, 70 well-determined linear combinations of matrix elements were fit to 699 empirical levels and binding energies from 87 nuclei from $_{20}$Ca to $_{32}$Ge [15]. The starting values for the matrix elements were adopted from a G-matrix calculation and the Bonn-C bare nucleon-nucleon interaction potential. A mass dependence $A^{-0.3}$ is assumed for the matrix elements.

The *GXPF1* interaction was later adjusted to form the *GXPF1A* interaction [16]. Specifically, five individual matrix elements were adjusted, a move spawned

by a lack of data for $N \geq 32$ nuclides in the original fit and hence, the resulting uncertainty associated with $p_{1/2}$ and $f_{5/2}$ matrix elements. Additionally, a general feature of the *GXPF1* interaction was that it tended to over-predict 2^+ energies, which was apparently an artifact of the Finite Dimension Basis Approximation used to diagonalize matrices during the fitting procedure. It was contested that this procedure does not properly treat pairing correlations, thus over-compensating the pairing strength which results in higher 2^+ energies (or, rather lower 0^+ energies). To address this latter issue, three $J = 0$, $T = 1$ matrix elements were weakened by 200 keV. For the former, two of the three matrix elements just addressed were weakened by an additional 300 keV, and the $(\mathrm{f_{5/2}p_{1/2}})^{J=2,3}_{T=1}$ matrix elements were adjusted by -350 and +250 keV, respectively. These particular values were chosen so as to maintain a constant monopole centroid (see section 1.2.1 for further discussion of this).

G plus monopole: *KB3* and *KB3G* interactions

The last example of an empirical interaction listed above was, compared with the examples given in the two previous sections, actually initiated much earlier. It is also historically quite interesting since it uses as its basis the results of a G-matrix calculation by Kuo and Brown (*KB*) [17–20], which itself is based on the bare nucleon-nucleon potential of Hamada and Johnston [21]. Thus, the *KB* effective interaction was the first large-scale attempt to adapt a general nucleon-nucleon interaction to calculations in nuclear matter. Of course, there were sharp deficien-

cies in the results of this interaction, which were especially evident as experimental studies extended further beyond the closed-shell systems. Because of these deficiencies, a series of modifications to the original KB matrix elements was undertaken, resulting in the *KB3* [22–24] and *KB3G* [25] effective interactions.

In arriving at the *monopole-adjusted* interaction *KB3*, the authors argued that an inherent limitation in every G-matrix effective interaction is a failure to reproduce saturation properties in nuclear matter, *ie:* binding energy $\approx$ -16 MeV/A and $\rho \approx$ 0.17 fm^{-3} . It was further proposed that the source of these problems lies in the monopole part of the nuclear Hamiltonian, and that specific adjustments to matrix elements important to this term would absolve a large part of the discrepancies seen in G-matrix-derived effective interactions [23, 26] (Note that the issue here is not with the G-matrix methodology but rather with the nucleon potentials; see below). Later, after some specific deficiencies were identified in the *KB3* interaction, further adjustments were made to the matrix elements which gave rise to the *KB3G* effective interaction.

Whereas the arguments in support of these adjustments are based on well-founded theoretical concepts, it appears that the actual changes to the matrix elements were guided by agreement to empirical data and not calculated from theory. For instance, the primary modification defining the *KB3* interaction was a gross shift in the $T = 1$, ($f_{7/2}r$) (where r$\equiv p_{1/2}p_{3/2}$,$f_{5/2}$ orbitals) matrix elements by +300 keV, adopted because of a desired shift in several experimental levels [22]. Similar arguments are conveyed for most of the other changes, although no specific reasons are given for the changes adopted in *KB3G*. This distinction is made not to take

away from any validity that the results might hold, but to emphasize the empirical nature of the resulting interactions.

Modern G-matrix interactions

The inherent flaw in the monopole component of Hamiltonians derived from bare nucleon-nucleon interactions is a serious one, but modern approaches have sought to improve on this. Machleidt, Sammarruca, and Song [27] describe a similar phenomenon in terms of so-called "off the energy shell" effects that arise from the fact that energy is conserved within the multi-nucleon system but not necessarily within the two nucleons that interact. This effect understandably does not manifest itself in two-nucleon scattering experiments and, therefore, an important component of nuclear matter calculations is missing in the scattering data. To address this problem, those authors introduced a more rigorous meson exchange term to the usual high-precision fit (to 4301 scattering data; $\chi^2 = 1.02$), so that these off-shell components would be accounted for. The result gave rise to a 44% improvement in the binding energy of the triton compared to purely "on the energy shell" potentials and, ultimately, the CD-Bonn nucleon-nucleon potential [28].

More recently, the attention of the theoretical community has focused on a chiral perturbation theory-based derivation of the nuclear force, which is favored to the above approach because it is rooted more deeply in fundamental theory [29]. The *next-to next-to next-to leading order* (N3LO) solution has attained nearly as much success as high-precision fits like CD-Bonn but with fewer parameters (*ie:*

24 parameters compared to 38 in CD-Bonn, and $\chi^2 = 1.1$ and 1.5 for np and pp potentials, respectively) [30]. However, this potential has not yet seen broad use in nuclear structure applications.

1.1.4 Deformed shell model

Up to this point, all of the formalism has operated under the assumption of a spherical potential. If, instead, the potential is assumed to be deformed but axially symmetric, eqn. (1.3) can be rewritten,

$$V = \frac{1}{2}m(\omega_x^2(x^2 + y^2) + \omega_z^2 z^2), \tag{1.16}$$

where the angular frequencies ω are defined in terms of deformation parameter δ,

$$\begin{aligned} \omega_x^2 &= \omega_0^2(1 + \frac{2}{3}\delta) \\ \omega_z^2 &= \omega_0^2(1 - \frac{4}{3}\delta). \end{aligned} \tag{1.17}$$

Substitution of eqns. (1.17) into eqn. (1.16) yields (after some work) the expression,

$$\begin{aligned} V &= \frac{1}{2}m\omega_0^2 r^2 - \frac{4}{3}m\omega_0^2 r^2 \delta\sqrt{\frac{\pi}{5}}Y_{20}(\theta,\phi), \\ \text{where } \; Y_{20}(\theta,\phi) &= \sqrt{\frac{5}{16\pi}}\frac{3z^2 - r^2}{r^2}. \end{aligned} \tag{1.18}$$

Equation (1.18) is just the spherical harmonic oscillator potential plus a term proportional to deformation δ. So, at the limit $\delta \to 0$, this expression becomes the familiar harmonic oscillator potential of eqn. (1.3). Furthermore, the deviation from spherical behavior is determined almost entirely from the second term of this equation, assuming that the effects of deformation on spin-orbit and ℓ^2 terms of the nuclear Hamiltonian can be neglected [6]. The consequence of this expression,

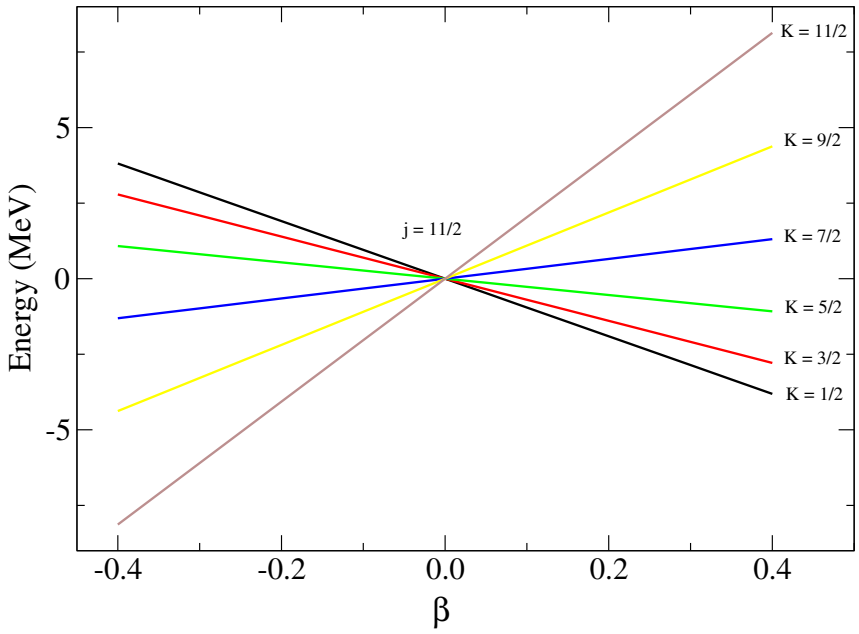

Figure 1.3: The substates of orbital j split up as a function of projection quantum number K for an axially deformed nucleus.

illustrated in Figure 1.3, is that the different substates (*ie:* states with the same j but different projection, m_j, onto the z-axis), diverge as a function of deformation. Specifically, the low-m substates are lowered in energy under prolate (*ie:* football-shaped, positive β) deformation, and the high-m substates are raised. The opposite occurs under oblate (*ie:* doorknob-shaped, negative β) deformation.

Note that the deformation here is given in terms of β, instead of δ which was defined above. This convention was adopted because most nuclear structure applications tend to use this parameter, which will be defined later. For the purposes of this discussion, one need only consider the relation between β and δ [31],

$$\beta \approx \sqrt{\frac{\pi}{5}}\frac{4}{3}\delta. \tag{1.19}$$

Now that the shape assumed for the nucleus is nonspherical, a new degree of freedom must be considered that previously could be neglected: collective rotation.

Since rotation is indistinguishable in a spherical quantum system, this degree of freedom could be neglected in the spherical shell model formalism. However, in the deformed shell model, the Hamiltonian must be written,

$$H = H_p + H_{rot}. \tag{1.20}$$

The rotational kinetic energy is given by,

$$\frac{\hbar^2}{2\Im} R^2, \tag{1.21}$$

where $\Im$ is the moment of inertia of the rotating system and R is the rotation quantum number. One of the important consequences of this equation is that, for a rigid-rotational system (*ie:* constant $\Im$), the ratio of level sequences gives a telltale signature. For example, the ratio,

$$E_{4^+/2^+} = \frac{R^2_{4^+}}{R^2_{2^+}} = \frac{4(4+1)}{2(2+1)} = 3.33. \tag{1.22}$$

The rotation quantum number, R, is the difference between total angular momentum, I, of the rotating nucleus, and total angular momentum, j, of the non-rotating nucleus,

$$R = I - j. \tag{1.23}$$

Thus, the rotational Hamiltonian can be represented by,

$$\begin{aligned} H_{rot} &= \frac{\hbar^2}{2\Im} \left[(I_x - j_x)^2 + (I_y - j_y)^2 \right] \\ &= A \left[(I^2 - K^2) + (j^2 - \Omega^2) - 2(I_x j_x + I_y j_y) \right], \end{aligned} \tag{1.24}$$

where $K = I_z$, $\Omega = j_z$, and the rotational constant $A = \frac{\hbar^2}{2\Im}$. Note that, for axially deformed systems, $K = \Omega$. The last term in brackets in eqn. (1.24) is the Coriolis

term. Substitution of eqns. (1.18) and (1.24) into eqn. (1.20) leads to,

$$H = e_j + A\left[I(I+1) + j(j+1)\right] + (C - 2A)\Omega^2 + H_c. \tag{1.25}$$

The diagonal energies of eqn. (1.25) are given by [32],

$$E(Ij\Omega) = e_j + A\left[I(I+1) + j(j+1) + \delta_{\Omega,1/2}(-1)^{I+j}(I+\frac{1}{2})(j+\frac{1}{2})\right] + (C-2A)\Omega^2, \tag{1.26}$$

where the term absent in the previous equation comes from symmetrization of the wave function [33]. Stephens showed that the diagonal energies of eqn. (1.25) can be alternatively written as a function of the projection, α, of j along the rotation axis [32],

$$E(Ij\alpha) = e_j + A\left[(I-\alpha)(I-\alpha+1) + \left(\frac{C}{2A} + \frac{\alpha}{(2I+1)}\right)\left(j(j+1) - \alpha^2\right)\right]. \tag{1.27}$$

This gives the energies in the so-called rotation-aligned coupling picture. Simple numerical solutions to Eqns. (1.26) and (1.27) can be obtained with the use of empirical relations derived from Grodzin's Rule [32],

$$\begin{aligned} E_{2+} &= 6A = \frac{1225}{a^{7/3}\beta^2} MeV \\ C/2A &= 0.379\frac{a^2\beta^3}{j(j+1)} \\ e_j &= e'_j - 51.5\frac{\beta}{a^{1/3}}. \end{aligned} \tag{1.28}$$

The numerical solutions are illustrated in Figure 1.4 for $\Omega = \frac{1}{2}$ and $\alpha = \frac{11}{2}$. Here the mass, a, is taken to be 130 and $j = 11/2$ has been used, in accordance with similar calculations presented in Ref. [32]. The important consequence depicted here is that, up to moderate deformation, the state with $\alpha = \frac{11}{2}$ is lower in energy

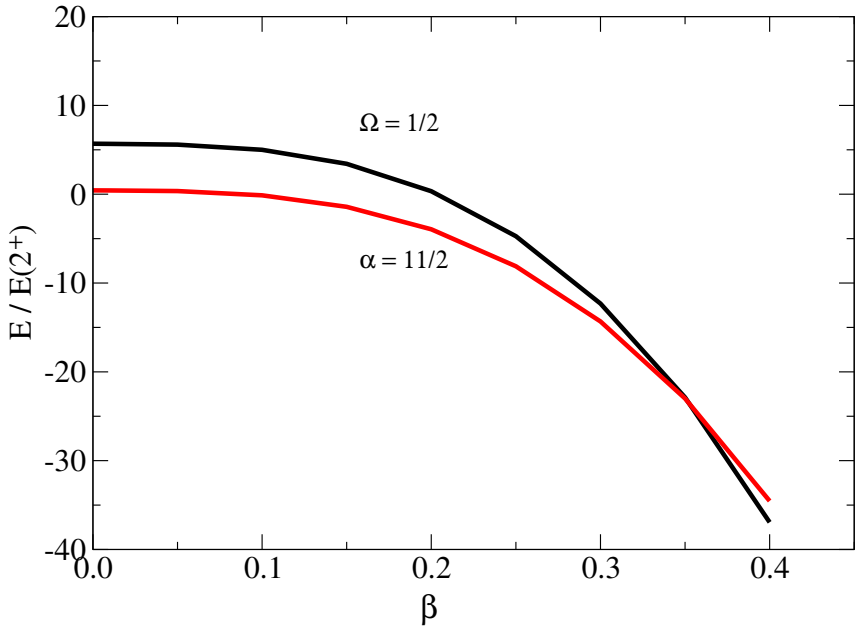

Figure 1.4: Comparison of level energies calculated with Ω or α assumed to be a good quantum number. The former is computed from eqn. (1.26), and the latter from eqn. (1.27). This shows that, for a nucleus characterized by rotation-aligned coupling, the $\alpha = j_{max}$ state can occur below the $\Omega = \frac{1}{2}$ state.

than the state with $\Omega = \frac{1}{2}$. Hence, whereas Fig. 1.3 seemed to indicate that prolate deformation always produces the lowest possible Ω-value at the lowest energy, Fig. 1.4 shows that this contention is not always true.

A conceptual picture of the rotation-aligned coupling scheme described above is of a cross-shell excitation of a single nucleon coupling weakly to the rotation of a deformed system. Thus, one would expect on top of the state with $j = \alpha$, a band consisting of states whose energies closely match those of the $A - 1$ core. For a rigid rotor, this would likely resemble the trends described in eqn. (1.22). However, Stephens [32] points out that, since the phenomenon is exhibited at small deformation, rotational energy spacings are not necessarily prerequisite to the manifestation of this phenomenon. In that work, it is also noted that the so-called "favored" states

which form the excitation band on top of the rotation-aligned state follow a pattern of *E2* multipoles. The converse phenomenon, which occurs for oblate deformation, is known as strong coupling. The distinguishing feature of this is a sequence of *M1* multipole transitions, forming a pattern that does not resemble that of the $A-1$ core nucleus. Further details of the strong coupling picture will not be discussed here but can be found in Ref. [32].

1.2 Motivation

1.2.1 Evolution of Shell Structure

One of the most intriguing aspects of nuclear structure research has been the recognition that shell structure is not absolute. Rather, the magic numbers predicted by the conventional spin-orbit shell model will tend to evolve as a function of neutron-to-proton ratio. One particularly elegant depiction of the gradual changes in structure predicted to exist in the hitherto unknown regions of the nuclear chart comes from the monopole Hamiltonian,

$$H_{ij}^{m\tau} = \sum_{i,j}\left[\frac{a_{kk}}{2}\hat{n}_k(\hat{n}_k+1) + \frac{b_{kk}}{2}\left(\hat{T}_k^2 - \frac{3}{4}\hat{n}k\right)\right] + a_{ij}\hat{n}_i\hat{n}_j + \frac{b_{ij}}{2}\left[(\hat{T}_i+\hat{T}_j)^2 - \hat{T}_i^2 - \hat{T}_j^2\right],$$
$$a_{ij} = \frac{1}{4}(3V_{ij}^{(1)} + V_{ij}^{(0)}), \qquad b_{ij} = V_{ij}^{(1)} - V_{ij}^{(0)}, \qquad V_{ij}^{\tau} = \frac{\sum_J (2J+1)\left\langle ij|V|ij\right\rangle_{J\tau}}{\sum_J(2J+1)}. \tag{1.29}$$

This equation is a generalization of the work of Bansal and French [34], which was used as the basis for the monopole-adjusted interactions *KB3* and *KB3G*, as mentioned in section 1.1.3. The principle behind this formulation is that the angular

components of the interaction are averaged out in the monopole matrix element, V_{ij}^{τ}, and the interaction therefore depends on occupation and isospin only [35]. Of course, this formulation is entirely model-dependent since its success relies ultimately on an effective interaction that is valid over a range of nuclear data. On the other hand, it is also useful for testing new effective interactions. But, the main utility of the monopole Hamiltonian is that it allows one to paint a simple picture of the migration of single-particle levels over the span of a nuclear shell. The monopole matrix elements act on the single-particle energies as they appear outside a magic core, and cause them to shift as a function of the occupation of various orbitals within the model space. The result is a property analogous to the average energy of all states of a given J weighted by their respective spectroscopic factors, known as the effective single-particle energy (ESPE).

Poves and Zuker have argued that the gross features of nuclei across regions of the nuclear chart are delegated by the monopole part of the nuclear interaction, and they have demonstrated a rigorous separation of monopole and multipole components [26, 36]. More recently, Otsuka *et al.* showed that the tensor component of the nuclear force is most influential on the properties of the monopole interaction [37].

The term "tensor force" is used to describe any interaction that is non-central in character. So, whereas a central force depends only on the distance between particles, a tensor force is dependent on the angle which the spins of particles make relative to inter-particle separation [38]. The presence of a tensor component to the nuclear force was proposed as a result of the non-zero quadrupole moment measured

for the deuteron. Since the deuteron is composed of two non-identical particles, a pure central force would result in both particles occupying a spherical s state, and therefore zero quadrupole moment. For the tensor operator, S_{12}, the following semi-quantitative relation is used [39],

$$S_{12} \equiv 3(\vec{\sigma_1} \cdot \vec{e})(\vec{\sigma_2} \cdot \vec{e}) - (\vec{\sigma_1} \cdot \vec{\sigma_2}), \tag{1.30}$$

where $\vec{e}$ is a unit vector in the direction of inter-particle separation and $\vec{\sigma}$ are the unit spin vectors for each particle. Assuming two particles of spin $\vec{\sigma_1}$ and $\vec{\sigma_2}$, separated in the direction $\vec{e}$, four scenarios can be surmised, as depicted in Figure 1.5a. Using the law of cosines, where the dot product is proportional to the cosine of the angle between vectors, it can be shown that the tensor force is most attractive for two particles of anti-parallel spin whose separation is parallel to the spin axis (upper left panel of Fig. 1.5a). In the realistic picture, the former would correspond to two particles of opposite intrinsic spin, *ie:* $s_1 = +\frac{1}{2}$ and $s_2 = -\frac{1}{2}$ or, stated another way, $j_> = \ell + \frac{1}{2}$ and $j_< = \ell - \frac{1}{2}$. A similar argument can be made for the isospin quantum number, so that $\tau = 0$ interactions are stronger than $\tau = 1$. The strongest repulsion is attained for two particles with parallel spin whose separation is parallel to the spin axis (lower left panel of Fig. 1.5a). The inter-particle separation is less intuitive, but one could argue that the separation would be most parallel to the spin axis for two particles of the same orbital angular momentum, ℓ, and oscillator number, N [37]. Thus, the radial distribution of the particles is narrower, and the wave functions overlap more in the direction parallel to the spin axis. In contrast, two particles with vastly different orbital angular momentum will exhibit a wave function stretched in the radial direction.

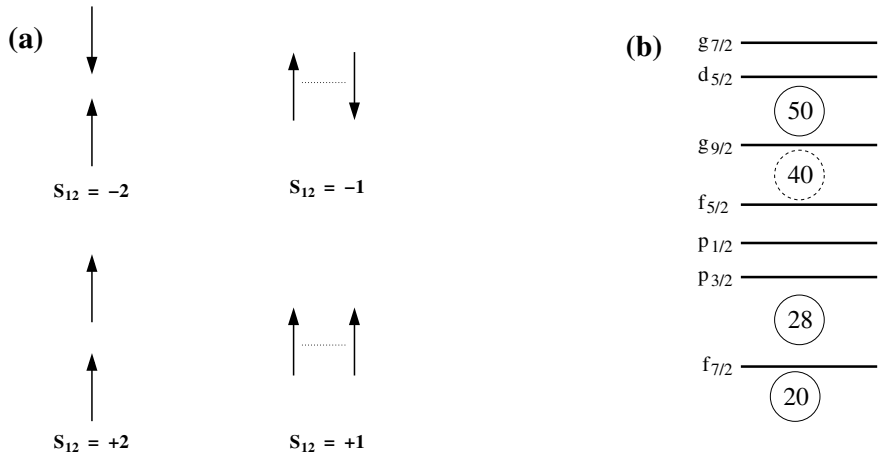

Figure 1.5: (a) Schematic depiction of the tensor force, with the relative interaction strength calculated according to eqn. (1.30), and (b) shell model diagram containing orbitals of interest to this work.

In practice, these basic principles can be applied to a number of regions of the nuclear chart. For instance, Otsuka *et al.* [37] describe a new magic number at $N = 16$, owing to the removal of protons from the $d_{5/2}$ orbital from $^{30}_{14}\mathrm{Si}_{16}$ to $^{24}_{8}\mathrm{O}_{16}$ and the consequent loss of interaction energy between $\pi d_{5/2}$ and $\nu d_{3/2}$ orbitals. Indeed, recent empirical data on binding energy systematics seems to corroborate this [40]. Second, a new magic number was predicted to exist at $N = 34$ in Ca, Ti and Cr, owing to a loss in interaction energy between $\pi f_{7/2}$ and $\nu f_{5/2}$ orbitals caused by the lowered occupation of the $\pi f_{7/2}$ in these lower-pf shell nuclei. In fact, reduced 2^+ energies [41, 42] and higher *B(E2)* [43] values with respect to neighbors tend *not* to support this contention for $^{56}_{22}\mathrm{Ti}_{34}$ and $^{58}_{24}\mathrm{Cr}_{34}$, and efforts are still underway to identify the 2^+ energy of $^{54}_{20}\mathrm{Ca}_{34}$. Instead, a new subshell closure has been discovered at $N = 32$ in this region.

The argument for the existence of a semi-magic number at $N = 34$ focused on a significant energy gap between the filled $\nu(f_{7/2}, p_{3/2}, p_{1/2})$ subshell and the empty

$f_{5/2}$ orbital, induced by the loss of $\tau = 0$ interaction energy once the $\pi f_{7/2}$ orbital was no longer filled (see Fig. 1.5b for a schematic of these orbitals). The argument for a semi-magic number instead at $N = 32$ would consist of an analogous contention, fueled by a large separation between $p_{3/2}$ and $p_{1/2}$ spin-orbit partners. Although the former contention was supported quantitatively by the *GXPF1* effective interaction, the data for neutron-rich Ti and Cr isotopes partly stimulated the modification of *GXPF1* to *GXPF1A*. The *ad hoc* maneuver to solve the problem faced here was to weaken the attraction of the $\left\langle p_{1/2}p_{1/2}\left|V\right|p_{1/2}p_{1/2}\right\rangle_{\tau=1}^{J=0}$ matrix element, which has the consequence of increasing the separation of ESPE between $p_{3/2}$ and $p_{1/2}$ orbitals at $N > 32$ once the $p_{1/2}$ orbit begins to fill. The resulting calculations compare well with experiment to the effect that an $N = 32$ subshell is described and an $N = 34$ is not, at least for Ti and Cr. The *GXPF1A* interaction still predicts a high 2^+ energy for ^{54}Ca [16].

With the above arguments for a subshell closure at $N = 32$ now established, it is interesting to study the evolution of this gap as the $f_{7/2}$ orbit is filled. For instance, Figure 1.6 illustrates the 2^+ energy trends in Ca, Ti, Cr, and Fe, so that the gradual disappearance of the $N = 32$ subshell gap is readily observed. Also depicted in this figure is the shell gap at $N = 28$, which remains robust for all of these nuclei.

Another interesting facet of the structure in this region is manifested in the levels up to moderate spin in ^{50,52,54}Ti [44]. In these isotopes, a large energy gap beginning at 3-4 MeV represents a unique signature of the subshell, spanning $N = 28-32$. The states below this energy gap are dominated by $p_{3/2}$ neutron configurations,

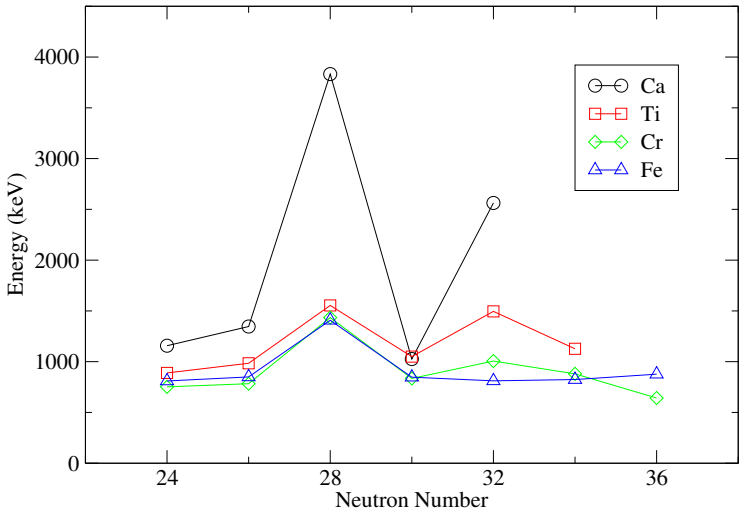

Figure 1.6: The $N = 32$ subshell gap becomes less pronounced as the $f_{7/2}$ orbital is filled until it is completely absent in ^{58}Fe. In contrast, the $N = 28$ shell gap remains robust in all cases.

whereas the states above this gap require excitations beyond the $N = 32$ subshell. This case is a classic example of why it is important to study the structure of even-even nuclei beyond the first excited 2^+ states.

The so-called "island of inversion" cannot be explained in such simple terms. Here, the magic number $N = 20$ disappears for Ne, Na, and Mg nuclei. Its discovery can be traced back to 1975 when Thibault *et al.* [45] reported anomalously high binding energy in ^{31,32}Na. The region of anomaly was later expanded to include $^{30-32}$Ne, $^{31-33}$Na, and $^{32-34}$Mg and termed the "island of inversion" [46]. Unlike the cases above, this phenomenon cannot be explained by a difference in the occupation of a single orbital. Instead, Warburton *et al.* proposed the root cause to be a culmination of three important factors: (1) a somewhat reduced shell gap, (2) an increase in neutron pairing energy, and (3) an increase in *pn* interaction energy [46]. Factor (1) simply reflects the migration of ESPE's as a function of Z. Here,

Warburton *et al.* did not find an overwhelming trend, although their calculations did posit a somewhat smaller gap than in neighboring nuclei. The neutron pairing energy does not vary appreciably as a function of Z, and can be computed with $E_{nn} = E(0_2^+) - 2E_{gap}$, where $E(0_2^+)$ is the excitation energy of the $2p$-$2h$ intruder state in $^{28}_{8}O_{20}$ calculated from theory, and E_{gap} is the single-particle gap at $^{28}_{8}O_{20}$. Last, the pn interaction energy is dependent on Z, and can be computed from (1) and (2) and the excitation energy of the intruder state of said species: $E_{pn}(Z) = E_x(Z) - 2E_{gap} - E_{nn}$. It turns out that $E_{pn} \approx -3.5$ to -3.9 MeV within the "island of inversion" and ≥ -2.1 MeV outside, according to the calculations of Warburton *et al.* [46]. Here, the pn interaction is dominated by higher multipole components, which is why (a) it cannot be anticipated by the effective single-particle energies, which are calculated from the monopole Hamiltonian, and (b) the region is characterized by strong deformation. Thus, there is a fundamental difference between this case and those denoted above.

Another case that should not escape mention is the study of Dobaczewski *et al.* [47] in which the results of a series of mean field calculations were reported on the $A = 100$ isobars from proton dripline to neutron dripline. These calculations pointed toward an increasingly diffuse system as the neutron dripline was approached. In such a case, one would expect the shell model potential to become more rounded and thus more harmonic oscillator-like. This would have important consequences in the $N = 40$ region, since $N = 40$ is a harmonic oscillator shell closure. Hence, one might predict the onset of a sustained shell closure here in very neutron-rich nuclei.

1.2.2 $N = 40$

Research in the $N = 40$ region has in general been buoyed by the presence of a subshell closure in $^{68}_{28}Ni_{40}$, marked by an elevated 2^+ energy relative to its nearest neighbors [48] and complemented by a low *B(E2)* value [49]. However, interest in this region has in particular been piqued by the immediate disappearance of this subshell gap in $^{66}_{26}Fe_{40}$ in favor of a possible new region of deformation [50]. Although the structure of $^{64}_{24}Cr$ is not yet known, 2^+ energy trends appear to tell a similar story for these isotopes [51]. All of this, of course, gives rise to questions of the role of the $\nu g_{9/2}$ orbital in these nuclei.

One way to probe this problem, as proposed by Mueller *et al.* [52], is to compare the known Ni isotopes with the "valence mirror" $N = 50$ isotones. Since the Ni isotopes have magic number 28 protons, they can be viewed as a closed proton shell with valence neutrons filling the $N = 28 - 50$ shell. On the other hand, the $N = 50$ isotones present a closed neutron shell with valence protons filling the $Z = 28 - 50$ shell. Hence, these two systems are denoted "valence mirrors" of one another. With this in mind, a comparison of the 2_1^+ and 2_2^+ states in these nuclei, illustrated in Figure 1.7, shows a marked consistency in the general trend of these states, except for a marked contrast in the 2_2^+ states beyond $N = 38$. Because of this discrepancy, Mueller *et al.* speculate that the $\nu g_{9/2}$ orbital must therefore have "a larger influence on the collectivity of Ni isotopes than the $\pi g_{9/2}$ orbital has on $N = 50$ isotones." This would imply that there is an isospin dependence to the interaction which promotes the onset of deformation, possibly something analogous to the role of E_{nn} and E_{pn} as discussed for the "island of inversion" species.

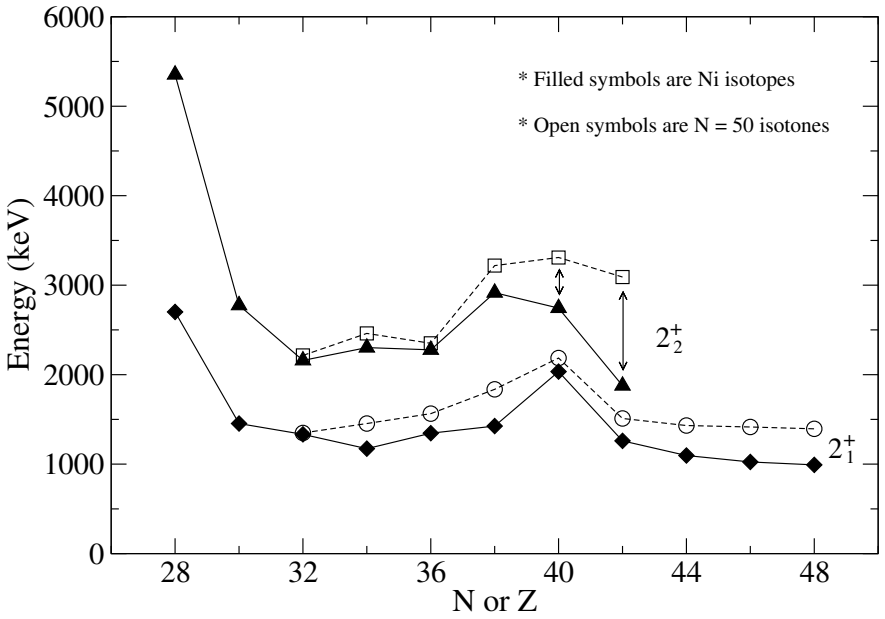

Figure 1.7: The 2_1^+ and 2_2^+ states in the Ni isotopes compare well with those of the $N = 50$ isotones up to N or $Z = 38$, where a large deviation occurs. This figure adapted from Ref. [52].

Drawing from the previous discussion on the tensor force and monopole Hamiltonian, one could also postulate that the sharp change in structure from $^{68}_{28}$Ni to $^{66}_{26}$Fe comes from the loss of $\pi f_{7/2} \cdot \nu f_{5/2}$ interaction strength owing to the lowered occupancy of the $\pi f_{7/2}$ orbital in Fe [53]. In this scenario, the ESPE of the $f_{5/2}$ neutron orbital would rise into and effectively dissolve the already small $N = 40$ subshell gap of $^{68}_{28}$Ni. What is more, this phenomenon would fight against the further development of this harmonic oscillator shell gap in the very neutron-rich nucleus ^{60}Ca.

To understand the evolution of the $N = 40$ shell gap, it is important to obtain a realistic and reliable estimate of the magnitude of the single-particle gap between pf and $g_{9/2}$ orbitals, and how it changes as a function of Z. Additionally, the monopole shift of the $\nu f_{5/2}$ orbital as a function of $\pi f_{7/2}$ occupation must be properly understood. The latter can be quantitatively estimated with the *GXPF1*

and *GXPF1A* effective interactions, as evidenced by their success in reproducing structure related to the $N = 32$ subshell closure [15, 16]. The former is not well established owing to (1) the sparse data for *pf* shell nuclei related to the $\nu g_{9/2}$ orbital and (2) the size of the model space needed to fully assess the role of this orbital in semi-empirical interactions like *GXPF1* and *GXPF1A*. Even so, there have been attempts to determine the matrix elements associated with the $\nu g_{9/2}$ orbital.

Sorlin *et al.* [49] have used an effective interaction based on the *KB3G* matrix elements plus some components related the $\nu g_{9/2}$ orbital that were based on an old G-matrix calculation. The result proved very optimistic in that it could reproduce the *B(E2)* values for Ni isotopes with reasonable accuracy [49]. Results from this interaction have also successfully reproduced 2^+ energy trends in the Fe and Cr isotopes [51] in a very qualitative fashion; namely, the larger model space promoted the lowering of the 2^+ energy at $N = 40$ rather than a peak which is an artifact of the smaller *pf* model space. Those authors also pointedly note that a comparison with experiment is further improved by the introduction of $\nu d_{5/2}$ configurations, a contention raised earlier by Caurier *et al.* [54].

The argument for introducing the $\nu d_{5/2}$ orbital into the model space was to account for the phenomenon of "quadrupole coherence" a term that is not defined by the authors, but seems to ring a tone similar to Warburton's [46] residual $Q \cdot Q$ interactions that were purported to have a strong influence on E_{pn} and the onset of deformation in the "island of inversion".

It is clear by now that the situation at $N = 40$ is liable to be very complicated, and could very well involve a mixture of several important phenomena. It is also

clear that theoretical speculation on the matter would greatly benefit from additional data in this region. For example, new data relating to states beyond the 2_1^+ level and especially those involving the $g_{9/2}$ neutron orbital will provide much-needed data points to test and to improve empirical shell model interactions, which can lead to better predictions and hopefully a more complete understanding of the structural trends near $N = 40$. The scarcity of data necessarily limit the reliability and detail that can be gleaned from current theoretical assessments of the region. To address these issues, the work presented in this thesis has focused on expanding the spectrum of data currently available for the Fe isotopes up to $^{66}_{26}\mathrm{Fe}_{40}$. The purpose of this work, then, is to evaluate the gradual evolution of these isotopes as the νpf orbitals are filled.

Chapter 2

Experimental Methods and Analysis

2.1 Gamma-ray spectroscopy

Radioactive nuclei can emit excess energy through several mechanisms. Some of these mechanisms involve particle emission such as α decay, β decay, neutron or proton emission, and fission, each of which will convert a nucleus into an entirely different system. Alternatively, a radioactive nuclide can decay through the emission of electromagnetic radiation, a process by which excess energy is given off that does not change N or Z of the system. Instead, the nucleus transitions into a less excited state or the ground state.

A photon emitted from an excited nucleus will carry with it a discrete energy and angular momentum, related to the difference in these properties exhibited by the two states that are connected via the transition. The angular momentum, L, carried away by the photon can take on any value represented by the vector sum of

angular momenta of the initial and final states,

$$|J_i - J_f| \leq L \leq J_i + J_f. \tag{2.1}$$

Following the nomenclature 2^L-pole, these are referred to as, for example, dipole for $L = 1$, quadrupole for $L = 2$, etc. In practice only the lowest multipole component contributes significantly to the transition rate for reasons that will be discussed below, although exceptions to this rule are seen in low-multipole transitions.

A γ-ray transition may or may not be characterized by a change in parity (π) of the state from which it originated. Electric (EL) and magnetic (ML) multipole transitions differ in this property via the rule,

$$\begin{aligned} \Delta\pi &= (-1)^L \qquad \text{for } EL \text{ radiation} \\ &= (-1)^{L-1} \qquad \text{for } ML \text{ radiation,} \end{aligned} \tag{2.2}$$

The primary goal of most γ-ray spectroscopic studies is to construct a level scheme which depicts the excited states in a particular nucleus. Once the level scheme is established, the character and spacing of levels can be quite telling. For example, the ratio of 4_1^+ to 2_1^+ states in an even-even nucleus can provide important information regarding the rotational motion of a deformed system, as discussed in section 1.1.4. Moreover, the level scheme can be compared with theoretical predictions, thus providing an indirect, model-dependent method for interpreting structural information. In spite of the model dependency, this is one of the most fruitful discourses following the establishment of a nuclear level scheme. This comes from the supposition that a model which can simultaneously reproduce a detailed level scheme and any number of additional observables must do an adequate job

of representing the complex web of nuclear interactions. Among the "additional observables" is the rate of transition between excited states, which can be related to the quadrupole moment and deformation, as described below.

2.2 Rate of γ-ray emission

The probability of a γ-ray transition from some initial state, $|i>$, to final state, $|f>$, depends on energy, multipolarity, and the overlap of wave functions for these states. For a proper derivation of the operator connecting these two states one must consider Maxwell's equations and the electromagnetic interaction Hamiltonian [7]. With these formulae the Helmholtz equation is derived, which bears as solutions the electric and magnetic transition operators,

$$\begin{aligned} O(M\ LM) &= \frac{-1}{c(L+1)} \int j(r) \cdot [r \times \bigtriangledown r^L Y_{LM}] dr \\ O(E\ LM) &= \int \rho(r) r^L Y_{LM} dr, \end{aligned} \tag{2.3}$$

where $j(r)$ is the current density, $\rho(r)$ is the charge density, and Y_{LM} are spherical harmonics. These equations provide the basis for the derivation of single-particle transition rates known as the Weisskopf estimates, as well as an intimate connection between transition rates, quadrupole moment, and deformation. The probability, P, for a transition from state $|J_i M_i>$ to $|J_f M_f>$ is given in terms of the transition operators as,

$$P(\lambda\ LM; J_i M_i \rightarrow J_f M_f) = \frac{8\pi(L+1)}{\hbar L[(2L+1)!!]^2} \left(\frac{E}{\hbar c}\right)^{2L+1} \langle J_f M_f \left| O(\lambda\ LM) \right| J_i M_i \rangle^2 . \tag{2.4}$$

Here, the terms outside of the transition matrix element come from spherical Bessel functions as a part of the solution to the Helmholtz equation alluded to above [39]. The transition rate, then, is given by the summation of eqn. (2.4) over all M_i, M, and M_f, normalized to $2J_i{+}1$. To average out M it is useful to consider the reduced matrix element which is defined by the Wigner-Eckart theorem,

$$\langle J_f M_f \, | O(\lambda \; LM | \, J_i M_i \rangle = \frac{(J_i M_i L M | J_f M_f)}{\sqrt{2J_f + 1}} \, \langle J_f \| O(\lambda L) \| J_i \rangle \, . \tag{2.5}$$

Then, the transition rate is written in terms of the reduced matrix element,

$$T(\lambda \; L; J_i \rightarrow J_f) = \frac{8\pi(L+1)}{\hbar L[(2L+1)!!]^2} \left(\frac{E}{\hbar c} \right)^{2L+1} \frac{\langle J_f \| O(\lambda L) \| J_i \rangle^2}{2J_i + 1}. \tag{2.6}$$

The transition rate is an observable quantity, related to the mean lifetime τ and half-life, $t_{1/2}$ by $\tau = \frac{1}{T} = \frac{t_{1/2}}{0.693}$. However, most nuclear physics applications tend to use instead the reduced transition probability, defined as the square of the reduced matrix element normalized to $2J_i{+}1$, so eqn. (2.6) can be rewritten,

$$T(\lambda \; L; J_i \rightarrow J_f) = \frac{8\pi(L+1)}{\hbar L[(2L+1)!!]^2} \left(\frac{E}{\hbar c} \right)^{2L+1} B(\lambda L; J_i \rightarrow J_f). \tag{2.7}$$

For a transition of *E2* multipolarity, eqn. (2.7) can be simplified with $\hbar = 6.58 \times 10^{-22} \; MeV \cdot s$, $\hbar c = 197.327 \; MeV \cdot fm$, and $e^2 = 1.44 \; MeV \cdot fm$, noting that the units for EL reduced transition rates are $e^L \cdot fm^{2L}$. Thus, eqn. (2.7) simplifies to,

$$T(E2; J_i \rightarrow J_f) = 1.225 \times 10^9 \cdot E_\gamma^5 \cdot B(E2; J_i \rightarrow J_f), \tag{2.8}$$

where E_γ is the γ-ray energy in MeV and the transition rate is given in s^{-1}.

In a similar vein, single-particle estimates to the transition rate expression (2.6) are determined with the application of some crude approximations to the integrals

of eqns. (2.3) (For details, see section 9.6 of Ref. [7]). First deduced by Victor Weisskopf [55], this set of equations has been termed the "Weisskopf estimates." Simplified expressions based on the Weisskopf estimates are,

$$\begin{aligned} T(EL) &\approx \frac{4.4(L+1)}{L[(2L+1)!!]^2}\left(\frac{3}{L+3}\right)^2\left(\frac{\hbar\omega}{197\ MeV}\right)^{2L+1} \times R^{2L} \times 10^{21} s^{-1} \\ T(ML) &\approx \frac{1.9(L+1)}{L[(2L+1)!!]^2}\left(\frac{3}{L+3}\right)^2\left(\frac{\hbar\omega}{197\ MeV}\right)^{2L+1} \times R^{2L-2} \times 10^{21} s^{-1}, \end{aligned} \tag{2.9}$$

where $R = 1.2A^{1/3}\ fm$. The importance of eqns. (2.9) is in the specific approximation of a single particle transition from one state to the next. Hence, the Weisskopf estimates are alternatively termed the single-particle estimates, and can be used to gauge the single-particle nature of a transition. This is particularly relevant where reduced transition rates are concerned, as they are often quoted in terms of "Weisskopf units" meaning that the measured value has been normalized to the single-particle estimate. A transition rate much larger than this value generally signifies collectivity, and "hindered" values are often encountered in isomeric states. Either way, such comparisons can be quite telling in regard to the intrinsic structure of the nucleus.

Equations (2.9) also allow one to compare the expected lifetime for different multipole transitions. Simplification of these equations yields the expressions given in Table 2.1. Here, it is seen that, for a transition of energy E in a nucleus of mass A, the expected lifetimes for different multipoles differ by orders of magnitude, thus proving the supposition alluded to above whereby only the lowest-multipole transitions will typically contribute to the transition rate.

Table 2.1: Weisskopf estimates for transition rates of different multipolarity. Transition rates are given in units of s^{-1}.

λL	$T(\lambda L)$	
$E1$	1.0×10^{14}	$E_\gamma^3 \; A^{\frac{2}{3}}$
$E2$	7.4×10^{7}	$E_\gamma^5 \; A^{\frac{4}{3}}$
$E3$	3.5×10^{1}	$E_\gamma^7 \; A^{\frac{6}{3}}$
$E4$	1.1×10^{-5}	$E_\gamma^9 \; A^{\frac{8}{3}}$
$E5$	2.5×10^{-12}	$E_\gamma^{11} \; A^{\frac{10}{3}}$
$M1$	3.1×10^{13}	$E_\gamma^3 \; A^{0}$
$M2$	2.2×10^{7}	$E_\gamma^5 \; A^{\frac{2}{3}}$
$M3$	1.0×10^{1}	$E_\gamma^7 \; A^{\frac{4}{3}}$
$M4$	3.3×10^{-6}	$E_\gamma^9 \; A^{\frac{6}{3}}$
$M5$	7.4×10^{-13}	$E_\gamma^{11} \; A^{\frac{8}{3}}$

2.2.1 Relation to quadrupole moment

Once the transition rate is measured or calculated from theory, it can be related to the quadrupole moment with the use of an analytical expression. The quadrupole moment is a mathematical entity derived from the Taylor series expansion of the external potential which acts on a nucleus. This expansion, given in numerous textbooks, results in an expression for the quadrupole moment tensor,

$$Q_{ij} = \int (3r_i r_j - r^2 \delta_{ij}) \rho(r) dr, \tag{2.10}$$

where i and j are indexes denoting the coordinate axes. This expression can be re-written in terms of the spherical harmonic Y_{20} and thus related to the electric

transition operator of eqn. (2.3) so that,

$$\begin{aligned} Q_{ij} &= \sqrt{\frac{16\pi}{5}} \int \rho(r) r^2 Y_{20} dr \\ &= \sqrt{\frac{16\pi}{5}} \frac{(J_i M_i L M | J_f M_f)}{\sqrt{2J_f + 1}} \langle J_f \| O(E2) \| J_i \rangle \\ &= \sqrt{\frac{16\pi}{5}} \begin{pmatrix} J_i & L & J_f \\ -M_i & M & M_f \end{pmatrix} \langle J_f \| O(E2) \| J_i \rangle \,, \end{aligned} \tag{2.11}$$

where the definition of the 3-j symbol was used in the last step. Using the orthogonality relations of 3-j symbols (eqn. 13.59 of Ref. [56]) and the definition of the reduced transition rate, eqn. (2.11) can be rearranged so as to give the *B(E2)* value as a function of the intrinsic quadrupole moment,

$$B(E2) = \frac{5}{16\pi} Q_0^2 (2J_f + 1) \begin{pmatrix} J_i & L & J_f \\ -M_i & M & M_f \end{pmatrix}^2 . \tag{2.12}$$

The nomenclature associated with quadrupole moments can be confusing: there is the intrinsic quadrupole moment, Q_0, which represents the moment in the body-fixed frame of reference; the measured value, $Q(JM)$, in the lab frame; and the spectroscopic quadrupole moment, Q_s, defined as the moment with $J = M$. Confusion arises because the latter two are often used interchangeably. Indeed, it is often the case that $J = M$ and therefore the measured value is equivalent to the spectroscopic value. Using geometrical arguments, the relation between $Q(JM)$ and Q_0 can be derived (See section 11.4 of Ref. [7], section 4-3b of Ref. [6], or section 7.A of Ref. [39] for detailed accounts of intrinsic and spectroscopic quadrupole moments),

$$Q(JM) = Q_0 \frac{3M^2 - J(J+1)}{(2J+3)(J+1)}. \tag{2.13}$$

2.2.2 Relation to deformation

The quadrupole moment is intimately related to the deformation of the nucleus. However, the exact relation depends on the definition of the deformation parameter [31]. One commonly used convention comes from an expansion of the radius, R, in terms of spherical harmonics,

$$R = R_0 \left[1 + \alpha_{00} Y_{00} + \alpha_{20} Y_{20}\right], \tag{2.14}$$

where R_0 is the spherical radius ($R_0 \approx 1.2A^{1/3}$), and a constant volume condition is assumed (*ie:* the volume is assumed to remain constant under deformation). If the charge density is assumed to be constant over the nuclear volume, the term $\rho(r)$ will be equal to $\frac{3}{4\pi} Ze R_0^{-3}$. After integration, eqn. (2.11) can be expressed in terms of the deformation parameter β_2 [31, 57, 58],

$$Q_0 = \sqrt{\frac{16\pi}{5}} \frac{3}{4\pi} Ze R_0^2 \beta_2. \tag{2.15}$$

The deformation parameter β_2 is identical to the coefficient α_{20} of eqn. (2.14) [31].

2.3 Angular correlation of γ rays

Since excited states in nuclei tend to be very short-lived, the time required for the emission of coincident γ rays is generally very short when compared to the physical motions of a stopped nucleus. Therefore, a proper assessment of the angular correlation of γ rays emitted from a given system can be a powerful tool for the determination of characteristics of specific nuclear transitions. The directional cor-

relation of coincident γ rays can be expressed in terms of the LeGendre polynomial,

$$W(\theta) = \sum_{k\ even} A_{kk} P_k(cos\ \theta). \tag{2.16}$$

For pure multipole radiation, the index k is limited by the selection rule,

$$0 < k < Min(2J, 2L_1, 2L_2), \tag{2.17}$$

which arises specifically from the triangular relation of 6-j symbols contained in the expression for A_{kk} [59]. By convention, the terms of eqn. (2.16) are normalized to the value A_{00}, so that,

$$a_{kk} \equiv \frac{A_{kk}}{A_{00}} = \frac{A_k(L_1 L_1 J_i J)}{A_0(L_1 L_1 J_i J)} \cdot \frac{A_k(L_2 L_2 J_f J)}{A_0(L_2 L_2 J_f J)} = F_k(L_1 L_1 J_i J) \cdot F_k(L_2 L_2 J_f J). \tag{2.18}$$

The normalized F_k-factors are given by a collection of angular momentum coupling coefficients,

$$F_k(LLJ_iJ) = (-1)^{J_i+J-1}(2L+1)(2J+1)^{\frac{1}{2}}(2k+1)^{\frac{1}{2}} \begin{pmatrix} L & L & k \\ 1 & -1 & 0 \end{pmatrix} \begin{Bmatrix} L & L & k \\ J & J & J_i \end{Bmatrix}, \tag{2.19}$$

where the last term in brackets is the 6-j symbol.

With the above formalism, one can compute theoretical values for the coefficients and therefore the form of the curves representing different combinations of multipole transitions. The result is illustrated in Figure 2.1 for *E2-E2*, *M1-M1*, and *M1-E2* decay sequences. The normalized correlation coefficients a_{kk} for these cascades are a_{22} = 0.10, a_{44} = 0.01; a_{22} = 0.05; and a_{22} = -0.07, respectively. The two latter do not possess a_{44}-coefficients due to the selection rule of eqn. (2.17). It should be emphasized that, without a measurement of the polarization of the

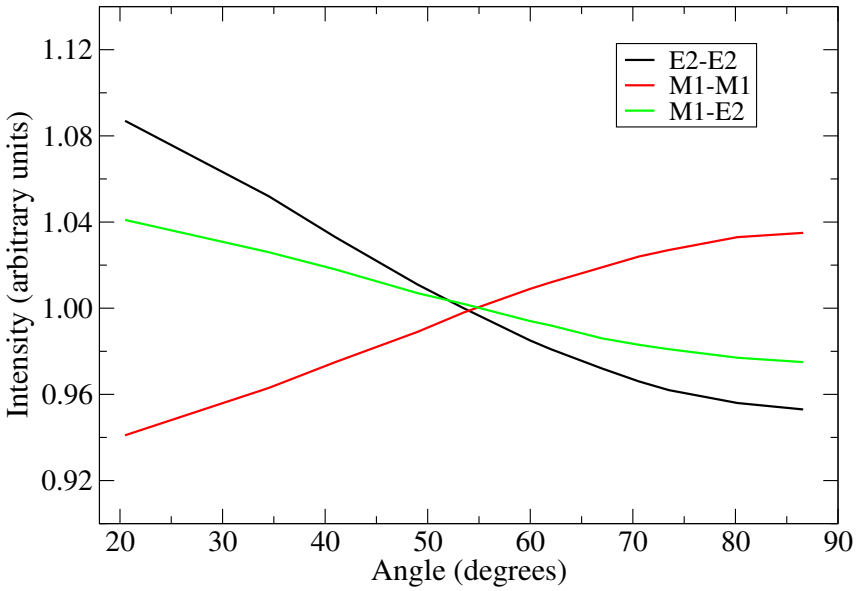

Figure 2.1: Theoretical angular correlation curves for pure E2-E2, M1-M1, and M1-E2 cascades. Sequences used in the calculation of these curves were $4 \rightarrow 2 \rightarrow 0$, $2 \rightarrow 1 \rightarrow 0$, and $3 \rightarrow 2 \rightarrow 0$, respectively.

detected γ-radiation, the parity of the transition cannot be determined, so that the above might instead be represented by Q-Q, D-D, and D-Q symbols, where Q denotes a quadrupole transition and D denotes a dipole transition. Note that Q-Q and D-D cascades show qualitatively similar angular correlation curves, but quantitatively different coefficients. These are not always discernable from experiment since the uncertainties associated with experimental values are often large enough to make this distinction ambiguous. However, one often begins an experimental analysis with transitions of known multipolarity, so that it is, in most cases, trivial to distinguish whether a cascade is Q-Q or D-D.

The possibility of mixed-multipole transitions represents an added difficulty for any angular correlation analysis. This can be addressed with the introduction of the mixing amplitude, δ, which is defined as the ratio of reduced matrix elements

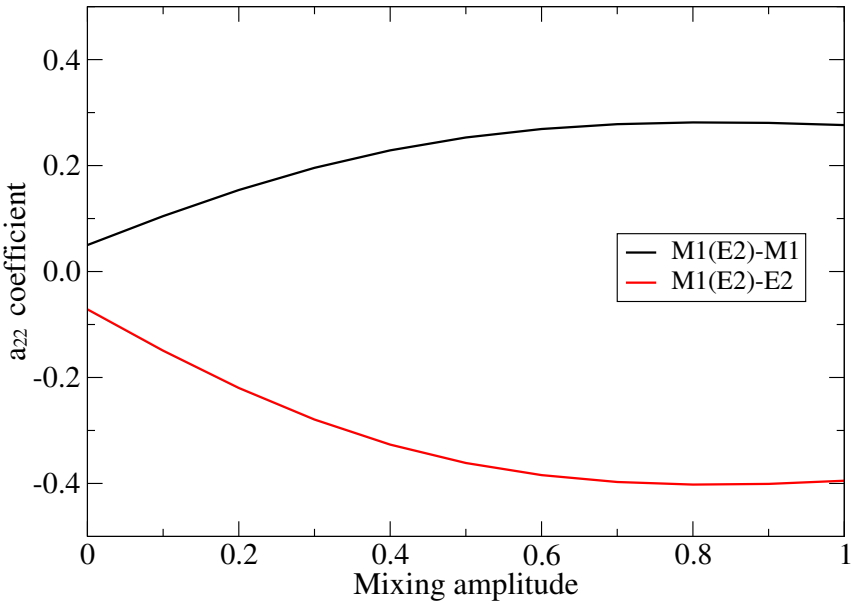

Figure 2.2: Variation of a_{22} coefficient as a function of mixing amplitude, δ. Calculations are based on eqns. (2.18), (2.19), and (2.20).

for each multipole. This leads to an expression for the correlation coefficient [59],

$$A_k(L_1 L_1^{'} J_i J) = \frac{F_k(L_1 L_1 J_i J) + 2\delta_1 F_k(L_1 L_1^{'} J_i J) + \delta_1^2 F_k(L_1^{'} L_1^{'} J_i J)}{1 + \delta_1^2}. \qquad (2.20)$$

Since the Weisskopf estimates of Table 2.1 pointed to a very small likelihood of anything other than transitions of the smallest possible multipole, the question of mixed transitions is not often an issue. However, numerous cases of *M1(E2)* mixing have been identified, so this is by no means something that can be ignored completely. The effect of eqn. (2.20) on the a_{22} coefficient is plotted in Figure 2.2 as a function of the mixing amplitude for *M1(E2)-E2* and *M1(E2)-M1* cases. Here, it is seen that the advent of multipole mixing has the effect of increasing the a_{22} coefficient up to $\delta \sim 1.0$.

2.4 Detection and measurement of γ rays

2.4.1 Interactions with matter

γ rays interact with matter primarily through the processes of photoelectric absorption, Compton scattering, and pair production. Of these, photoelectric absorption is the most important for assessing the quantitative features of detected radiation, since it involves the complete absorption of photon energy by an electron or electrons. Thus, the energy transferred to an electron is proportional to the energy of the photon or, alternatively, the number of electrons excited is proportional to the photon energy. The process of Compton scattering, on the other hand, involves incomplete absorption of the photon energy and the consequent scattering of the original photon at some angle θ. The energy of the electron can be related to the initial energy of the photon through its relationship with the angle θ, but in most cases the scattered photon is not detected, so the information is lost. The last mechanism, pair production, is important at higher energies, where the energy of the photon is more than twice the rest mass energy of an electron (2×0.511 MeV/c^2). It is therefore possible for the photon to convert its energy to the production of an electron-positron pair, whose kinetic energy reflects the difference between the photon energy and 1.022 MeV.

The relative importance of each mechanism is dependent on the energy of the photon and on Z of the absorbing material. This is reflected in Figure 2.3, over the region of interest to most nuclear structure applications. It is seen that Compton

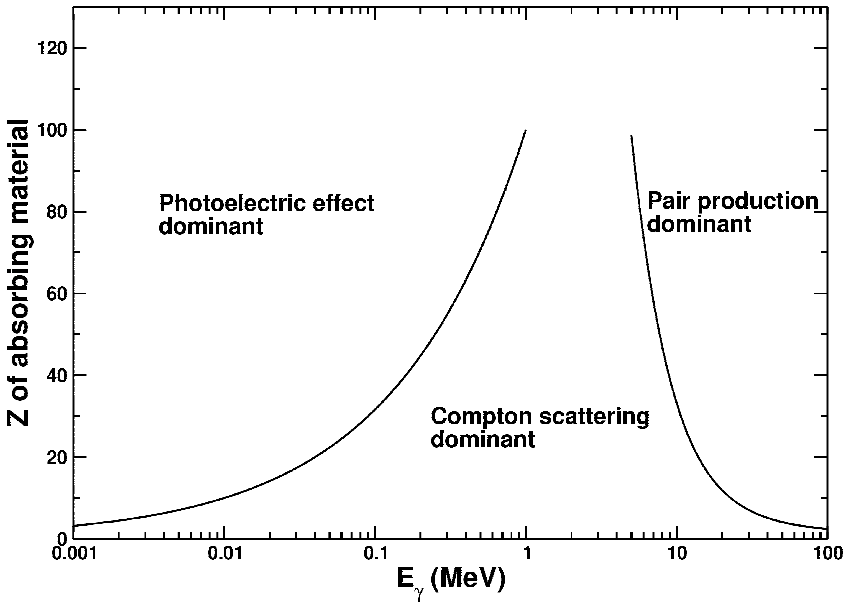

Figure 2.3: The interaction of γ radiation with matter depends on both the Z of the absorbing material and the energy of the radiation [60].

scattering dominates much of this region, enough so that it could represent a problem for some γ-ray spectroscopy experiments. One solution to this problem is addressed in the next section, where a method to suppress Compton scattered events from the recorded data is described.

When it comes to a quantitative measurement of the energy of γ radiation, semiconductors are far and away the best materials. The reason for this comes from the relatively small but important energy gap between so-called valence and conduction bands in these materials. An insulating material can be characterized by a large such gap, so that electrons are tightly bound and do not move freely about in a material. Conductors are the opposite, as the electrons tend to flow freely about in the conduction band. In semiconductors, electrons generally occupy the valence band, where they form the bonds that hold the material together in a crystalline structure. However, the energy required to excite an electron into the conduction

band is relatively small, so thermal excitations can easily surmount this energy gap. For γ-ray spectroscopy, high-purity Ge detectors are most often used, since the energy gap is $\sim$0.7 eV, compared to $\sim$1.1 eV for the well-known semiconductor Si [60]. A smaller gap means a higher probability for thermal noise, but this can be suppressed by cooling the material with liquid nitrogen. Since the number of electrons promoted from the valence band to the conduction band is proportional to the energy of the photon, the smaller gap exhibited for Ge translates to better energy resolution in the detected signal, once thermal noise is suppressed.

Another important characteristic of semiconductor detectors is the very short charge-collection time stimulated by a high electron mobility in the material which translates into fast timing signals. This feature enables the measurement of coincidences, a reduction in signal pile-up, and better detector resolution.

Note that the principles of γ-ray detection are far more complex than has been represented here. For a more detailed summary of such methods, see Ref. [60].

2.4.2 Compton suppression

As mentioned above, the dominant interaction mechanism of γ radiation throughout most of the energy region of interest to nuclear structure studies is, unfortunately, Compton scattering. This has a large effect on the observed spectrum as many of the detected γ rays are recorded with an energy much lower than the actual energy of the photon, the result being an accumulation of low-energy background that can obscure real peaks. To ameliorate this problem, many applications

have adopted the use of high-Z materials as scintillators to serve as anti-coincidence shields, in order to suppress events in which γ rays are scattered out of the detector. Most often, the material Bismuth Germanate ($Bi_4Ge_3O_{12}$, referred to as "BGO") is used for which it is well suited because of its scintillating properties, high Z and high matter density (7.13 g/cm^3). Because of the latter two characteristics, BGO forms a highly efficient detection medium, but since the detection mechanism is based on scintillation, the energy resolution is rather poor. Nevertheless, this material is ideal for the rejection of Compton-scattered events, where the exact energy of the scattered photon is unimportant.

The effect of Compton suppression on the resultant spectrum from a ^{60}Co source is illustrated in Figure 2.4. Here, many artifacts can be seen not just from Compton scattering, but from the many phenomena encountered in a real experiment. For example, a cluster of sharp peaks is evident at low energy, which arises from x-rays emitted from the BGO scintillators. Second, a fairly small peak at $\sim$200 keV comes from the backward scattering of γ rays from materials behind the detector. Third, a sharp peak at 511 keV comes from positron annihilation as a result of pair production, which is most likely induced in the high-Z BGO detectors. The overall shape of the background in the unsuppressed spectrum results from the continuum of energies exhibited by Compton scattered photons. The edge of this, termed the "Compton edge", is generally located at an energy $\sim$256 keV below that of the incident γ ray, or half the rest mass energy of an electron [60]. Two such edges are seen in the spectrum of Fig. 2.4 since there are two strong peaks in ^{60}Co decay, at 1173 and 1332 keV, respectively.

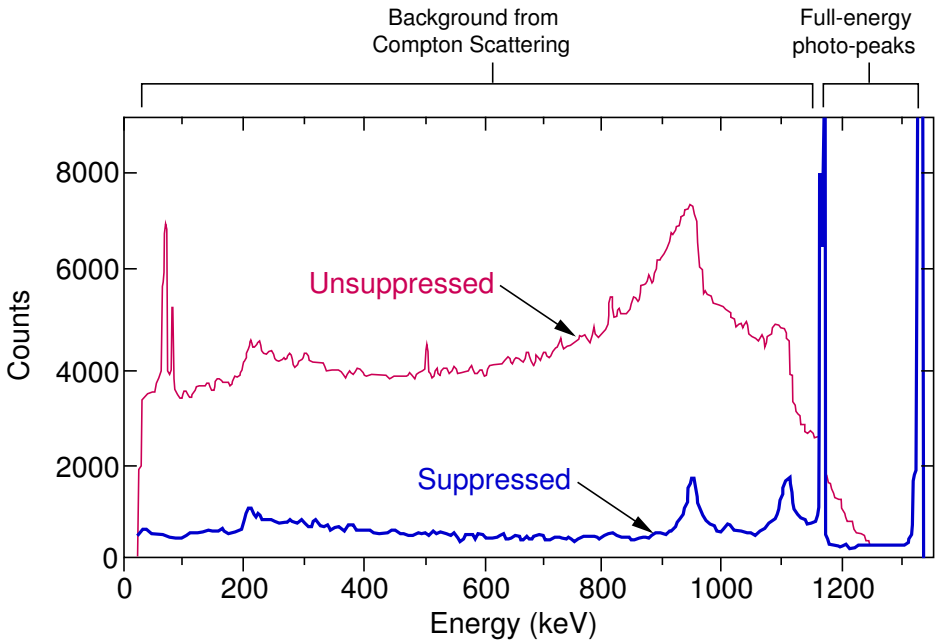

Figure 2.4: Comparison of spectra obtained with and without Compton suppression.

2.4.3 Gammasphere

Gammasphere [61] is an array of Ge and BGO detectors spanning the complete 4π geometry around a focal point, where the target chamber or source material is mounted. The complete array can fit up to 110 detector modules, each mounted to a fixed position on the frame, so that the exact location of each is constant and reproducible in case the detectors need to be removed. Each module consists of a cylindrical, 7 cm diameter $\times$ 7.5 cm long Ge crystal surrounded by a BGO shield optically separated into six components plus a backplug. The six BGO components are flat and wedge-shaped, as depicted in Figure 2.5, shaped to a hexagon so that each detector module can be efficiently set into position. The backplug covers the rear of the Ge crystal except for the space required for the cold finger, which extends into the crystal from the liquid nitrogen dewar in order to keep the detector cool.

The full array consisting of 110 detector modules provides an effective coverage of 46% of the solid angle, since each Ge detector covers 0.418% [62].

For the experiment described in this thesis, each detector was fitted with a 3-cm-thick tungsten alloy material known as a Hevimet shield, which covers the BGO face so as to reduce the probability for false vetoes resulting from direct hits in the BGO detectors by γ rays originating at the target. In addition, a sequence of Ta, Cd, and Cu absorber foils were installed across the face of each detector in order to reduce the flux of x-rays entering the Ge crystals.

γ-ray detector performace is often gauged by the resolving power, which is proportional to the ratio,

$$R \propto \frac{(P/T)}{\Delta E_\gamma}, \tag{2.21}$$

where (P/T) is the peak-to-total, a ratio of total photopeak events to total events, and ΔE_γ is the peak width, determined from the intrinsic resolution of the detector. In an escape-suppressed array like Gammasphere, the former is dramatically increased due to the reduction of Compton scattered events, such that improvements from $\sim$25% for unsuppressed to $\sim$60% for suppressed detectors have been measured [63]. The total efficiency of the complete array is reported to be 9.4% at 1.3 MeV [62], although this value is highly dependent on the γ-ray energy. An efficiency curve specifically tailored for this experiment will be calculated later.

Figure 2.5: Schematic depiction of the layout of Gammasphere detector modules and of the types of interactions between γ rays and the detector material.

2.5 Spectroscopy with deep-inelastic reactions

The production and subsequent investigation of neutron-rich exotic nuclei can be particularly challenging, as most traditional techniques must necessarily make use of stable beam-target combinations or, otherwise, do not yet have sufficient resolving power to permit the analysis of prompt de-excitations. For example, much can be gleaned from fusion-evaporation and particle-transfer experiments, but these necessitate the use of relatively intense beams, of which only stable species are currently available. Alternatively, one can turn to the use of fragmentation, spallation, or fission experiments, where very exotic species can be produced, but the prompt analysis of such species is negated by a need to separate and isolate the desired products. In this work, where the focus is on the prompt decay properties of moderately neutron-rich Fe isotopes, one must turn to the use of deep-inelastic reactions.

The microscopic details of deep-inelastic reactions have been the subject of extensive study [64], but there is, at present, no adequate theoretical tools available to guide experimental pursuits of nuclear spectroscopy with these reactions; nevertheless, the application of such experiments to nuclear structure studies has led to a number of new discoveries in recent years. For example, the identification of an elevated 2^+ state in ^{68}Ni, as discussed in section 1.2.2, was the result of an early application of deep-inelastic reactions [65]. A schematic illustration comparing the deep-inelastic collision process with other nuclear reaction mechanisms is given in Figure 2.6. The distinguishing feature in this schematic is the "neck" that forms between projectile and target species. This differs from a complete fusion experi-

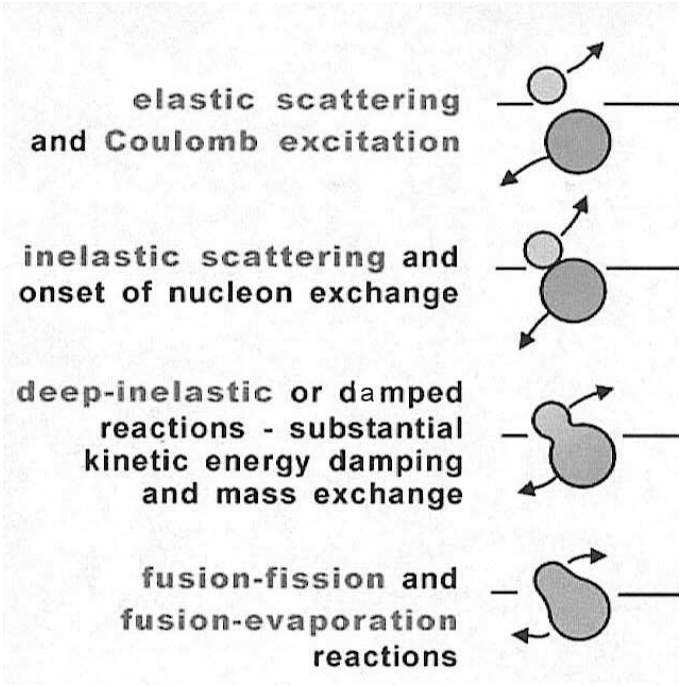

Figure 2.6: Schematic diagram of nuclear reaction mechanisms. The interaction energy increases toward the bottom of the figure.

ment in that the colliding systems maintain projectile- and target-like properties, but are unlike simple particle-transfer reactions in that they can potentially involve the transfer of a large number of nucleons.

Another unique feature of this kind of reaction is the tendency toward N/Z equilibration [64, 66]. It has been noted that the reaction products in deep-inelastic experiments tend to equilibrate toward the N/Z ratio of the composite system, although this is only a tendency and not a concrete rule, possibly attributed to the dynamic shape of the colliding system [66], or possibly due to a relatively short interaction time. Nevertheless, this empirical rule is useful for the design of experiments when the goal is to study weakly-produced nuclei.

An important question that remains is how to successfully identify γ-ray transitions associated with specific reaction products, since a broad array of nuclei are

produced in these experiments. To do this would seem to require some correlation of detected radiation with particle recoils detected downstream from the target position. With the current setup at Argonne National Laboratory, where Gammasphere is positioned in front of the Fragment Mass Analyzer (FMA), the small acceptance of this instrument makes this method forbiddingly inefficient. Although experiments with the Chico charged particle detector in conjunction with Gammasphere have been carried out, a simpler approach is to use a thick target, so that the reaction products are stopped within the target chamber. Here, the high resolving power of Gammasphere can be used to identify reaction products based on coincidence relationships with previously-known transitions. Furthermore, depending on the nature of the target nucleus, the cross-correlation of target-like and projectile-like product transitions can assist in isotopic identification [67]. However, in the pursuit of neutron-rich nuclei, the principle of N/Z equilibration often leads to a need for neutron-rich target nuclei that happen to undergo spontaneous and beam-induced fission. In such cases, the method of cross-correlations does not work, since the complex array of fission products washes out any correlations, which are weak to begin with. Hence, the primary weakness of any deep-inelastic reaction experiment lies in a sometimes ambiguous method of isotope identification. The removal of this ambiguity often depends on the identification of at least two γ-ray transitions with the use of a different technique such as β decay.

A final point regarding experimental design relates to the energy required to induce a deep-inelastic collision. Initial studies of deep-inelastic reactions showed that they become important for heavy ions colliding at energies $\sim$10% above the

Coulomb barrier [64]. However, in thick-target deep-inelastic reaction experiments, one always uses an energy closer to ∼25% above this barrier. This way, the slowdown due to peripheral Coulomb interactions does not immediately eliminate the chance that a deep-inelastic collision takes place. Instead, the effective thickness of the target is maximized and the probability for the desired reaction to take place is larger (with reaction taking place roughly in 1/2 target thickness).

Because of the nature of the mechanism of deep-inelastic reactions, the product nuclei are generally populated at high angular momenta, and the prompt decay follows primarily through the yrast levels (the lowest energy of a given spin, J). This follows from the energy dependence of γ-ray transitions, as detailed in Table 2.1, namely that the transition rate scales with energy raised to some power, which depends on the multipolarity of the transition. However, in a typical experiment only the levels up to $J \sim 10$ can usually be identified, since many of the higher-lying transitions proceed faster than the stopping time in the target.

2.6 Experiment and Data Analysis

2.6.1 Experimental details

Ion beams are produced and accelerated with the Argonne Tandem Linear Accelerator System (ATLAS). This system is composed of an Electron Cyclotron Resonance (ECR) ion source, in which neutral atoms are ionized by plasma electrons accelerated in a bath of microwave radiation. The ionized particles are injected into a

booster linac and finally into the main ATLAS beamline, where they are accelerated in a series of 62 superconducting niobium resonators, while focus is maintained by superconducting solenoids. Particle velocity is controlled by adjusting the relative phases of each resonator, and beam energies up to 17 MeV/u can be attained for ions from hydrogen to uranium.

For this experiment (ANL experiment 1104, gsfma166), a Ni source material was used to produce an ion beam of ^{64}Ni accelerated at a charge state 15^{+} to an energy of 430 MeV. Beams are generally produced in bunches separated by 82 ns, but for this experiment only one of every five bursts was allowed to enter the experimental area, so that an effective separation of 410 ns between bursts was achieved. The beam was incident on a 55 mg/cm^2 thick target of isotopically enriched ^{238}U mounted in a position at the center of Gammasphere. For the duration of the experiment, $\sim$100 detector modules were present (during the experiment one of the detectors was switched off to reduce noise originating from that module which had the effect of increasing dead time in the acquisition system). A beam current between 3 and 7 enA was maintained for five days (3-7 October, 2005). For most of this time the acquisition trigger was three coincident γ rays, although $\sim$14 hours of data were collected under a two-fold coincidence requirement. The data were recorded to Sony QG-112M 8mm data tapes, and later transferred to disk for analysis.

2.6.2 Data collection and analysis

As noted above, there was a three-fold coincidence threshold maintained for most of the experiment. A three-fold coincidence is defined here as three successive signals recorded within 1 μs of the first signal. Once this condition is met, these data and any additional Compton-suppressed γ rays detected within the 1 μs time window are recorded as an event. In addition to the energy signals, the time relative to an RF pulse is recorded for each of the detected γ rays, yielding the time spectrum illustrated in Figure 2.7. Here, two additional peaks are evident, which correspond to subsequent beam bursts, separated by 410 ns. The slow exponential decay of background radiation following the initial burst is also evident in this spectrum (note that, due to the nature of experimental setup, time increments backwards in this picture).

The analysis of data from this experiment was carried out primarily within the Radware software package, which includes an array of programs tailored to the analysis of high-fold γ-ray coincidence experiments. For organizational purposes, a flow chart of the analysis is depicted in Figure 2.8. Here, the programs used to generate coincidence cubes and angular correlation curves, as described in the following sections, is presented. In this figure, programs suffixed with * are a part of the Radware package, **.cc* are custom codes, *root* refers to the software developed at CERN [68], and GSSORT is a program written specifically to sort Gammasphere data.

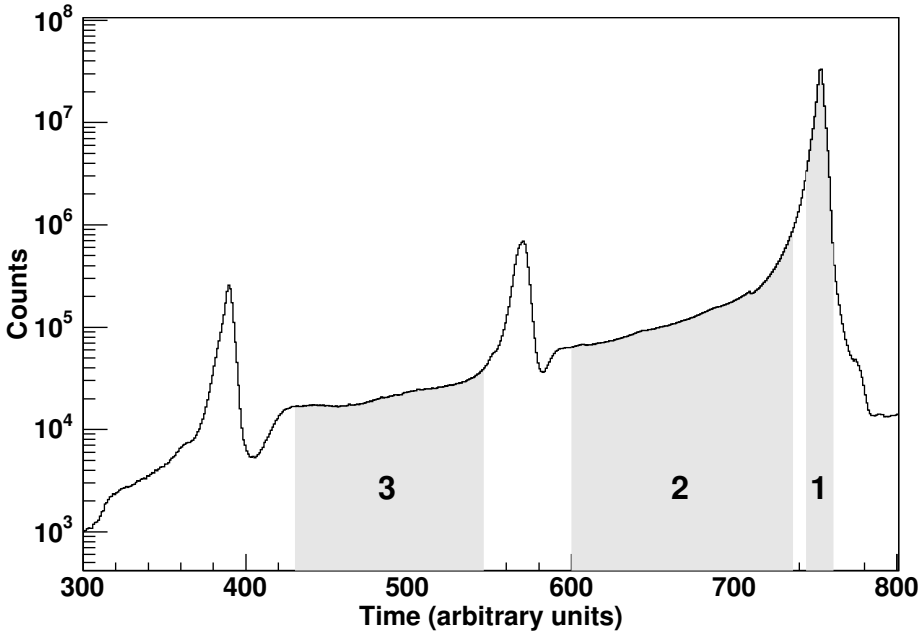

Figure 2.7: The time with respect to an RF pulse for a selected group of γ-ray signals. Shaded region 1 depicts the "prompt" flash of radiation arriving with the beam pulse. Regions 2 and 3 indicate "delayed" transitions which arrive between beam pulses. Note that time increments backwards in this spectrum.

Coincidence cubes

Three regions are labeled on the time spectrum of Figure 2.7. These regions have been used in order to classify a recorded γ ray as "prompt" or "delayed." Prompt events are defined as those which arrive within the initial flash of radiation that is emitted during a beam pulse, and delayed events are those which arrive between subsequent beam bursts. Since γ-ray events are recorded for a full microsecond after an initial signal is detected, radiation emitted over a span of several hundred nanoseconds can be correlated. Thus, four different classes of triple-coincidence events are defined: (1) *prompt-prompt-prompt* (PPP), in which all three associated γ rays arrive within region 1 of Fig. 2.7, (2) *prompt-prompt-delayed* (PPD), whereby

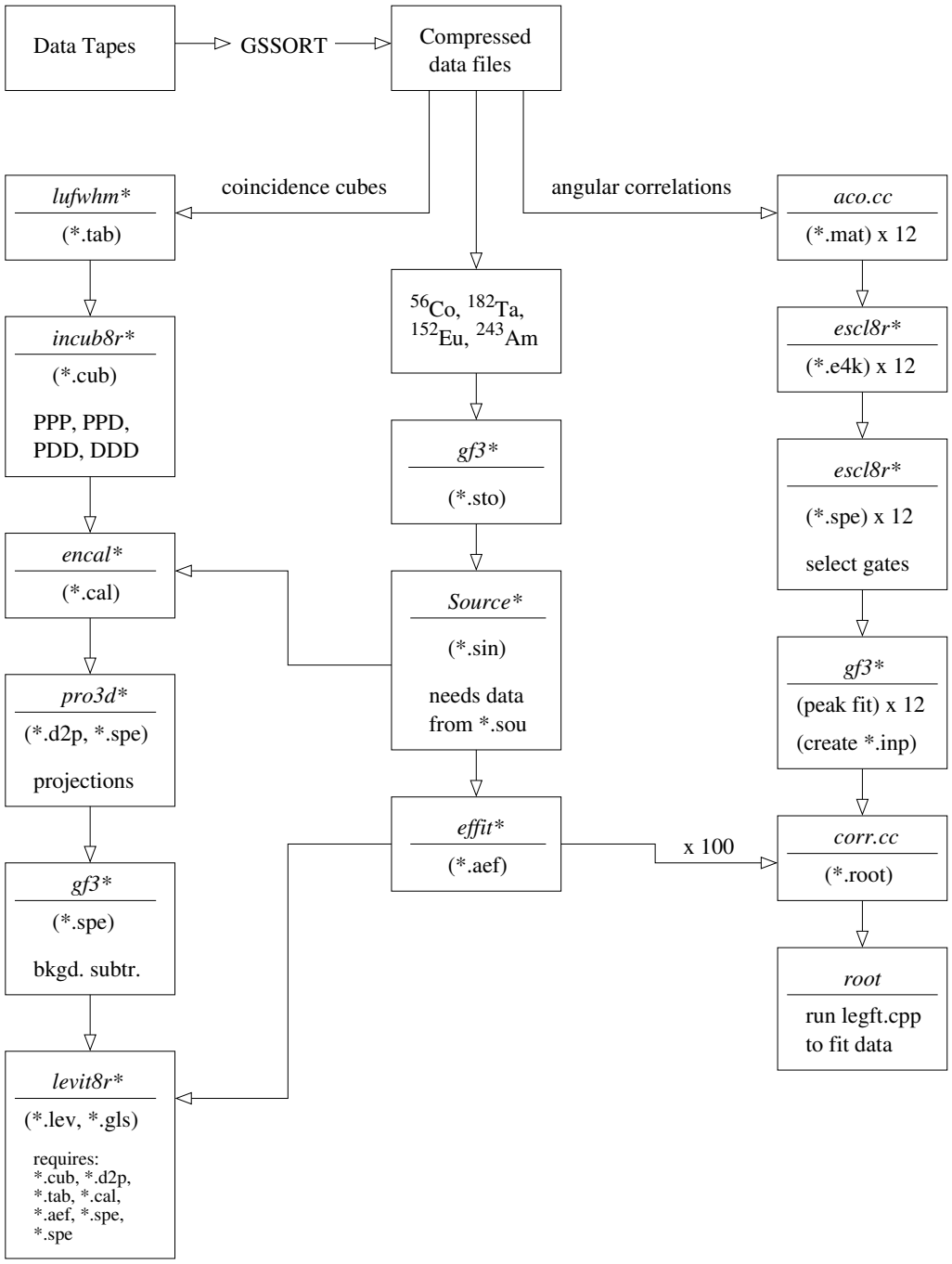

Figure 2.8: A flowchart illustrating the programs used in sequential order for the analysis. Programs suffixed with * are a part of the Radware package, **.cc* are custom codes, GSSORT is a program written to sort Gammasphere data, and *root* is a data analysis program written at CERN [68].

two γ rays are recorded in region 1 and a third in region 2 or 3, (3) *prompt-delayed-delayed* (PDD), where one γ ray is observed in region 1 and the others in region 2 or 3, but in prompt coincidence with one another, and (4) *delayed-delayed-delayed* (DDD), in which all three associated γ rays arrive in region 2 or 3, but in prompt coincidence with one another. In this scheme, "prompt coincidence" means that the events must come within $\sim$40 ns of one another. Note that the peak intensity of the second beam burst in Fig. 2.7 is roughly two orders of magnitude less than that of the principal burst; this means that only one of one hundred beam bursts produces a reaction and, thus, only a remote possibility exists for contamination of γ rays detected in region 3 of that figure. Based on the above classification, four symmetric coincidence cubes were constructed with the *incub8r3* program of the Radware package [69].

Energy and efficiency calibration

An energy calibration was performed prior to the experiment so that all 100 detectors could be properly aligned. This was monitored periodically throughout the experiment in case of gain shifts. Offline, a raw calibration was carried out with a ^{152}Eu source.

The relative efficiency of Gammasphere was measured by placing, separately, four radioactive sources (^{56}Co, ^{152}Eu, ^{182}Ta, and ^{243}Am) at the target position and acquiring data until sufficient statistics were achieved. In each case, peak areas were determined for several known γ-ray transitions, and the measured values were

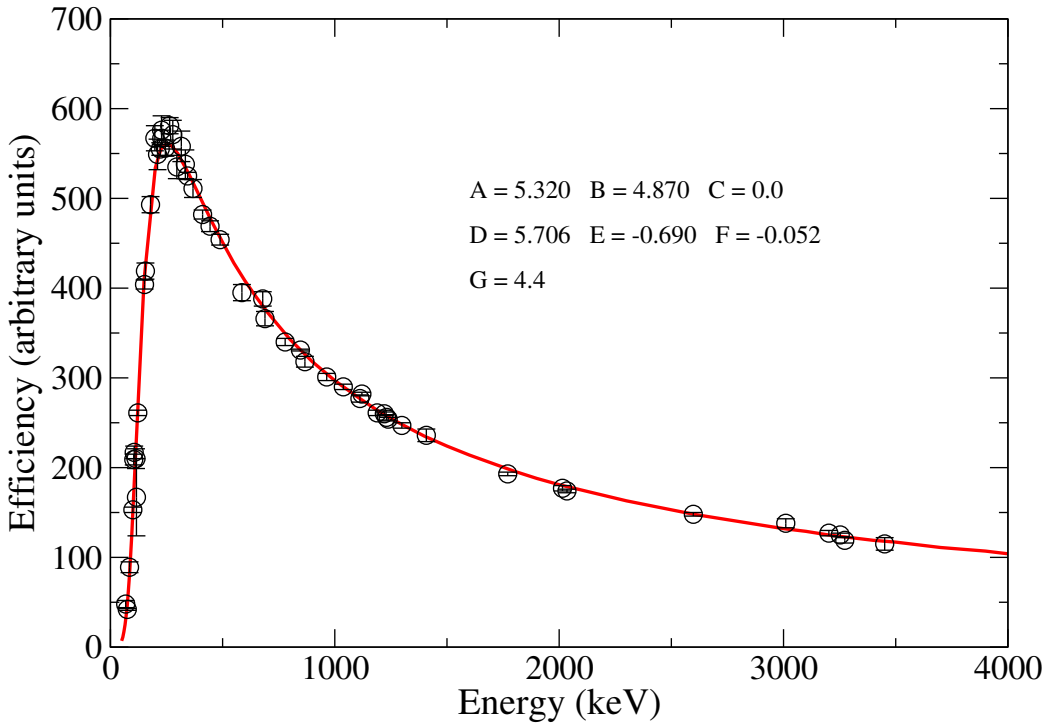

Figure 2.9: The efficiency curve derived from a fit to equation (2.22); parameters used for this fit are provided on the figure. Data points are from ^{56}Co, ^{152}Eu, ^{182}Ta, and ^{243}Am sources.

compared to the known relative intensities. To compare the results from each case, a scaling factor was introduced so as to minimize the χ^2 value for a fit to the equation,

$$\epsilon = exp\left\{\left[(A + Bx + Cx^2)^{-G} + (D + Ey + Fy^2)^{-G}\right]^{\frac{1}{-G}}\right\}, \qquad (2.22)$$

where $x \equiv ln\left(\frac{E_\gamma}{100}\right)$ and $y \equiv ln\left(\frac{E_\gamma}{1000}\right)$. Once the results from all sources were combined to a single dataset spanning an energy range from 67.8 to 3451 keV, the curve depicted in Figure 2.9 could be obtained with the parameters indicated. The coefficient C was fixed to zero, leaving six variable parameters from which a $\chi^2 = 4.7$ was achieved.

Angular correlation analysis

The procedure followed in this work to determine angular correlation coefficients was to (1) sort the data into coincidence matrices, each representing a range of angles between emitted radiation; (2) gate on the γ ray of interest and find the peak area of the appropriate coincident transition or transitions for each angular bin; and (3) fit the efficiency-corrected data to eqn. (2.16) in order to obtain a_{22} and a_{44} angular correlation coefficients. The details of this analysis are given below.

The angle between γ rays emitted from a point at the center of Gammasphere to detectors at positions i and j can be computed from the law of cosines,

$$\vec{u}_i \cdot \vec{v}_j = |u_i|\,|v_j|\,cos\Theta_{ij}, \tag{2.23}$$

where $\vec{u}_i$ and $\vec{v}_j$ are the vectors depicting the emission of γ rays from the target position to i and j, respectively, and Θ_{ij} is the angle between these vectors. Since each detector is fixed at a position along a sphere, the magnitude of these vectors is the same and $|u_i|$ and $|v_j|$ can be arbitrarily normalized to 1. Spherical coordinates are defined by,

$$\begin{aligned} x &= r\ sin\ \theta\ cos\ \phi \\ y &= r\ sin\ \theta\ sin\ \phi \\ z &= r\ cos\ \theta, \end{aligned} \tag{2.24}$$

where the polar angle, θ, is measured with respect to the downstream beam axis, and the azimuth angle, ϕ, is measured from the downward vertical axis. Combining eqns. (2.24) with the explicit form of the dot product and eqn. (2.23), the angle

between two emitted γ rays can be derived,

$$\Theta_{ij} = cos^{-1}\left(sin\theta_i\ sin\theta_j\ cos(\phi_i - \phi_j) + cos\theta_i\ cos\theta_j\right). \tag{2.25}$$

Since the position of each detector module in Gammasphere is known, the determination of Θ_{ij} is easily computed with eqn. (2.25) once the specific detectors are identified. Under these auspices, the data were sorted into twelve matrices depending on the angle derived between the modules in which the signals were detected. The total number of 2-fold detector combinations can be computed with the binomial coefficient,

$$\left(\begin{array}{c} n \\ k \end{array} \right) = \frac{n!}{k!(n-k)!}. \tag{2.26}$$

For the current experiment, eqn. (2.26) gives 4950 possible combinations. By omitting detectors 1-6, 10, 53, 58, and 67, the distribution of Θ_{ij} is presented in Figure 2.10. In this picture, angles greater than 90° have been represented by 180° - Θ_{ij}, since all correlation curves are symmetric about 90°.

It is clear from Fig. 2.10 that each of the twelve angular matrices derived in this work are characterized by varying degrees of statistics, since the distribution of angular data is not uniform. Specifically, the bins with the fewest possible detector combinations contained the fewest events and therefore the highest relative error (for this reason, two of the bins, labeled 4 and 7 in Fig. 2.10, were omitted from the analysis). With this in mind, the data from each bin could only be compared after the fitted peak areas were corrected for the relative efficiency of that bin. To determine this, a curve similar to that illustrated in Fig. 2.9 had to be constructed for each detector, and the relative efficiency of measuring a γ-ray coincidence of

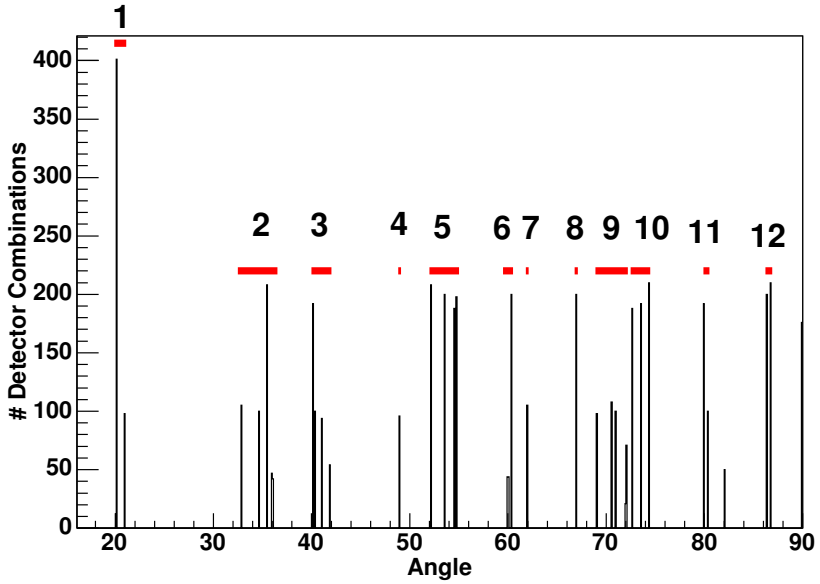

Figure 2.10: The distribution of possible angles between detectors with the 100-detector setup used for this experiment. Horizontal lines depict the angular bins used for the construction of correlation curves. Bins 4 and 7 exhibited very low statistics and were omitted from the analysis reported in this work.

energies e_1 and e_2 in angular bin n is given by,

$$\epsilon_n(e_1, e_2) = \sum_{i,j} \epsilon_{ij}(e_1, e_2) = \epsilon_i(e_1)\epsilon_j(e_2) + \epsilon_i(e_2)\epsilon_j(e_1), \tag{2.27}$$

where the labels i and j indicate the modules in which the radiation was detected. To compare different bins, the value from eqn. (2.27) must be normalized to,

$$\sum_{n=1}^{12} \epsilon_n(e_1, e_2). \tag{2.28}$$

Peak fitting and error analysis

Finding the area under a γ-ray peak can be somewhat complex. The reasons for this are numerous, but what is of most immediate concern is the possibility of incomplete charge collection which is typically caused by neutron damage or by the presence of detector impurities. This will tend to produce a more gradual slope on

the low-energy side of the peak curve and, as a result, the data for a given peak may appear somewhat asymmetric which can be problematic for simple peak-fitting routines. Instead, a skewed Gaussian function may be used, which can reproduce this asymmetry quite well. In spite of this, all peak areas derived from this work have been carried out with a symmetric Gaussian function,

$$G(x) = y_0 \; exp\left[-\frac{(x-x_0)^2}{2\sigma^2}\right], \tag{2.29}$$

where y_0 is the height at the centroid position, x_0. The standard deviation of the Gaussian, σ, is related to the peak area by $A = \sqrt{2\pi} y_0 \sigma = 1.064 y_0 \Gamma$, where Γ is the full width at half maximum. To show that this simple curve is sufficient for the current dataset, a peak from ^{152}Eu source data is reproduced in Figure 2.11. Here, the simple Gaussian function adequately reproduces the observed peak produced from a 964-keV γ ray. Fitting parameters included a constant background of 2976 counts, and $\Gamma = 7.621$.

Under normal circumstances, counting statistics obey a Poisson distribution, and the standard deviation of any peak area is the square route of that area. However, in an experiment such as the one described here, the spectra undergo significant modification, particularly from background subtraction, and the uncertainties are more complicated to evaluate. For instance, a γ ray of interest might overlap with another very intense γ ray in the total projection spectrum, whereas a different γ ray might be comparatively clean. It is then reasonable to postulate that the intensity determined for the former transition should be regarded as less certain than that of the latter. Hence, a proper evaluation of the uncertainty associated with

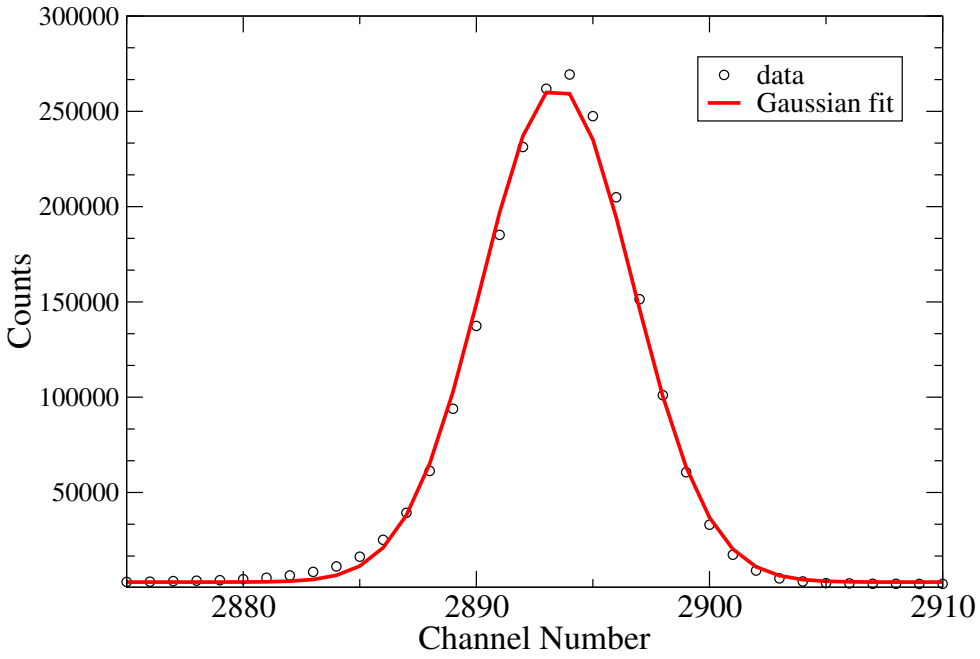

Figure 2.11: Sample Gaussian fit to the 964-keV peak of a ^{152}Eu source spectrum.

each channel number in a background-subtracted spectrum is given by the sum of variances of each spectrum,

$$\sigma_{spe}^2 = \sigma_0^2 + \sigma_{bkgd}^2, \tag{2.30}$$

where σ_{spe} is the standard deviation obtained from the background-subtracted spectrum, σ_0 is from the original spectrum, and σ_{bkgd} is from the background spectrum. The variance being the square of the standard deviation means that σ^2 is simply the number of counts, $C(n)$, in a given channel, n, of a particular spectrum so,

$$\sigma_{spe} = \sum_n \sqrt{C_0(n) + C_{bkgd}(n)}. \tag{2.31}$$

In some cases, the fitting procedure carried out by the program *gf3* is less consistent for repeated fits to the same peak, so instead of the above method, the variation in successive attempts at fitting the peak gives a more realistic indication of the peak area uncertainty. This method is applied where peak areas are very

large, or when the background is very complex even in the background-subtracted spectrum. In these cases, the standard deviation of three successive attempts at fitting the peak is larger than that the value computed with equation (2.31), so the latter method is adopted.

Chapter 3

Results

3.1 Total projection spectra

Each of the four coincidence cubes is projected into a 1D histogram in Figure 3.1. In these spectra, one can identify the main contaminants as well as the most strongly-produced species for each analysis technique. The PPP, PPD and to a lesser extent, the PDD cubes, show a strong effect from neutron-induced reactions on the detector apparatus. The most obvious feature comes from $(n, n'\gamma)$ reactions in the germanium crystal itself, which are visible from the 2^+ energy peaks for all of the naturally-occurring isotopes of Ge, each with a high-energy tail that represents the recoil energy gained after collision with a neutron. These are labeled in Fig. 3.1a: 563 (^{76}Ge; 7.83% abundance), 596 (^{74}Ge; 36.73%), 834 (^{72}Ge; 27.31%), and 1039 keV (^{70}Ge; 20.37%). The PPD spectrum, plotted in Fig. 3.1b, yields an additional peak of this nature at 691 keV, which is attributed to decay of a 444-ns isomeric state in ^{72}Ge.

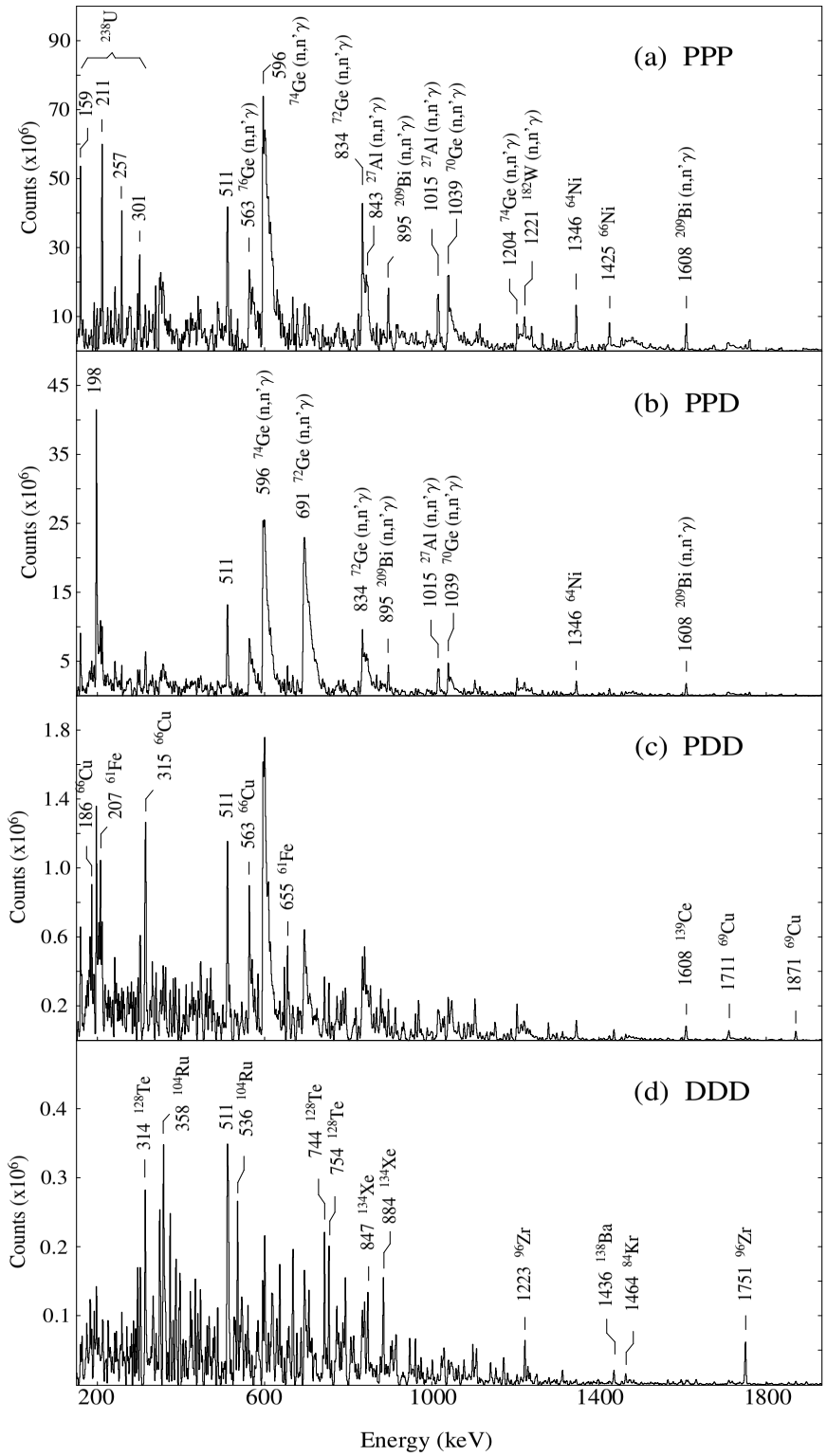

Figure 3.1: The total projection spectra for each coincidence cube. Representative peaks are labeled in each spectrum.

Neutron interactions with other elements of the detector apparatus besides the germanium crystals are also visible. For instance, peaks arising from the presence of ^{27}Al, ^{182}W, and ^{209}Bi are labeled in Fig 3.1a. These materials come from the aluminum casing that holds the germanium, the Hevimet absorbers, and the BGO Compton-suppressors, respectively. A detailed analysis of neutron-induced background radiation has been carried out in Ref. [70].

A significant contribution to the PPP data comes from γ-ray transitions in the beam and target materials. These arise from Coulomb excitation in the absence of a reaction. Also, the 1425-keV γ ray from the 2^+ state of ^{66}Ni is evident in this spectrum, which probably comes from two-nucleon transfer from the target. Lastly, the positron annihilation peak at 511 keV is present in all of the spectra.

In Figure 3.1c and d, where the total number of counts is relatively small, one can begin to see real reaction products. This is especially true for the PDD spectrum, where the selectivity of correlated prompt and delayed data is evident. Here, four specific cases of isomeric decay can be picked out: (1) ^{61}Fe, which has a half-life of 250 ns and is characterized by a cascade of 655 $\rightarrow$ 207 keV γ rays; (2) ^{66}Cu, with $t_{1/2}$ = 600 ns, and a cascade 563 $\rightarrow$ 315 $\rightarrow$ 89 $\rightarrow$ 186 keV; (3) ^{69}Cu, with $t_{1/2}$ = 360 ns, and a cascade 75 $\rightarrow$ 486 $\rightarrow$ 470 $\rightarrow$ 1711 keV; and (4) ^{139}Ce, with $t_{1/2}$ = 70 ns, and a cascade 270 $\rightarrow$ 1608 keV. This last example comes from fission of the target or target-like product, as do each of the transitions labeled in the DDD spectrum of Fig. 3.1d.

3.2 ^{58}Fe

Since the structure of stable ^{58}Fe has been the subject of a number of detailed and thorough studies, the presentation of ^{58}Fe data here exists primarily for illustrative and demonstrative purposes. The level schemes depicted in Figure 3.2a and b, provide the levels and γ rays that could be identified from PPP and DDD spectra, respectively, and the relative intensity of each transition, as determined from the current experiment, are represented by the widths of the transition arrows. Spin and parity assignments are adopted from the accumulated literature, as given in Ref. [71].

One of the important characteristics to note from these data, illustrated in the level schemes of Figure 3.2, as well as in the spectra of Figure 3.3, is the general pattern of excited states that can be identified from the reaction. For instance, the prompt data indicate a preference toward yrast and near-yrast states, whereas the

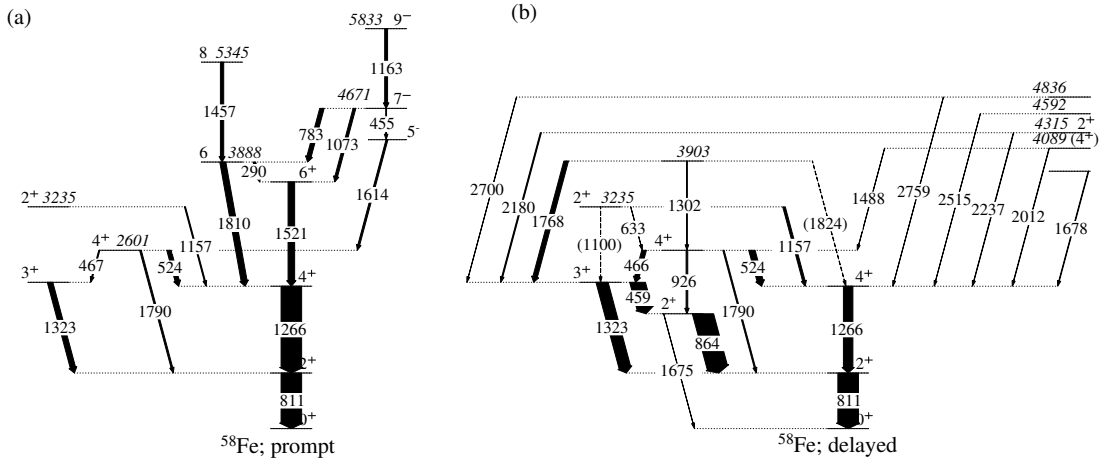

Figure 3.2: Partial level scheme for ^{58}Fe derived from (a) PPP and (b) DDD coincidence cubes.

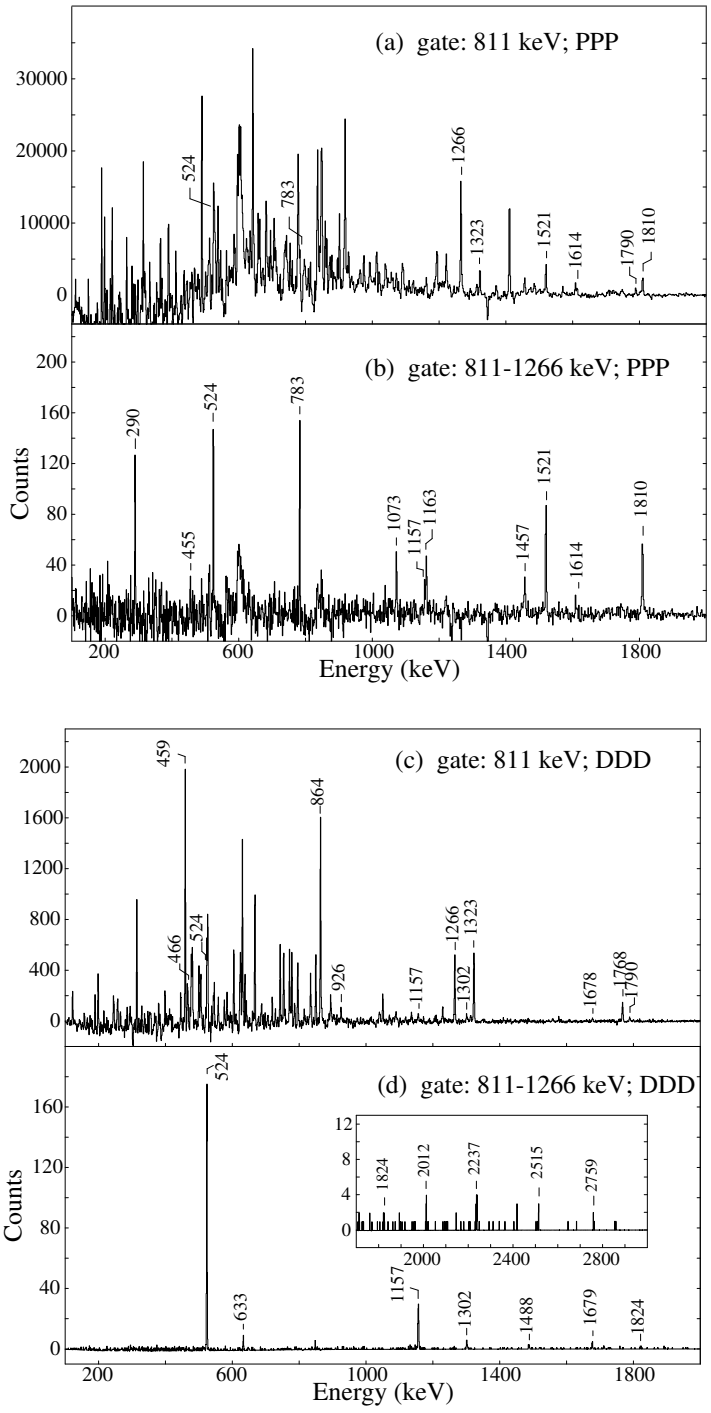

Figure 3.3: Representative spectra from coincidence gates on $2^+ \rightarrow 0^+$ and $4^+ \rightarrow 2^+$ transitions in ^{58}Fe in prompt and delayed cubes.

delayed data yield a completely different population of states which focuses instead on low-spin levels. The latter trend is simply a signatory that the off-beam data consist almost entirely of β-delayed γ rays, whereas the former reflects the large amount of energy and angular momentum that is exchanged during a deep-inelastic reaction.

Another interesting, albeit somewhat disconcerting, feature of the current dataset is the rather large discrepancy in the relative intensities and branching ratios of some transitions compared with previous β decay work [72]. For example, the γ ray branching ratio of the 2134-keV, 3^+ state has been purported to proceed roughly 75% via the 1323-keV transition, whereas in the current work a value just under 45% is deduced. Similarly, the 1675-keV, 2_2^+ state reportedly decays directly to the ground state with a 44% branch compared to the current dataset where nearly all of the decay appears to pass through the 2_1^+ state. Both of these cases can be easily attributed to the threefold coincidence requirement adopted in this experiment. For any direct population of the 3^+ state, the decay through a 1323-811 keV sequence would not be recorded owing to the multiplicity of this cascade. Nor would the 459-1675 keV sequence be recorded for the same reason.

An analysis of the angular correlation of γ-ray transitions in the prompt data did not produce adequate results owing to the high background present in 811- and 1266-keV coincidence gates. In contrast, the delayed data did present a good test case for such an analysis. Here, peaks fit from a single coincidence gate on the 811-keV, $2^+ \rightarrow 0^+$ transition yielded $a_2 = 0.11(9)$, $a_4 = 0.07(12)$ for the 1266-keV $4^+ \rightarrow 2^+$ transition, and negative a_2 coefficients for 459- and 1323-keV transitions,

Table 3.1: Levels observed in ^{58}Fe from the PPP data.

E_{level} (keV)	J^π	E_γ (keV)	I_γ
811	2^+	811.0(1)	100
2077	4^+	1266.2(1)	100
2134	3^+	1323.1(2)	26(4)
2601	4^+	466.9(2)	
		524.1(2)	21(3)
		1790.1(1)	8(1)
3235	2^+	1157.4(2)	5(2)
3598	6^+	1520.9(1)	32(4)
3888	6	289.6(2)	12(2)
		1810.5(2)	29(4)
4214	5^-	1614.3(4)	9(1)
4671	7^-	455.3(2)	4(2)
		783.1(1)	21(3)
		1072.6(3)	13(3)
5345	8	1457.1(2)	16(3)
5833	9^-	1162.6(4)	14(3)

consistent with the adopted J^π assignments for these states (see Table 3.2 for the correlation coefficients determined in this work).

As a final note, two transitions are depicted in Fig. 3.2b that are not included in the current nuclear database [71]. These transitions, at 1100 and 1824 keV, are included in the level scheme because (1) they are present in the very clean DDD coincidence gates, (2) coincidence gates involving these weak transitions return the expected spectrum consistent with their location in the level scheme, and (3) their energies imply levels which are already known to exist, and which are marked

Table 3.2: Levels observed in ^{58}Fe from the DDD data.

E_{level} (keV)	J^{π}	E_{γ} (keV)	I_{γ}	a_2	a_4
811	2^+	810.9(1)	100		
1675	2^+	864.2(1)	100	0.47(6)	0.09(8)
2077	4^+	1266.0(1)	46(2)	0.11(9)	0.07(12)
2134	3^+	459.3(1)	74(2)	-0.13(6)	0.09(8)
		1323.4(1)	57(2)	-0.49(3)	-0.07(5)
2601	4^+	466.4(1)	22(1)		
		524.1(2)	30(2)		
		925.8(1)	8(1)		
		1789.8(5)	6(1)		
3235	2^+	632.9(3)			
		1100.4(5)			
		1156.9(2)	12(3)		
3755		1677.9(5)	3(2)		
3903		1302.2(3)	4(3)		
		1768.3(2)	22(1)		
		(1824)			
4089	(4^+)	1488.4(1)	1(1)		
		2012.5(4)	2(1)		
4315	2^+	2179.7(5)	5(1)		
		2237.4(6)	2(1)		
4592		2515.0(3)	1(1)		
4836		2700.2	1(1)		
		2759.3(3)	< 3		

by other known transitions in the spectra. The scant evidence for an 1824-keV transition is provided in the form of a few counts in the inset of Fig. 3.3d, and evidence for the 1100-keV transition is not explicitly shown but can be seen in the 811-1323 keV coincidence gate. The latter transition is somewhat more intense than the former and, as such, the peak could be fit, although the relative intensity could not be reliably extracted.

3.3 ^{60}Fe

The nucleus ^{60}Fe has been extensively studied with a wide array of techniques, ranging from transfer reactions [73–75] to fusion-evaporation [73, 76] to β decay [77–79] and deep-inelastic reactions [80] (additional deep-inelastic work, carried out in parallel with the current project was recently reported in Ref. [81]).

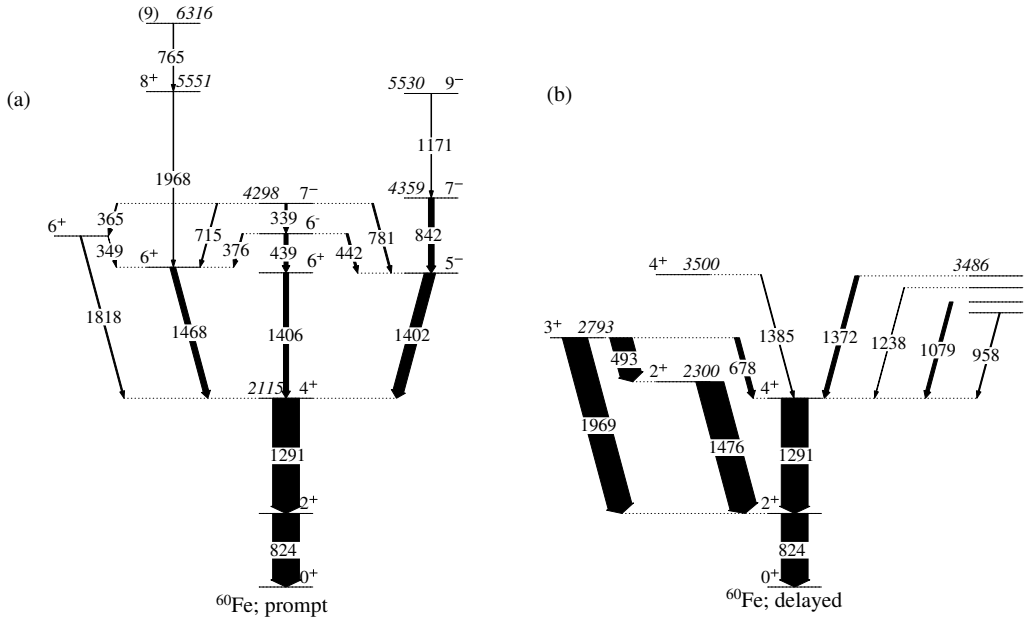

Figure 3.4: Partial level scheme for ^{60}Fe derived from (a) PPP and (b) DDD coincidence data.

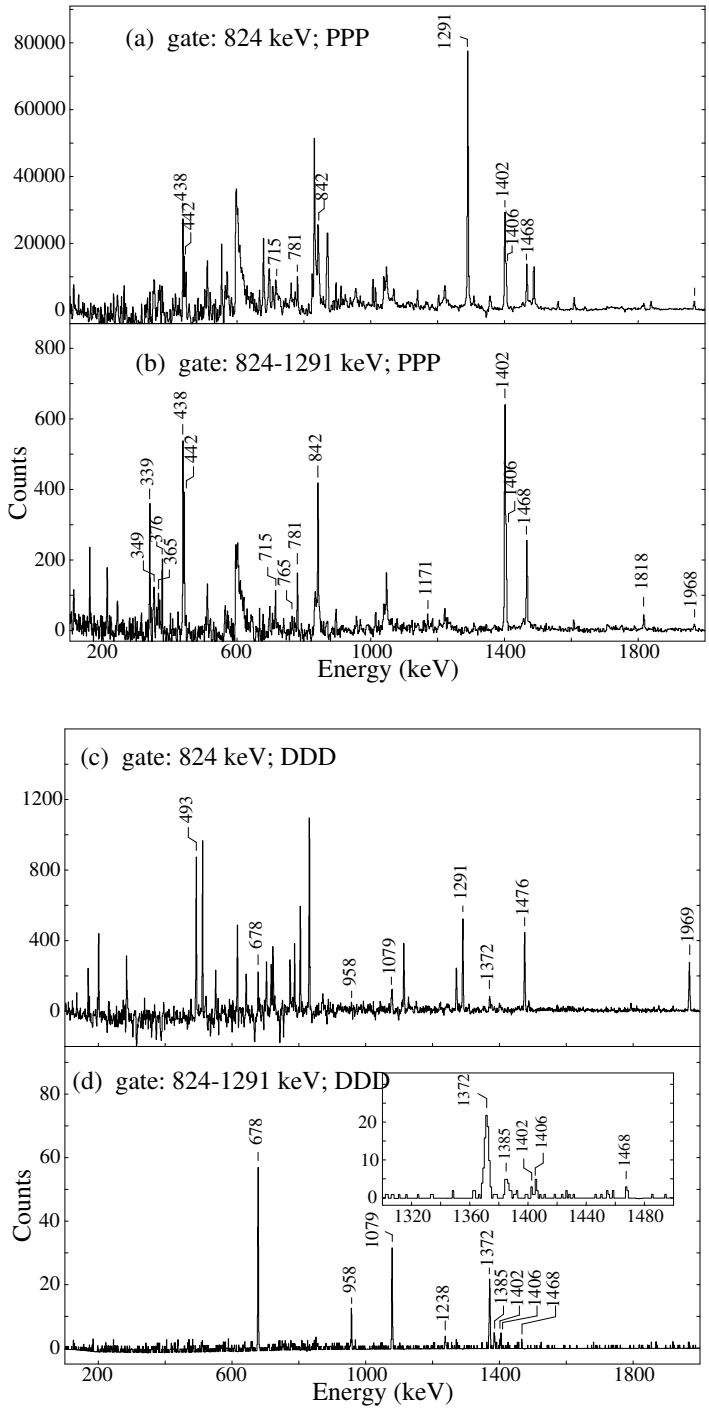

Figure 3.5: Representative spectra from coincidence gates on $2^+ \rightarrow 0^+$ and $4^+ \rightarrow 2^+$ transitions in ^{60}Fe in prompt and delayed cubes.

The current experiment differs only slightly from Ref. [80], where a 360 MeV ^{64}Ni beam was incident on a ^{208}Pb target, and Gammasphere, then at Lawrence Berkeley National Laboratory, consisted of 83 detector modules. Thus in principle, the current experiment, with more detectors, a more neutron-rich colliding system and a longer run time (5 days compared to 48 hours), should yield superior results. In fact, the results from the prompt data of this experiment, illustrated in Figure 3.4a, reveal several new transitions beyond what could be seen in that experiment. This is illustrated in Figure 3.5a and b, in which the spectra are presented from coincidence gates on 824- and 824-1291-keV γ-ray transitions, respectively. The single coincidence gate in Fig. 3.5a produces a complex assortment of small peaks below $\sim$850 keV, but some of the more intense transitions can nevertheless be identified in this range, including the 781-keV transition that was not reported in Ref. [80]. This is puzzling since this γ ray is quite prominent in the double-coincidence gate of Fig. 3.5b, with a relative intensity at least as much as a few of the transitions that were identified in that work (unfortunately, the spectra from Ref. [80] are not available for comparison). Additional new γ rays have been identified at 349, 365, 715, 765, 1170, and 1818 keV. These results are corroborated by an extensive analysis of high-spin states in this nucleus reported recently by Deacon *et al.* [76]. In that work, all of these transitions were reported and more, far exceeding what could be identified here. However, one important result arises from this work in that the distinction could be made between 1402- and 1406-keV transitions in the angular correlation analysis, whereas this doublet could not be easily separated in the Doppler-corrected data of Ref. [76]. The correlation coefficients determined in

this work, from a coincidence gate on the 1291-keV transition are a_2 = -0.07(3), a_4 = -0.02(4) and a_2 = 0.21(6), a_4 = 0.03(9) for 1402 and 1406 keV, implying dipole and quadrupole character, respectively. Thus, the spin assignments for the states at 3517 ($J = 5\hbar$) and 3521 ($J = 6\hbar$) keV proposed by Wilson *et al.* [80] are confirmed. However, the angular correlations measured here cannot distinguish the parity of the transition and hence this remains uncertain. Whereas Wilson *et al.* [80] proposed a positive parity for the state at 3517 keV (without an accompanying explanation), Deacon *et al.* [76] have proposed a negative parity based on (1) the absence of an analagous state in shell model calculations which employed the pf model space, and (2) the fact that the band was observed to extend up to $J = 17\hbar$, consistent with a proposed configuration $\nu g_{9/2}(f_{5/2}p_{3/2}p_{1/2})^5$.

The results from an analysis of delayed coincidence spectra is summarized in Fig. 3.4b. A coincidence gate on the 824-keV transition, illustrated in Figure 3.5c, yields several contaminant γ rays which belong to nuclei other than ^{60}Fe, in addition to a number of strong lines associated with this nucleus. The spectrum of Figure 3.5d shows the results of a double-coincidence gate on 824- and 1291-keV γ rays. Most prominent in this very clean spectrum is the known 678-keV line which deexcites the level at 2792 keV into the 4^+ state at 2115 keV. In addition to this, three more strong lines are observed at 958, 1079, and 1372 keV. As none of these appears in coincidence with one another, these γ rays are determined to independently feed the 4^+ state at 2115 keV. The γ ray at 958 keV was reported previously by Warburton *et al.* [73] from ^{58}Fe(t,$p\gamma$) reactions, and the 1079- and 1372-keV γ rays were previously identified by Runte *et al.* [78] following the β decay of ^{60}Mn but could not be placed

in the level scheme. Closer inspection shows additional lines at 1239, 1385, and some trace of the lines at 1402 and 1405 keV. Among these, only the 1239-keV line is unique to this experiment. The level implied by the 1385-keV γ ray was identified previously from (t,p) reaction data in Ref. [75], whereas the 1402- and 1405-keV γ rays are among the yrast transitions that could be easily distinguished in the prompt data, and were consequently identified in a previous deep-inelastic experiment [80]. In fact, the possibility that these two transitions are present as merely leak-through from the prompt data could not be ruled out, owing to the extremely low intensities associated with these peaks, but this is unlikely (for a further discussion on this matter see section 3.5).

Previously, the level at 2793 keV, which partially deexcites via the 1969-keV γ ray, was proposed to possess spin and parity $J^\pi = 3^+$ [77]. The basis for this assignment was that the logft value from decay of the parent ^{60}Mn implied an allowed transition, and the absence of this level in (t,p) reaction data may be an indication that it is of unnatural parity. Although recent findings [79] show that Norman *et al.* [77] assumed an incorrect spin for the β-decaying state in ^{60}Mn, this does not affect the basis for their assignment. Curiously, Wilson *et al.* [80] suggest a spin and parity of 4^+ for this level and, whereas they offer no evidence in support of this assignment, this is the value which has been accepted into the current nuclear database of Ref. [71]. However, a measurement of the angular correlation of the 1969-keV γ ray, determined from a coincidence gate on 824 keV, gives coefficients a_2 = -0.22(4), a_4 = -0.02(5), consistent with dipole character which confirms the assignment $J^\pi = 3^+$.

Table 3.3: Levels observed in ^{60}Fe from the PPP data.

E_{level} (keV)	J^{π}	E_{γ} (keV)	I_{γ}	a_2	a_4
824	2^+	823.9(1)	100	0.11(1)	0.04(2)
2115	4^+	1291.0(1)	100		
3517	$5^{(-)}$	1402.0(1)	41(3)	-0.07(3)	-0.02(4)
3521	6^+	1405.7(2)	19(2)	0.21(6)	0.03(9)
3583	6^+	1467.8(1)	21(2)	0.11(4)	0.02(6)
3933	6^+	349.1(6)	1(1)		
		1818.0(2)	5(2)	0.33(18)	0.02(26)
3959	(7^+)	376.4(2)	5(2)	0.23(11)	-0.05(15)
		438.7(2)	15(2)	0.14(5)	-0.09(7)
		442.3(2)	8(1)	0.15(8)	-0.07(12)
4298		339.1(2)	8(1)	-0.22(9)	-0.03(12)
		365.4(5)	4(1)		
		715.3(2)	4(1)		
		781.2(3)	6(1)	0.01(13)	-0.23(19)
4359		842.5(3)	21(2)		
5007		1047.9( )	13(1)		
5530		1171.0(2)	2(1)		
5551		1968.4(5)	2(1)		
6316		765.3(1)	2(1)		

Table 3.4: Levels observed in ^{60}Fe from the DDD data.

E_{level} (keV)	J^{π}	E_{γ} (keV)	I_{γ}	a_2	a_4
824	2^+	823.8(1)	100		
2115	4^+	1291.0(1)	100	0.17(7)	0.05(9)
2300	2^+	1476.1(1)	101(4)	-0.18(7)	0.40(10)
2793	3^+	493.0(1)	81(3)		
		678.3(2)	18(2)		
		1969.2(1)	91(5)	-0.22(4)	-0.02(5)
3073		957.7(3)	4(1)		
3194		1079.0(5)	13(2)		
3354		1238.5(7)	2(2)		
3486		1371.6(2)	16(3)		
3500		1385.4(4)	3(2)		

3.4 ^{61}Fe

The structure of ^{61}Fe was previously investigated using β-decay [78], fragmentation [82], and, to some extent, deep-inelastic [83] reactions. From these studies, a 239(5)-ns isomeric state has been established at 861 keV [82, 84]. This state has been determined to represent the $9/2^+$ level associated with the occupation of the $g_{9/2}$ neutron orbital by a single neutron [85]. Above this isomer, a γ ray at 789 keV has been reported, deduced from the prompt-delayed coincidence matrix obtained in a deep-inelastic reaction with ^{64}Ni and ^{130}Te [83]. In the present study, triple-coincidence data are used to establish several new transitions above this 239-ns isomer, starting from the previously known 207- and 655-keV γ rays associated with the isomeric decay [82]. Figure 3.7a presents the result of a double-gate set

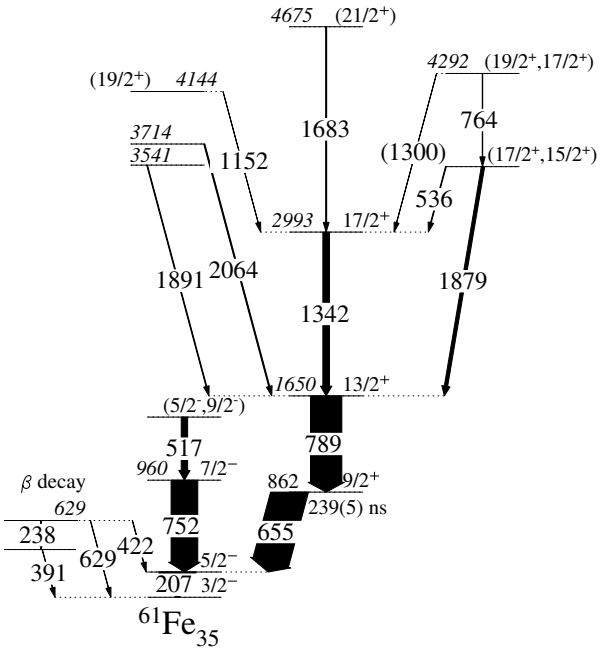

Figure 3.6: Partial level scheme for ^{61}Fe derived from correlated prompt and delayed coincidence cubes. Arrow width reflect the relative intensity of each peak and were not corrected for the presence of the isomer.

on these two transitions in the PPP coincidence cube. The 789-keV transition is clearly present in this spectrum together with a weak peak at 1342 keV. Note also two other weak transitions at 1040 and 1222 keV. Accompanying these is a similar weak (hardly visible in Figure 3.7a) γ ray at 842 keV. These most likely correspond to neutrons interacting with elements within the detectors, as discussed in section 3.1.

A similar double-gate on the 207-655 keV γ rays in the PDD cube, displayed in Fig. 3.7b, indicates a dramatic enhancement of all of the peaks that could be identified in the prompt spectrum, as well as the presence of several new transitions. Most prominent in this spectrum are the peaks at 1014, 1040, 1222, 1342, and 1879 keV, all of which are appreciably weaker than the very intense 789-keV γ ray. Of

these, three can be eliminated as candidates for γ-ray transitions in ^{61}Fe with a quick glance back at Fig. 3.1b, and the accompanying discussion, as the lines at 1014, 1040, and 1222 keV correspond to neutron-induced activity. A close inspection of Fig. 3.7b reveals five transitions that cannot be attributed to such reactions: 1184, 1309, 1342, 1683, and 1879 keV.

Figure 3.8 presents the coincidence spectrum resulting from the summation of double gates on the 207-789 keV and 655-789 keV γ rays. Again, γ rays from

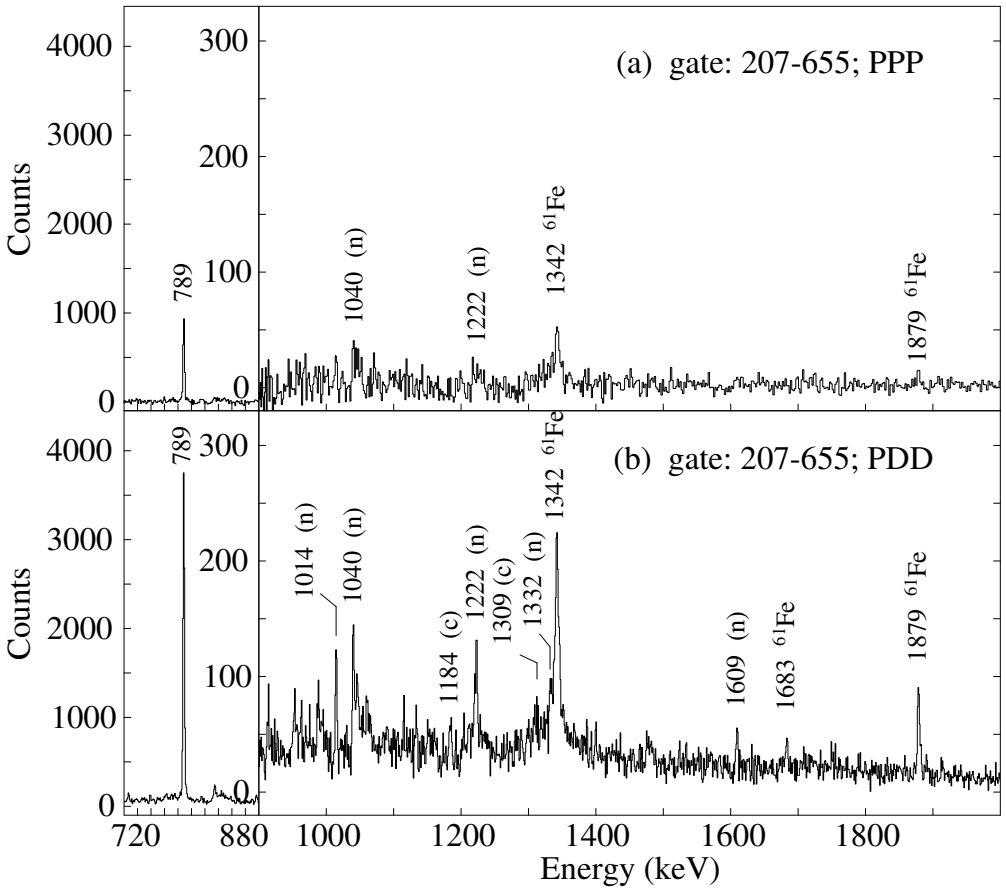

Figure 3.7: Gamma-ray spectra from the 207-655 keV coincidence gate in a) PPP and b) PDD cubes. Peaks marked with an n indicate γ rays arising from $(n, n'\gamma)$ reactions with elements in the detectors and auxiliary equipment, and c denotes unresolved contaminant transitions from a nucleus other than ^{61}Fe.

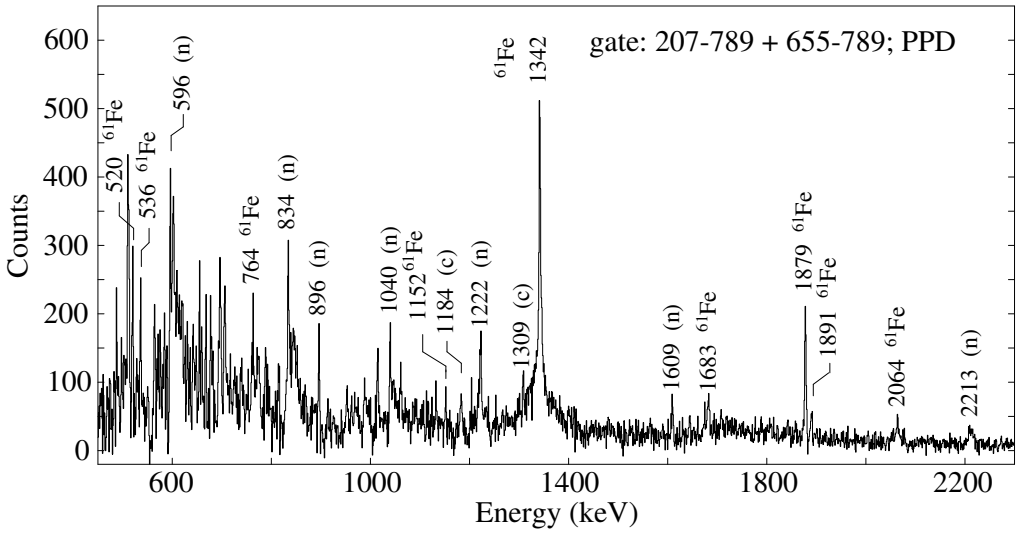

Figure 3.8: Spectrum produced from the sum of 207-789 and 655-789 keV coincidence gates in the PPD cube. In the spectrum, n denotes peaks that arise from $(n, n'\gamma)$ reactions with elements in the detectors and auxiliary equipment and c indicates peaks that are associated with unresolved contaminants from a nucleus other than ^{61}Fe.

neutron-induced reactions are widespread (this is primarily an effect of the location in energy of the gating transitions). Among the strong lines that could not be attributed to neutrons are: 520, 536, 764, 1152, 1184, 1309, 1342, 1683, 1879, 1891, and 2064 keV. Further inspection indicated that the 1342-keV peak is in coincidence with 536-, 1152-, and 1683-keV γ rays. Close scrutiny reveals a possible peak at 1300 keV in the 207-1342 keV double gate, but this transition does not appear above background in the 655-1342 keV double gate. Still, all of the gates involving this transition appear to produce consistent results, and the level implied at 4293 keV is supported by a coincidence relationship between the 1879- and 764-keV γ rays. Thus, each of the lines above is placed in the level scheme of Figure 3.6, although the assignment of the transition at 1300 keV remains tentative.

The analysis of the γ ray at 1309 keV indicates that it is in coincidence with the 520-keV transition. However, additional coincidence relationships with γ rays at 192, 333, and 369 keV indicate that this cascade belongs to a different nucleus. This leaves the 1184-, 1891-, and 2064-keV lines as the remaining candidate transitions. The 1184-keV γ ray returns 223- and 488-keV lines in coincidence and is, similarly, assumed to belong to a different nucleus. Analyses of the γ rays at 1891 and 2064 keV do not indicate any further coincidence relationships beyond those already established with 207-, 655-, and 789-keV transitions. Thus, these lines are included in the level scheme of Figure 3.6 directly populating the $13/2^+$ state.

In an independent investigation conducted in parallel with this work, the same reaction was studied, but with a thin target and recoil mass gating [81, 86]. An additional γ ray at 752 keV was reported in that work, which is found to directly populate the level at 207 keV. Data from the prompt cube in the present experiment clearly support this observation, and an additional transition at 517 keV is also observed to feed this new level.

An angular correlation analysis was performed for the strongest lines that could be identified in the data. As a proof-of-principle, the 655-207 keV sequence, which is known to be of *M2-M1* character, was analyzed. The resulting a_2 and a_4 angular correlation coefficients are $-0.03(4)$ and $0.07(5)$, respectively, supporting a quadrupole-dipole character in agreement with the literature. In spite of the fact that the 789-keV transition lies above the isomer, its intensity allows for a determination of its angular correlation, which is determined from a gate on the 655-keV γ ray to possess quadrupole character ($a_2 = 0.18(4), a_4 = 0.05(6)$). Similarly,

an analysis of the 1342-keV transition supports quadrupole character as well ($a_2 = 0.12(11), a_4 = 0.00(16)$, from a gate on the 789-keV γ ray), whereas the 752-207 keV correlation indicates a dipole-dipole cascade ($a_2 = 0.26(4), a_4 = 0.07(6)$).

On the basis of the angular correlation fits described above, the level at 1650 keV is determined to have spin and parity $13/2^+$, consistent with previous suggestions [83]. The most intense transition above the level at 1650 keV is the 1342-keV line of quadrupole character which most likely represents the next excitation of this sequence. Thus, a $17/2^+$ spin and parity are adopted for the state at 2993 keV. Similarly, the level at 4675 keV is tentatively assigned $21/2^+$. From feeding patterns, the sequence of levels at 3529 and 4293 keV could have $J^\pi = 17/2^+$ and $19/2^+$, respectively. This assignment also appears to be supported by the shell model calculations discussed below, but alternate respective assignments of $15/2^+$ and $17/2^+$ cannot be rigorously ruled out.

The level at 960 keV implied by the 752-keV γ ray is assigned a spin of 7/2 on the basis of its dipole character determined from angular correlations. A negative parity is assigned, primarily from systematics.

In addition to the levels described above, Fig. 3.6 shows two additional states at 391 and 629 keV that were previously identified from β decay [78]. Transitions associated with the de-excitation of these levels were not observed in this experiment, most likely due to the low multiplicity of these events. The γ rays, level energies, and proposed spins and parities that were established from this measurement are summarized in Table 3.5.

Table 3.5: Levels identified from the present experiment for ^{61}Fe. Relative intensities have not been corrected for the presence of an isomer.

E_{level} (keV)	J^π	E_γ (keV)	I_γ (rel.)
207.0	$5/2^-$	207.0(1)	100.0
861.8	$9/2^+$	654.8(1)	100.0
959.5	$7/2^-$	752.5(2)	72.9(105)
1476.6	$(5/2^-, 9/2^-)$	517.1(2)	17.5(29)
1650.3	$13/2^+$	788.5(1)	85.6(107)
2992.6	$17/2^+$	1342.3(3)	18.0(24)
3528.9	$(17/2^+, 15/2^+)$	1878.6(4)	9.2(13)
		536.1(3)	2.0(3)
3541.4		1891.1(6)	2.1(5)
3714.4		2064.1(6)	2.9(6)
4144.5	$(19/2^+)$	1151.9(2)	0.5(1)
4292.5	$(19/2^+, 17/2^+)$	763.6(2)	1.1(2)
		(1300)	<0.5
4675.3	$(21/2^+)$	1682.7(3)	2.7(6)

3.5 ^{62}Fe

Some information regarding the β decay of ^{62}Mn was previously reported by Runte *et al.* [87], which contributed to the establishment of the 2_1^+ and 4_1^+ states in ^{62}Fe. The level scheme was extended to medium spin from two deep-inelastic experiments [65, 80], but these reports contain some ambiguity in their spin assignments above J=4. In this work, the proposed assignments of Ref. [65] are supported with angular correlation data, as presented in the level scheme of Figure 3.9a. In particular, the assignment of dipole character is adopted for the 839-keV γ ray, and

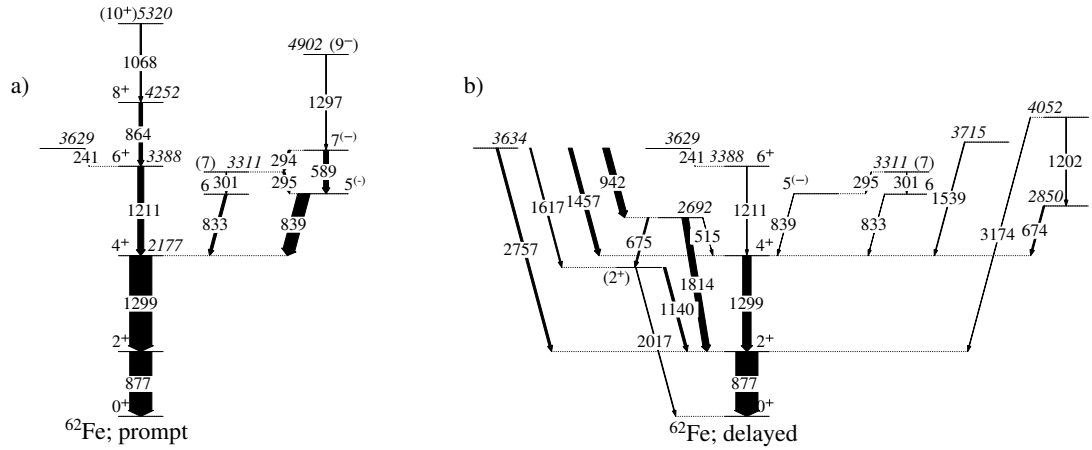

Figure 3.9: Partial level scheme for ^{62}Fe derived from (a) PPP and (b) DDD coincidence cubes.

quadrupole character is supported for the 833-, 1211-, 589- and 864-keV transitions (for a complete summary of the correlation coefficients, relative intensities, and γ-ray energies, see to Table 3.8).

The spectrum of Figure 3.10a, produced from a coincidence gate on the 877-keV γ ray in the prompt data, yields a relatively clean spectrum with intense peaks associated with γ-ray transitions in ^{62}Fe. A double-coincidence gate on 877- and 1299-keV transitions (Fig. 3.10b) gives rise to an even cleaner spectrum, and close inspection reveals a weak peak at 1297 keV. This γ ray, although weak, probably eluded previous investigators since it has an energy similar to the established $4^+ \rightarrow 2^+$ transition. From its coincidence relationships this line is placed above the proposed 7^- level at 3604 keV, making it a strong candidate for the 9^- state.

A coincidence gate on the 877-keV transition in the delayed cube, presented in Figure 3.10c, yields several very intense lines associated with the fission product ^{128}Te, which unfortunately has a γ-ray transition with an energy 878 keV. In spite

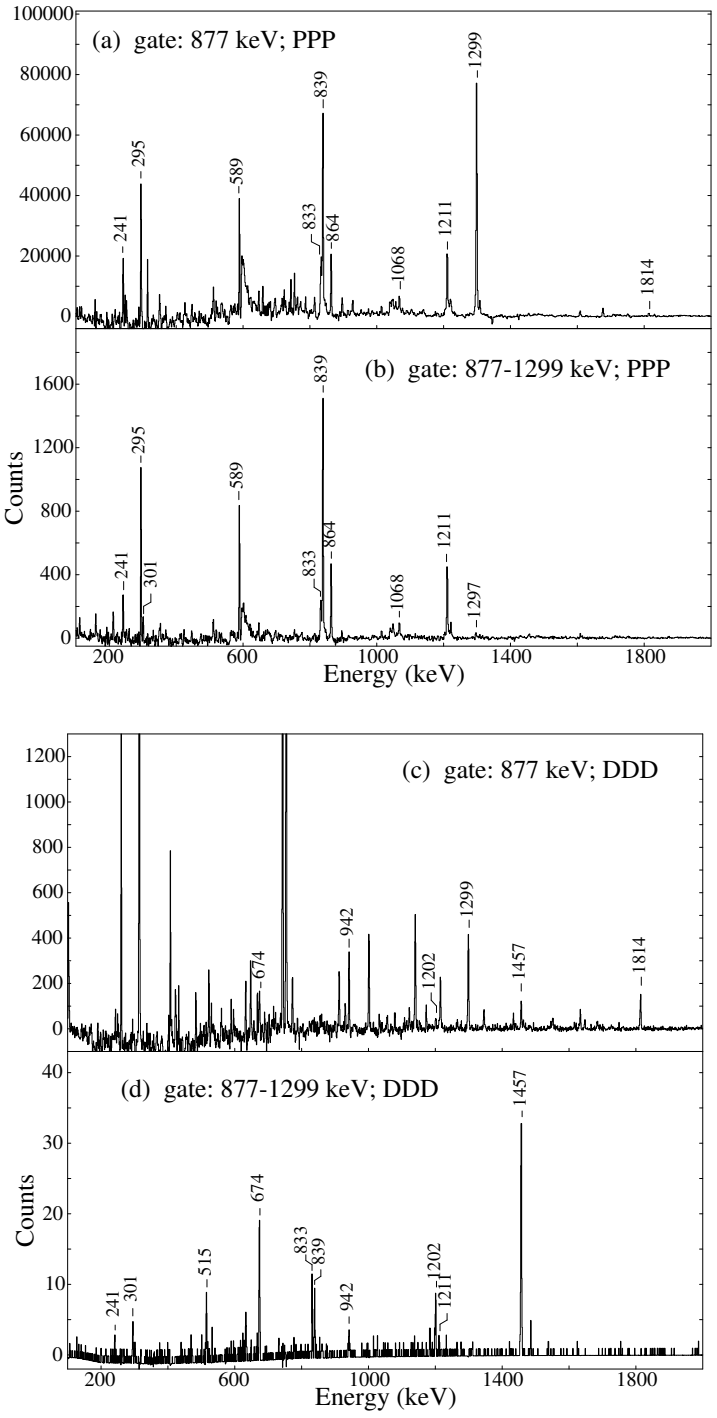

Figure 3.10: Representative spectra from coincidence gates on $2^+ \rightarrow 0^+$ and $4^+ \rightarrow 2^+$ transitions in ^{62}Fe in prompt and delayed cubes.

of this, many of the γ rays reported by Runte *et al.* [87], from the β decay of ^{62}Mn, can be identified in this spectrum. However, the contamination vanishes with the implementation of a double-coincidence gate on 877- and 1299-keV γ rays, as depicted in Figure 3.10d, and the resulting spectrum turns out to reveal a number of intriguing features.

The presence of some peaks that were observed in the prompt cube, identified in Refs. [65] and [80], but not in the previous β-decay measurement by Runte *et al.* [87], gave rise to the suspicion of leak-through from the prompt γ-ray flash that occurs during the beam burst. Recall that the presence of two weak lines at 1402 and 1406 keV in the delayed spectrum for ^{60}Fe sparked a similar concern. To test this hypothesis, a new coincidence cube was constructed in which the requirement for delayed events was re-defined so as to restrict the possibility for such contamination; namely, the minimum time with respect to the prompt beam burst was increased in the new cube. In the case of leak-through, any prompt lines leaking into the delayed data would be expected to disappear or substantially reduce in intensity compared to the γ rays that are known to arise from β decay. The subsequent analysis did not indicate the presence of leak-through, as each peak in the spectrum maintained a constant intensity relative to the 1457-keV peak which is known to be populated in β decay. A second explanation for the presence of these peaks could be the existence of an isomeric state in ^{62}Fe. If the isomer had a long enough lifetime then it would elude identification via the method described above. In this case, a series of gates in the PPD or PDD cubes would likely reveal correlated prompt and delayed transitions, which was not the case here (although this method is dependent on the

lifetime of the isomer). Last, the lines could simply arise from weak population via β decay that was below the detection limit of the experiment reported by Runte *et al.* [87]. Such a case would probably necessitate the existence of a β-decaying isomer in ^{62}Mn in order to explain the direct population of high-spin states and, indeed, Gaudefroy *et al.* [88] recently proposed the presence of a β-decaying isomer in that nucleus.

Another unexpected result arising from the spectrum of Fig. 3.10d is the presence of a small 942-keV peak. Prior to this work the 942-keV γ ray was proposed to deexcite a level at 1820 keV which is, itself, fed directly by an 1814-keV transition from the level at 3634 keV [87]. In this configuration, the 942-keV transition should not present a coincidence relationship with the 1299-keV γ ray since it runs parallel to this line in the level scheme. One possible explanation for this ambiguity could be the presence of a doublet at 942 keV. However, the centroid energies determined by fitting the peaks in different coincidence gates indicated identical energies within experimental uncertainty, which is an unlikely but not impossible scenario. It is important to note, as well, that in both experiments, the relative intensity of 942- and 1814-keV γ rays is identical, making the ordering of these two coincident transitions somewhat ambiguous. If, instead, the 942-keV transition decays from the 3634-keV state, a new level might be proposed at 2692 keV, which decays to the 2^+ state via the 1814-keV transition. This interpretation is supported with another new γ-ray transition present in Fig. 3.10d, at 515 keV, since this coincidence would, similarly, imply a new level at 2692 keV. Further support is provided in Figure 3.11 with a double-coincidence gate on 877- and 942-keV transitions, which reveals a

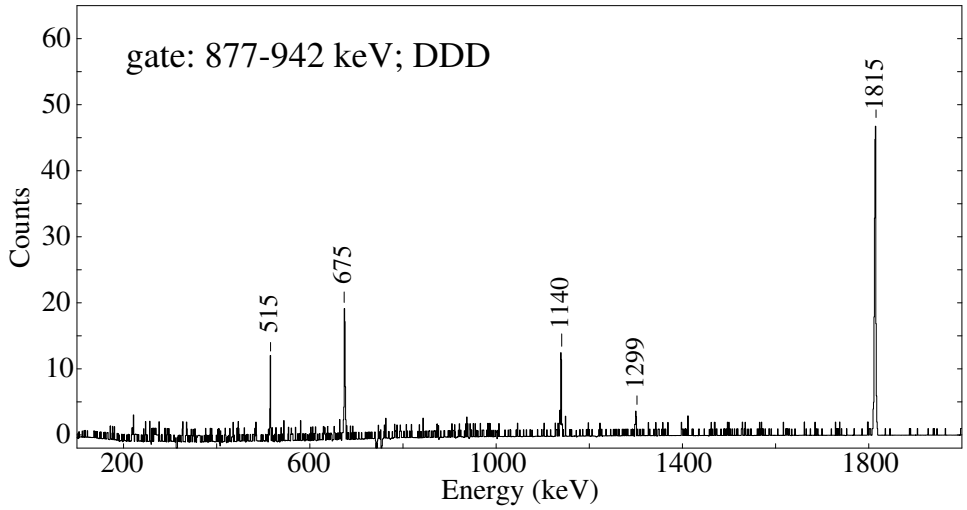

Figure 3.11: Double-coincidence gate on 877- and 942-keV γ rays in the DDD cube.

coincidence with 675 and 1140 keV, so that a cascade through the known level at 2017 keV is established.

By focusing attention once again on the spectrum of Figure 3.10d, it is clear that a pronounced 674-keV transition is present here. Note the 1-keV difference in the centroid energy of this γ ray from that which was present in the 877-942-keV double gate (Fig. 3.11). This is rather significant, and an additional coincidence with the γ ray at 1202 keV implies a new level at 4052 keV. A weak transition at 1539 keV may also be present in Fig. 3.10d and two more γ rays are present at 1184 and 1487 keV.

To complement this work, the results are compared to the unpublished results of an experiment carried out at ISOLDE/CERN. That experiment previously gave rise to Ref. [50], in which the data for β decay of ^{64,66}Mn were reported. For details on how the analysis of the data reported here was carried out, see Appendix B.

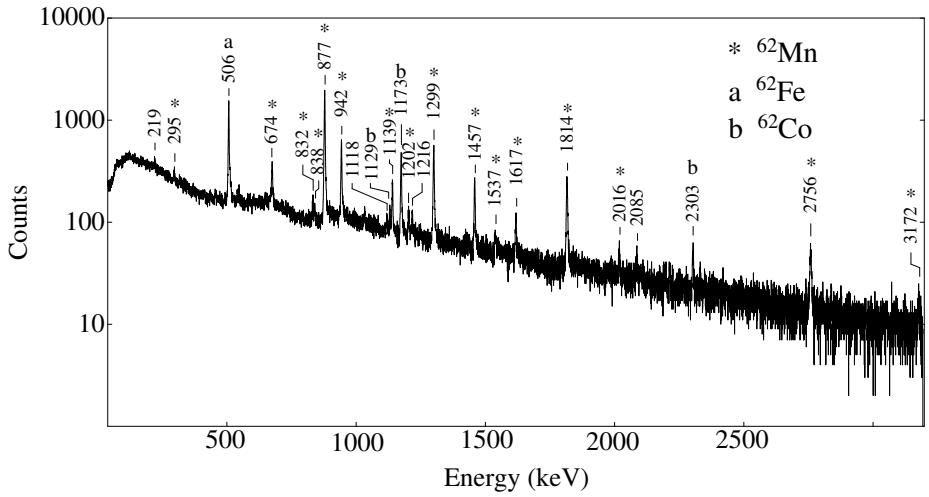

Figure 3.12: Decay spectrum for ^{62}Mn to levels in ^{62}Fe.

The spectrum of Figure 3.12 presents a rather thorough picture of the γ-ray transitions populated in the β decay of ^{62}Mn to levels in ^{62}Fe. Most of the levels reported above can be identified in this spectrum in addition to a few that could not due to low multiplicity cascades. For example, the two new levels at 2850 and 4052 keV, implied by 674- and 1202-keV coincident γ rays, are supported by the presence of a direct transition to the 2_1^+ state via a 3172-keV transition. A similar line extends from the 3634-keV level directly to the 2_1^+ state via a 2756-keV γ ray. The 2017-keV γ ray reported by Runte *et al.* [87] but missing from the triple coincidence data is also seen in this spectrum. Among the peaks that could not be identified in Fig. 3.12 are 515, 301, 1211, and 241 keV, each of which gave a relative intensity ≤ 1 in the analysis of triple-coincidence data. Additionally, the doublet at $\sim$675 keV could not be distinguished in this spectrum.

In their report, Runte *et al.* [87] proposed that ^{62}Mn has a ground-state spin and parity $J^\pi = 3^+$, since they observed allowed β transitions to 2^+ and 4^+ states.

However, this interpretation has come into question in a more recent report [88] in which the 1^+ state of ^{62}Mn was selectively populated through β decay of ^{62}Cr. Those authors also report a γ ray at 815 keV, which they attribute to the β decay of this apparently isomeric state (a γ ray which was not seen in this work). This presents somewhat of a conundrum since, even with a small energy difference, it is difficult to reconcile a β-decaying isomer in which the isomeric path exhibits a $\Delta J = 2$ (*ie:* a 100-keV, *E2* transition has a $\sim$5 μs mean lifetime based on the Weisskopf estimate, contrasted to tens of ms for the β-decay lifetime). A similar scenario was recently presented for the decay of ^{60}Mn, where Liddick *et al.* [79] populated ^{60}Mn$^{gs}(1^+)$ via β decay of ^{60}Cr$^{gs}(0^+)$. In that work, the authors argued that the ground state must possess $J^\pi = 1^+$ and the isomer therefore $J^\pi = 4^+$, since the spin change had been measured previously. It is therefore not unreasonable to assume a similar situation in ^{62}Mn, where the β-decaying isomer is 4^+ and the ground state is 1^+, or vice versa. Since neither of the experiments described here nor the report of Runte *et al.* [87] gave any indication of an 815-keV transition, the most likely scenario appears to favor a 4^+ isomer and 1^+ ground state. Then, the heavy population of the state at 3634 keV from β decay might imply $J^\pi = 4^+$, as opposed to the 2^+ assignment of Runte *et al.* which was based on the observed decay to the 4^+ state and to the 1820-keV state that was eliminated above. This raises questions, then, about direct feeding of the 2_1^+ state, purported by Runte *et al.* to be 42%, which is not consistent with the proposed 4^+ assignment of ^{62}Mn^m. However, a close inspection of the data from this work paints a very different picture, in which $\sim$10% direct feeding is observed (and this is close to the margin of error for this value).

More concerns are raised with the presence of weak population of medium-spin states in both datasets reported here. The presence of several of these transitions in the ISOLDE data indicate a population via β decay and not through the decay of a high-spin isomer in ^{62}Fe. Based on intensity balances, it appears that direct feeding populates medium-spin levels at 3629, 3311, and possibly 3009 keV. Unfortunately, the spins of the two former states have not been unambiguously determined. The 3311-keV state is tentatively assigned $J = 7$, and the level at 3009 keV, with $J = 6$, may or may not experience direct feeding. Because of these uncertainties, little can be concluded in regard to how these levels are populated in the β decay of ^{62}Mn.

Table 3.6: Levels observed in ^{62}Fe from the PPP data.

E_{level} (keV)	J^π	E_γ (keV)	I_γ	a_2	a_4
877	2^+	877.3(1)		0.12(1)	0.03(2)
2177	4^+	1299.2(1)	100		
3010	6	833.0(2)	13(2)	0.18(10)	0.00(15)
3016	$5^{(-)}$	839.2(2)	58(3)	-0.07(2)	0.05(3)
3311	(7)	294.2(6)	[1]		
		301.2(2)	3(1)		
3388	6^+	1211.3(1)	27(2)	0.12(4)	0.01(6)
3605	$7^{(-)}$	295.0(6)	[1]		
		589.2(1)	22(2)	0.14(4)	0.05(6)
3629		241.1(2)	6(1)		
4252	8^+	863.9(1)	16(2)	0.14(5)	0.07(8)
5320	(10^+)	1067.8(3)	6(2)		

[1] The relative intensity of the 294/295 keV doublet is 19(1). There is no reliable way to extract the individual intensities with the current data set.

Table 3.7: Levels observed in ^{62}Fe from the DDD data.

E_{level} (keV)	J^π	E_γ (keV)	I_γ (DI; β)		a_2	a_4
877	2^+	877.3(2)	-	100(2)		
2016	(2^+)	1139.8(4)	37(4)[1]	11(1)		
		2016.1(3)	-	3(1)		
2176	4^+	1299.2(2)	40	38(2)	0.06(7)	0.10(10)
2691		515.2(2)	1(1)	-		
		674.9(2)	3(1)	15(1)		
		1814.5(2)	22(5)	29(2)	-0.38(9)	-0.14(12)
2850		673.7(3)	2(1)	-		
3009	6^+	831.6(3)	1(1)	3(1)		
3015	$5^{(-)}$	838.0(9)	1(1)	2(1)		
3309	(7^+)	295.2(2)	1(1)	2(1)		
		301.5(2)	<1	-		
3387	6^+	1211.3(4)	<1	-		
3634		942.0(2)	19(3)	29(2)	0.23(7)	0.00(11)
		1457.5(2)	12(4)	17(1)		
		1617.0(2)	3(1)	6(1)		
		2755.8(6)	-	10(1)		
3628		241.0(2)	<1			
3713		1538.8(15)	<1	3(1)		
4052		1201.5(4)	2(1)	3(1)		
		3172.3(9)	-	2(1)		

[1] Some artificial enhancement of this intensity is expected from overlap with ^{128}Te γ rays.

3.6 ^{63}Fe

The structure of ^{63}Fe has been rather elusive as far as spectroscopic studies go. Several authors have reported a 356-keV γ ray populated in the β decay of ^{63}Mn [81, 89–92] and Gaudefroy [91] has proposed a decay scheme containing proposed levels in ^{63}Fe, but little is known beyond this. In the recent work of Lunardi *et al.* [81], two additional γ rays are reported in addition to this one at 819 and 1404 keV. In an attempt to establish coincidence relationships between these transitions, and to possibly identify new γ rays, various combinations of double-coincidence gates were attempted in each of the four cubes, as depicted in Figure 3.13. No coincidence relationship could be established for these transitions in any of the cubes.

3.7 ^{64}Fe

Excited states in ^{64}Fe, prior to this work, had been studied only through the β decay of ^{64}Mn and, as such, only the 746-keV, $2^+ \rightarrow 0^+$ transition had been published, first by Hannawald *et al.* [50], and later confirmed by Sorlin *et al.* [89] and Matea [90]. Several transitions associated with this β decay have been reported in the PhD. thesis of M. Hannawald [93], in which a tentative decay scheme was proposed, and some of those lines were identified, as well, in the PhD. thesis of L. Gaudefroy [91]. Since this work was carried out [94], there has been further work on the Fe isotopes in the form of a thin-target deep-inelastic reaction experiment reported by Lunardi *et al.* [81], which has been alluded to in previous sections. That

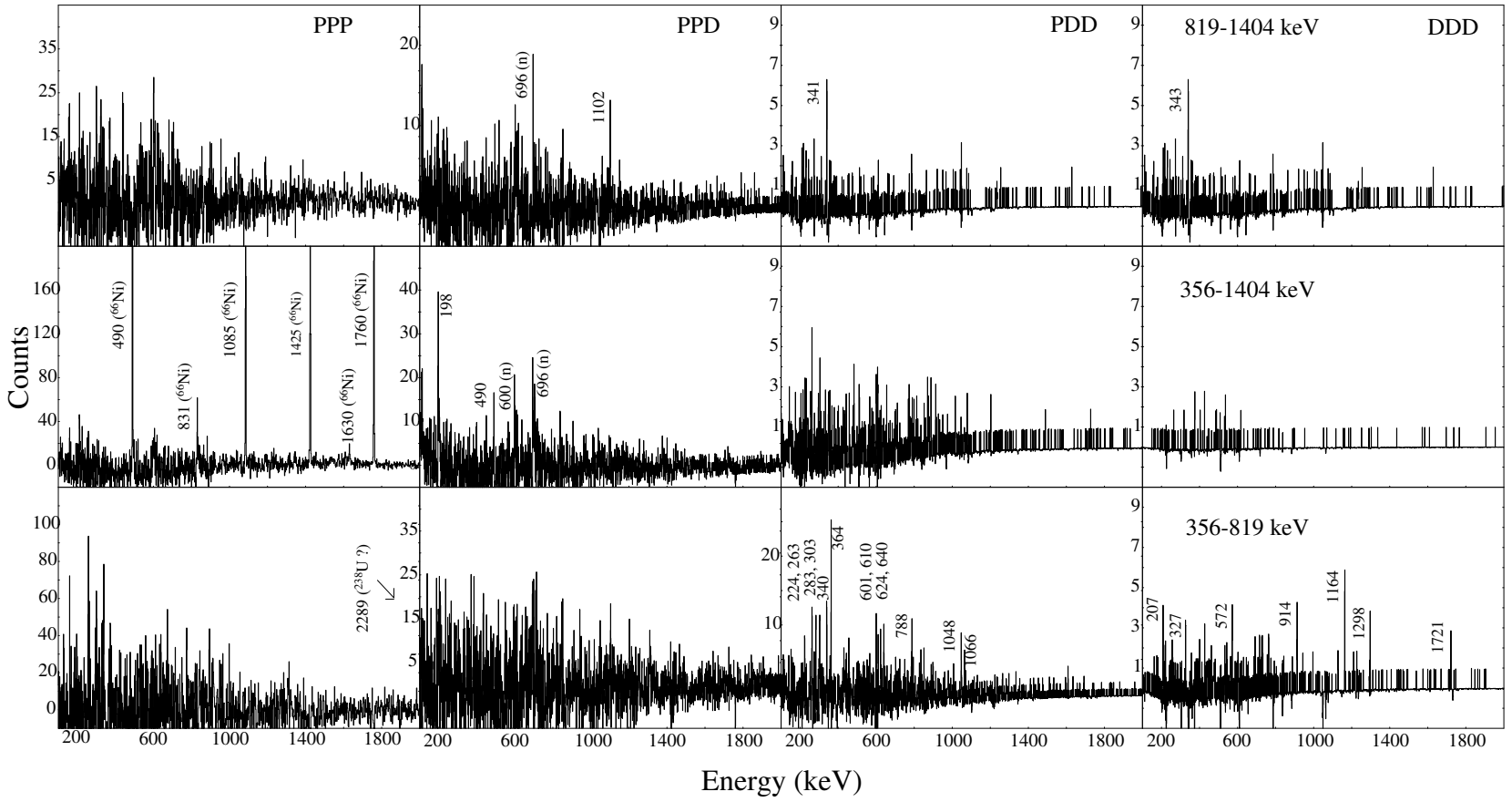

Figure 3.13: A series of coincidence gates on three γ rays in ^{63}Fe reported in Ref. [81]. A coincidence relationship could not be established from these data.

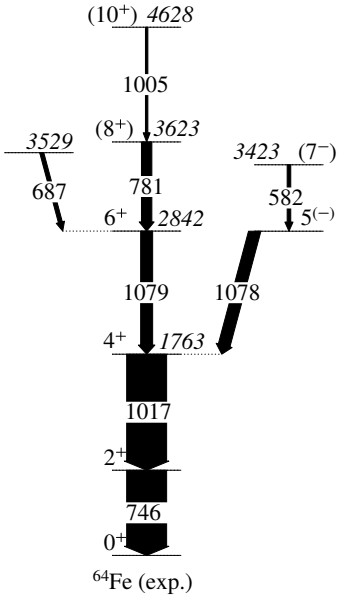

Figure 3.14: Partial level scheme for ^{64}Fe derived from the PPP coincidence cube.

work confirms most of the new γ-ray transitions identified here which are presented in Figure 3.14 and will be described below.

As has been reiterated several times in previous sections, the difference in levels populated directly during the deep-inelastic process compared with those populated in β decay, cast doubt on whether any transitions beyond the established 746-keV, $2^+ \rightarrow 0^+$ line would be easily identified in the prompt data. Thus, the starting point of the search for new prompt γ rays in ^{64}Fe was a single coincidence gate on the 746-keV γ ray, presented in Figure 3.15a. In this spectrum, four distinct lines rise above a rather complex background typical of such a simple coincidence requirement. Upon further investigation, two of these γ rays could be easily associated with known transitions in ^{69}Ga, where a 746-keV γ ray is known to be present, in coincidence with 914- and 635-keV transitions. The two remaining peaks could not be placed in any other known γ cascade and were, therefore, assumed to be candidates for higher-

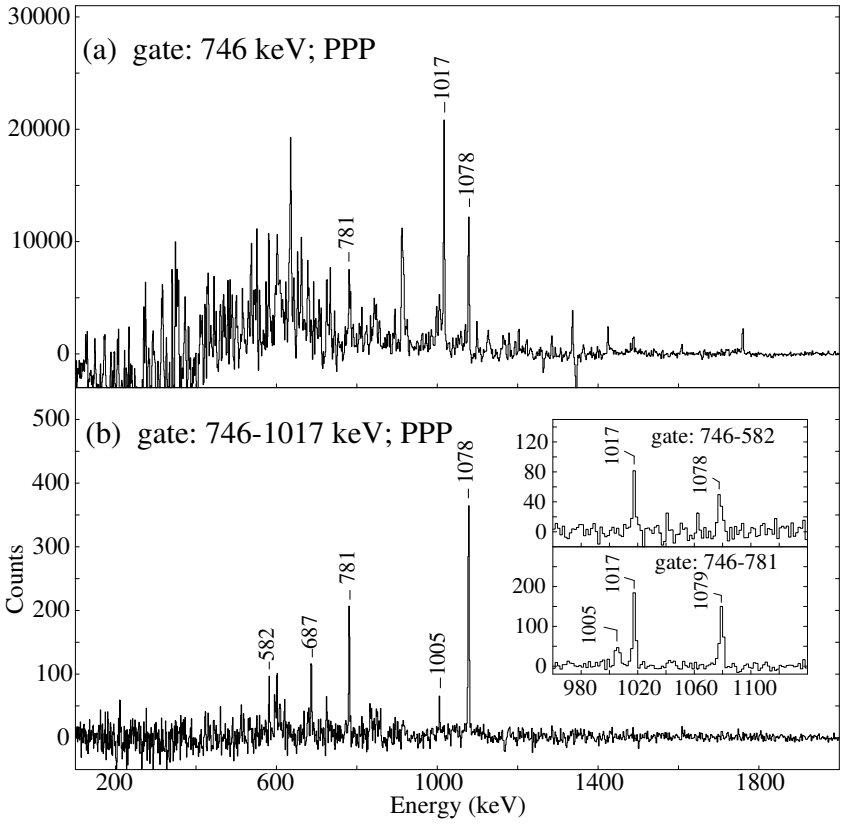

Figure 3.15: Representative spectra from coincidence gates on $2^+ \rightarrow 0^+$ and $4^+ \rightarrow 2^+$ transitions in ^{64}Fe in prompt cube. The insets illustrate a systematic shift in the centroid position of the 1078-keV peak.

lying transitions in ^{64}Fe. In fact, the peak at 1017 keV could be retrospectively identified in a spectrum measured at ISOLDE following the β decay of ^{64}Mn [95]. Furthermore, a double-coincidence gate placed on the 746- and 1017-keV transitions in the data from a previous experiment with ^{48}Ca and ^{208}Pb produced weak, but discernable, lines corresponding to yrast transitions in the Os isotopes, as shown in Figure 3.16. This is a clear indication that the γ rays belong to Fe because, for this particular colliding system, Fe and Os are produced simultaneously as reaction partners. Therefore, transitions in the Fe and Os isotopes will appear in coincidence with one another. The assignment to ^{64}Fe then follows because the 746-keV, 2^+

$\rightarrow 0^+$ transition has been measured previously. A similar cross-correlation analysis could not be performed with the current data because the target-like nuclei are expected to mostly undergo prompt fission.

The spectrum from a double-coincidence gate on the 746- and 1017-keV transitions is presented in Figure 3.15b. New lines are observed at 781, 1005, and 1078 keV. These are found to be in mutual coincidence with each other and with the 746- and 1017-keV γ rays. Additional lines are observed at 582 and 687 keV that are in mutual coincidence with the 746-, 1017- and 1078-keV lines, but not with each other. A noticeable energy broadening of the 1078-keV γ line gave indication for a possible doublet consisting of similar intensity components with an energy difference in the range of 1 keV. Indeed, the double-coincidence gates placed on the 746-keV line and correspondingly lower- and higher-energy parts of the 1078-keV peak resulted in clearly different spectra. Careful examination confirmed the presence of

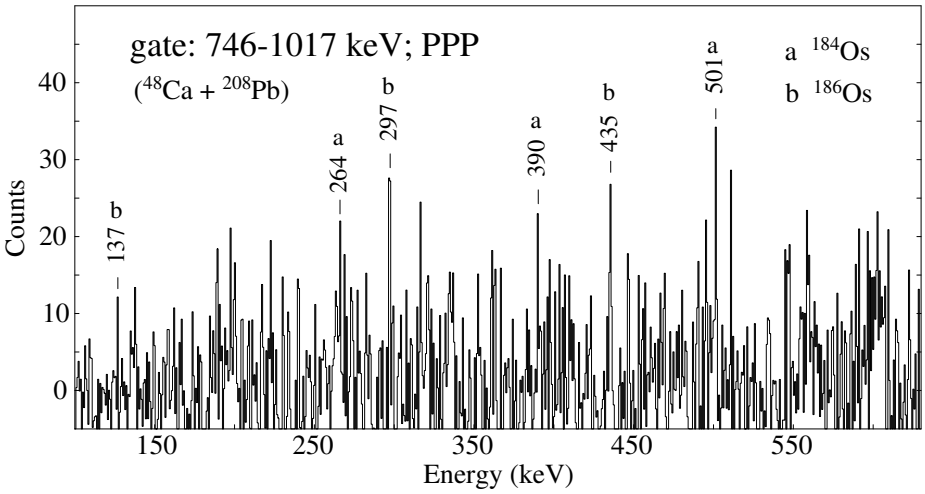

Figure 3.16: Coincidence gate on 746- and 1017-keV γ rays in the prompt data from the reaction ^{48}Ca + ^{208}Pb. The presence of γ rays from ^{184,186}Os confirms that the 1017-keV γ ray belongs to an isotope of Fe, since Os is the complement of Fe in this reaction.

two closely spaced transitions with the lower-energy component being in coincidence with the 582-keV line and the higher-energy component forming an yrast cascade with the upper 781- and 1005-keV transitions. This is illustrated in the inset of Figure 3.15b, where selected portions of the 582-746 (upper panel) and 781-746 (lower panel) double-gated spectra are given. Besides the 1005-keV line appearing only in the lower spectrum, one observes a shift in the position of the 1078-keV peak. The centroids obtained from these spectra determined the 1077.8- and 1078.9-keV energies for the corresponding components of the doublet. The proposed level scheme obtained from this data is provided in Figure 3.14.

An angular correlation analysis performed on these data indicated quadrupole character for the 1017-keV γ ray, confirming it to be the $4^+ \rightarrow 2^+$ transition, and it is noted that the two members of the 1077.8/1078.9 doublet exhibit a stark contrast in their respective angular correlations, depending on which γ ray is measured in conjunction with the 746- or 1017-keV transition. This deviation is an indication that the two components of the doublet represent transitions of different multipole character. In particular, the lower-energy component is determined from correlation coefficients a_2 = -0.13(6), a_4 = 0.22(8), to possess dipole character, and the higher-energy component, with coefficients a_2 = 0.31(5), a_4 = -0.11(7), to possess quadrupole character. Given the quadrupole nature of the 746- and 1017-keV transitions, this supports $J = 5$ and $J = 6$ assignments for the 1078- and 1079-keV components, respectively. Although parity assignments cannot be unambiguously made from this type of angular correlation analysis, a positive parity is assigned to the $J = 6$ level at 2842 keV since it seems to be naturally part of the main

Table 3.8: Levels observed in ^{64}Fe from the PPP data.

E_{level} (keV)	J^π	E_γ (keV)	I_γ (rel.)	a_2	a_4
746	2^+	746.4(1)		0.14(3)	0.01(4)
1763	4^+	1016.7 (1)	100	0.14(3)	-0.09(3)
2841	$5^{(-)}$	1077.8(2)	12(3)[1]	-0.13(6)	0.22(8)
2842	6^+	1078.9(3)	50(7)[1]	0.31(5)	-0.11(7)
3423	(7^-)	582.0(2)	12(1)		
3528	>6	686.9(2)	20(2)		
3623	(8^+)	781.0(1)	30(2)	0.11(3)	-0.06(5)
4628	(10^+)	1005.4(5)	6(1)		

[1] The values 12(3) and 50(7) are estimated from coincidence relationships and feeding and decay intensity patterns. The value 58(3) was measured from the spectra.

yrast cascade. The 781-keV peak is too weak in intensity to obtain a reliable fit in any single coincidence gate, but the summation of 1017- and 1078.9-keV gates does produce a curve which supports a quadrupole character and, therefore, the level at 3623 keV is tentatively assigned $J^\pi = 8^+$, with the parity assignment following the same argument that was used for the 6^+ level. The level at 4628 keV is tentatively assigned a spin and parity of 10^+, since it appears to represent the extension of the yrast cascade toward higher angular momentum. All relevant a_2 and a_4 coefficients are given in Table 3.8.

The new level at 3529 keV appears to feed the 6^+ yrast level, and not the lower-energy 4^+ state, and, therefore, is assigned a spin of 6 or greater. As the new level at 3423 keV depopulates only to the spin 5 level at 2841 keV, and not to the 6^+ level at 2842 keV, a negative parity assignment for the 2841-keV level is favored and a tentative spin and parity of 7^- is favored for the 3423-keV state.

A coincidence gate on the 746-keV γ ray in the delayed spectrum did not give any indication for new transitions populated in the β decay of ^{64}Mn. If the data were present, one would expect the most intense transitions to occur at the same energy as those reported in the theses of Hannawald [93] and Gaudefroy [91], but none of these γ rays could be unambiguously identified, nor did coincidence gates with these transitions reveal any apparent new cascades. The absence of any strong feeding to the 4^+ state, as had been observed in the lighter isotopes, gave an *a priori* indication that a double-coincidence gate on 746- and 1017-keV γ rays would be fruitless and, indeed, this spectrum did not yield anything beyond a weak background.

3.8 Relative yields

The effect of different reaction systems on the relative yields of each Fe isotope is summarized in Figure 3.17. Here, the relative yield is evaluated in a somewhat rudimentary manner by (1) fitting the peak areas of all transitions that directly feed the 2^+ state in a coincidence gate on the $2^+ \rightarrow 0^+$ γ-ray transition and (2) fitting the peak areas of all transitions that directly feed the 4^+ state in a double-coincidence gate on the $4^+ \rightarrow 2^+$ and $2^+ \rightarrow 0^+$ γ rays in the prompt cube. The total efficiency-corrected peak areas are normalized to ^{60}Fe and the results from each method are plotted in Fig. 3.17.

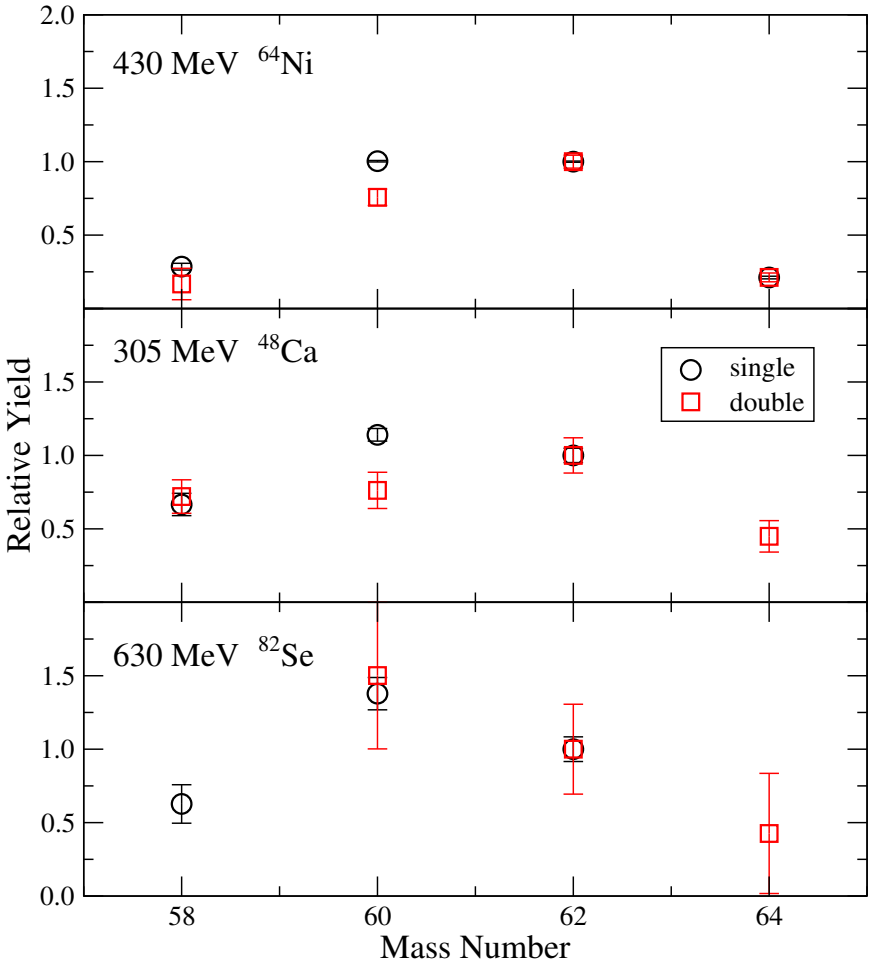

Figure 3.17: Relative yields for ^{64}Ni, ^{48}Ca, and ^{82}Se beams on ^{238}U in deep-inelastic reaction experiments. Statistical error from peak fitting is reflected in the error bars. In the plots, "single" denotes yields derived from a single coincidence gate on the $2^+ \rightarrow 0^+$ transition, and "double" denotes yields derived from a double-coincidence gate on $4^+ \rightarrow 2^+$ and $2^+ \rightarrow 0^+$ transitions.

Chapter 4

Discussion

4.1 Shell model calculations

Since the main issue to be addressed in this work relates to the role of the $g_{9/2}$ neutron orbital in the structure of Fe isotopes near $N = 40$, it is important that these results be illuminated by shell model calculations which include this orbital in the model spaces under consideration. One preliminary interaction was alluded to in section 1.2.2, in which the matrix elements from the *KB3G* effective interaction were complemented with $g_{9/2}$ matrix elements in calculations for Cr and Fe isotopes [49, 51, 54]. The results of those studies appeared to reproduce the 2^+ energy trends of these nuclei fairly well and, furthermore, seemed to indicate a need for $g_{9/2}$ and possibly $d_{5/2}$ orbitals in the model space. More recently, Matea *et al.* [85] and Vermeulen *et al.* [96] used the same interaction (per reference to [49]) to compute the energy, quadrupole moment, and g-factor of the $9/2^+$ isomer in ^{61}Fe. Likewise, this interaction was used to compute the levels of several Fe isotopes in the work of

Lunardi *et al.* [81]. However, the details of this effective interaction have not been published and, consequently, it was not possible to evaluate the results from this interaction in the present study. Furthermore, the authors of Refs. [81] and [85] cite different results for the $9/2^+$ energy in ^{61}Fe. Presumably, this is an artifact of different truncation methods used in the calculations, a point which will be discussed later.

There are also efforts to expand the *GXPF1A* interaction to allow for explicit excitations into the $g_{9/2}$ neutron orbital, but at present only preliminary results are available [97].

In the current work, shell model calculations are carried out with an effective interaction derived from the N3LO NN potential using the G-matrix methodology detailed in Ref. [9]. A ^{48}Ca core is assumed with a model space including the $\pi(f_{7/2}, p_{3/2}, p_{1/2}, f_{5/2})$ and $\nu(p_{3/2}, p_{1/2}, f_{5/2}, g_{9/2})$ orbitals. The single-particle energies adopted in this work were obtained from the spectra for ^{49}Sc (for protons) and ^{49}Ca (for neutrons) and are listed in Table 4.1 along with those typically used for *KB3G* and *GXPF1* interactions. No empirical modifications to the effective interaction were made, so the results presented here are based on a *pure G-matrix calculation*. All shell model calculations reported here were carried out with the Oslo shell model code [98].

A basic comparison of the results from the interaction mentioned in the previous paragraph with several interactions that have seen broad use in the literature is illustrated in Figure 4.1. The matrix elements for *KB3G*, *GXPF1*, and *GXPF1A* interactions were obtained from the Oxbash [99] package and converted to the Oslo

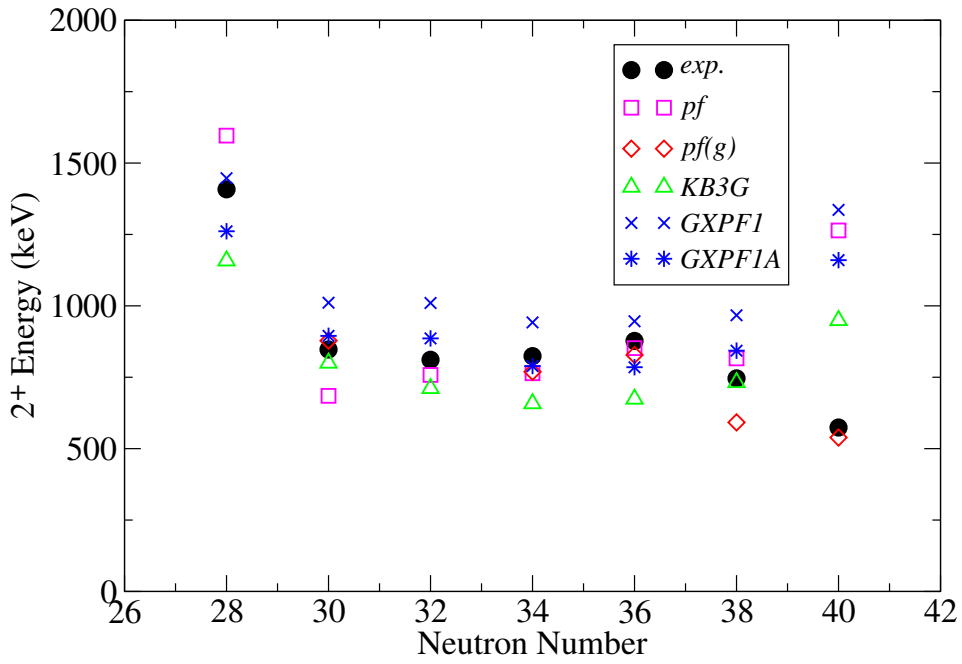

Figure 4.1: Results of shell model calculations for the 2^+ states of even-A Fe isotopes from $A = 54$ to 66.

format so that calculations could be carried out with the Oslo code. To allow for a full diagonalization of all the even-A Fe isotopes from $A = 54$ to 66, an "effective" ^{48}Ca core was used for *KB3G*, *GXPF1*, and *GXPF1A* calculations by disallowing excitations from the $\nu f_{7/2}$ orbital. As a result, the calculations may differ somewhat from those reported in the literature. For example, calculations for ^{56,58,60}Cr with *GXPF1A* yielded 2^+ energies 1010, 818, and 883 keV, whereas in Ref. [100] these are presented as 1071, 906, and 958 keV, respectively, a difference of less than 100 keV in each case.

Some interesting features are revealed in Fig. 4.1. For instance, all of the *GXPF1* calculations appear to overpredict the 2^+ energies, whereas the *GXPF1A* results are, in comparison, quite good. This is interpreted as a direct consequence of the fitting method used in the derivation of *GXPF1*, a point noted in section 1.1.3

Table 4.1: Single-particle energies adopted for several shell model effective interactions. Energies are in MeV.

Orbital	*pf(g)*	*KB3G*	*GXPF1(A)*
$\pi p_{1/2}$	4.493	4.000	4.487
$\pi f_{5/2}$	4.072	6.500	7.241
$\pi p_{3/2}$	3.087	2.000	2.945
$\pi f_{7/2}$	0.000	0.000	0.000
$\nu g_{9/2}$	4.072		
$\nu p_{1/2}$	2.023	4.000	4.487
$\nu f_{5/2}$	3.585	6.500	7.241
$\nu p_{3/2}$	0.000	2.000	2.945
$\nu f_{7/2}$		0.000	0.000

and detailed in Ref. [16]. The *KB3G* interaction gives very poor results in Fig. 4.1; this fact is intriguing since Caurier *et al.* [54] presented similar calculations which indicated quite good agreement with experiment. For example, those calculations were able to reproduce a slight downward trend in 2^+ energy from $^{62}Fe_{36}$ to $^{64}Fe_{38}$, whereas in Fig. 4.1, only the *pf* and *pf(g)* interactions are able to reproduce this characteristic. These latter two exhibit the most success in reproducing the experimental 2^+ energy trends. Note that, in Fig. 4.1, *pf* and *pf(g)* are identical except that excitations into the $\nu g_{9/2}$ orbital are blocked in *pf*. The parenthetical *g* in the latter indicates that a truncated $g_{9/2}$ orbital is available; namely, a maximum of 2 neutron excitations are allowed into this orbital. This truncation was required in order to keep the calculations tractable throughout the range $A = 54$ - 66 with the available resources. In the larger model space, the artificial rise in 2^+ energy is gone

and, in fact, the shell model result for $N = 40$ agrees quite well with the empirical result. However, the value for $N = 38$ is now considerably lower than experiment.

It was remarked earlier that shell model comparisons with 2^+ energy trends, while important, do not necessarily provide a rigorous means of determining nuclear structure characteristics. To this end, it is useful to compare several excited levels to shell model calculations and, only then, might the possibility of spurious agreement be ruled out or at least perceived as negligible. Hence, some "beyond the 2^+ energy" comparisons are summarized below.

4.1.1 Even-*A* Fe isotopes

Since the results for 2^+ energy calculations appeared in good agreement with experiment, it was of interest to expand the shell model comparisons up to higher spin. In Figure 4.2, the first few yrast states of ^{60,62,64}Fe are compared with *pf* and *pf(g)* shell model calculations. This figure also provides the predicted values for ^{66}Fe along with the 2^+ energy measured by Hannawald *et al.* [50] as well as tentative 4^+ and 6^+ states based on Refs. [101, 102]. The average occupation of the $g_{9/2}$ neutron orbital produced from the *pf(g)* calculations is indicated in the figure as well. This gives some indication that the model space used in these calculations is likely too small, since the $g_{9/2}$ occupation number quickly reaches the maximum value allowed in the truncated model space. Whereas the 0^+, 2^+, 4^+, and 6^+ states in ^{60}Fe show a negligible contribution from this orbital, these states have a moderate contribution in ^{62}Fe and the maximum allowed contribution in ^{64}Fe.

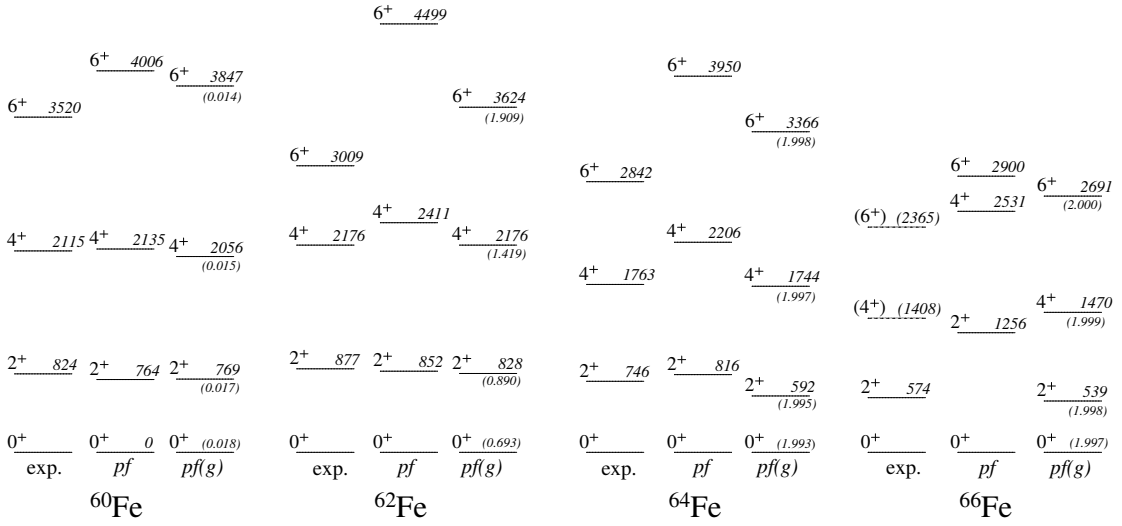

Figure 4.2: Shell model calculations for even-A Fe isotopes. The $g_{9/2}$ neutron occupation number is denoted in parentheses for each level from the *pf(g)* calculation, where a maximum occupancy of two neutrons was allowed. Tentative excited states from Refs. [101, 102] are included in ^{66}Fe.

In general, these calculations demonstrate quite convincingly the significance of the $g_{9/2}$ neutron orbital for the yrast structure of Fe isotopes beyond ^{60}Fe. In that isotope, the larger configuration space gave nearly identical results to those of the smaller but, for instance, in the 4^+ and 6^+ states of ^{62}Fe, a noticeable effect on the excitation energy begins to emerge. In ^{64}Fe, the difference is even more pronounced, and extends to the 2^+ energy, which deviates by nearly 300 keV below the experimental value. Thus, it might be speculated that the calculation predicts too significant a contribution from the $g_{9/2}$ orbital in this state. In contrast, the 2^+ energy for ^{66}Fe compares well with experiment, and this appears to extend to 4^+ and 6^+ states when the values of Refs. [81, 102] are adopted. Finally, it should be emphasized that the 6^+ states are predicted too high for nearly all of the nuclei displayed in Fig. 4.2. The larger configuration space does provide some improvement, but the results are still somewhat unsatisfactory.

The negative-parity states of the even-A Fe isotopes can be characterized in terms of a neutron excitation into the $g_{9/2}$ orbital. Unfortunately, the parity of a nuclear state is not determined in a trivial manner, and the experiments described in this work could only lead to tentative assignments, based mostly on systematic comparisons with lighter isotopes for which more information is available. With this in mind, it is noted that any agreement between experiment and theory exhibited in the yrast states of Fig. 4.2 quickly deteriorates for the negative-parity states. In a comparison between proposed 5^- and 7^- states with their respective shell model values, neither the excitation energy, relative spacing, nor the systematic trends of the proposed 5^- and 7^- states could be reproduced in the calculation. In fact, the computed values fluctuated considerably for $A = 60$, 62 and 64, varying from 5.7 MeV down to 1.9 MeV and back up to 6.2 MeV for the 5^- state. This compares to the measured values 3.5, 3.0, and 2.8 MeV, respectively. The computed 5^+ states appear to exhibit somewhat better agreement, but any conclusions drawn from this would be presumptive as this positive relationship could very well be accidental.

4.1.2 Odd-*A* Fe isotopes

Efforts to compute the $9/2^+$ states of odd-A Fe isotopes suffered a similarly disconcerting fate as those for the negative-parity states described above. In this case, the $9/2^+$ energy for ^{59}Fe is grossly overpredicted, but the value for ^{61}Fe is nearly half the empirical value, and the shell model value is further reduced to 247 keV in ^{63}Fe, for which an experimental value is as yet undetermined.

Driven by recent attempts at computing the measured properties of the $9/2^+$ isomer in ^{61}Fe, a considerable effort was spent on shell model calculations for this nucleus. In Ref. [85], a truncation scheme allowing "up to 6p−6h excitations for both protons and neutrons" gave rise to an excitation energy of 720 keV for this state. In Ref. [81], a different scheme yielded a value of 308 keV with the same interaction. In the present work, implementation of the truncation scheme used in Ref. [85] gave an energy of 632 keV for the $9/2^+$ state, whereas the truncation used in the preceding section gave a value of 427 keV. Clearly, this value is largely dependent on the truncation scheme that is implemented and a full model space calculation would be ideal. What is not mentioned in Ref. [85] are the details of the other states in ^{61}Fe, which also tend to vary from one truncation scheme to another. In Ref. [81], some additional excited states are presented which compare fairly well with the levels identified in that work.

In the present work, a much simpler truncation method is adopted for the calculation of states in ^{61}Fe: protons are "frozen" in the $f_{7/2}$ orbital, and neutrons are allowed to distribute throughout the available model space, with a maximum of two neutrons allowed in the $g_{9/2}$ orbital. Surprisingly, the resulting calculation reproduced the negative-parity states and the relative energy spacing of the positive-parity states fairly well, as depicted in Figure 4.3, although the $9/2^+$ energy was computed nearly 1.3 MeV too high. This state, along with the positive-parity band built on top, could be lowered in energy by lowering the $\nu g_{9/2}$ single-particle energy, a move that had a negligible effect on all other computed states in the nucleus. Upon lowering this value by 1.7 MeV, the $9/2^+$ state rested at a value 897 keV.

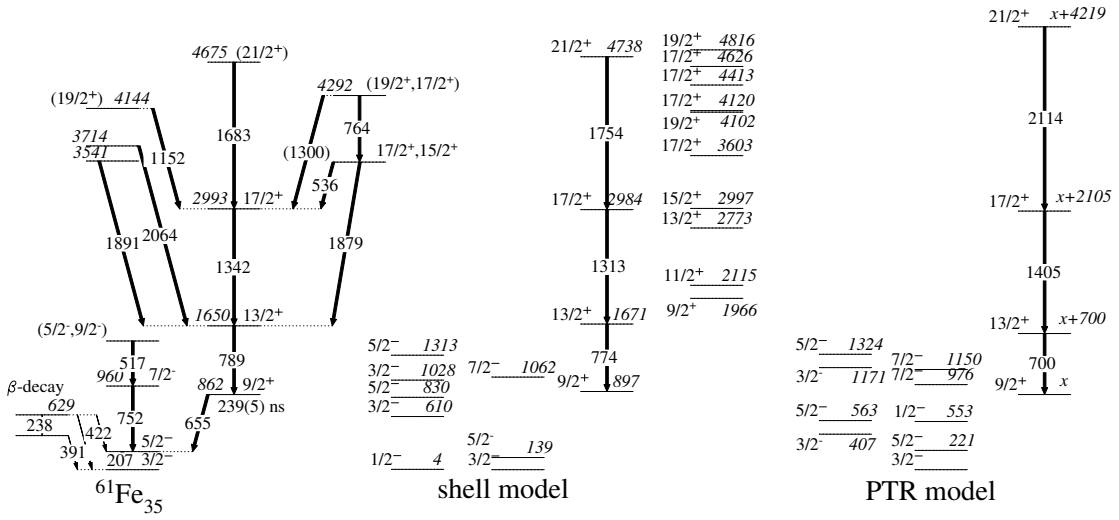

Figure 4.3: Comparison of the level scheme adopted for ^{61}Fe and the results of shell model and PTR model calculations. For simplicity, only calculated yrast and near-yrast levels are given. The arrows linking the calculated levels are presented to highlight the agreement between theory and experiment.

Using the wave functions from the calculation detailed above, the intrinsic quadrupole moment could be derived. To this effect, the reduced transition rate was computed with the $9/2^+$ state designated as both the initial and final state. The result, with eqn. (2.12), gave the result $Q_0 = +116\ e\ \mathrm{fm}^2$. Note that a factor 2^4 was included since an oscillator length 1 fm is "hardwired" into the code, whereas a length 2 fm is more realistic for a ^{48}Ca core [103]; the exponent comes from the units of *B(E2)*. This result converts readily to a spectroscopic quadrupole moment Q_s = -42 e fm^2 if $K = 1/2$ is assumed, or Q_s = 63 e fm^2 if $K = 9/2$ is assumed (per eqn. (2.13)). Hence, the results from the shell model calculation appear to compare well with the measured value $Q_s = |42|\ e\ \mathrm{fm}^2$, if $K = 1/2$ and, consequently, prolate deformation is assumed.

4.1.3 Summary

Clearly, the biggest impedance to the success of these shell model calculations is the necessity to use a truncated model space. The large dependence of ^{61}Fe results on the method of truncation speaks volumes to this end. Thus, it would be of interest to pursue a more rigorous theoretical investigation in order to see how the results summarized here are affected. However, it is also of interest to pursue an effective interaction that would be expected to agree with experimental data on a larger scale. The interaction used here, based on the N3LO NN potential without empirical modification of the matrix elements, appears to reproduce many of the systematic features of the Fe isotopes within a reasonable error. This agreement was manifested in the even-A yrast calculations of Fig. 4.2, but seemed to break down for most calculations involving the $g_{9/2}$ neutron orbital.

4.2 Rotation-aligned coupling and prolate shape in ^{61}Fe

One of the striking features brought to light by the new data in ^{61}Fe is the strong correlation between the first few yrast levels in ^{60}Fe and those of the $9/2^+$ band in ^{61}Fe, as displayed in Figure 4.4. This phenomenon is not new, but rather a continuation of a trend extending back to the ^{56,57}Fe and ^{58,59}Fe pairs. As described in section 1.1.4, this is the primary signature of a phenomenon called rotation-aligned coupling, where the band associated with an excitation into a unique-parity

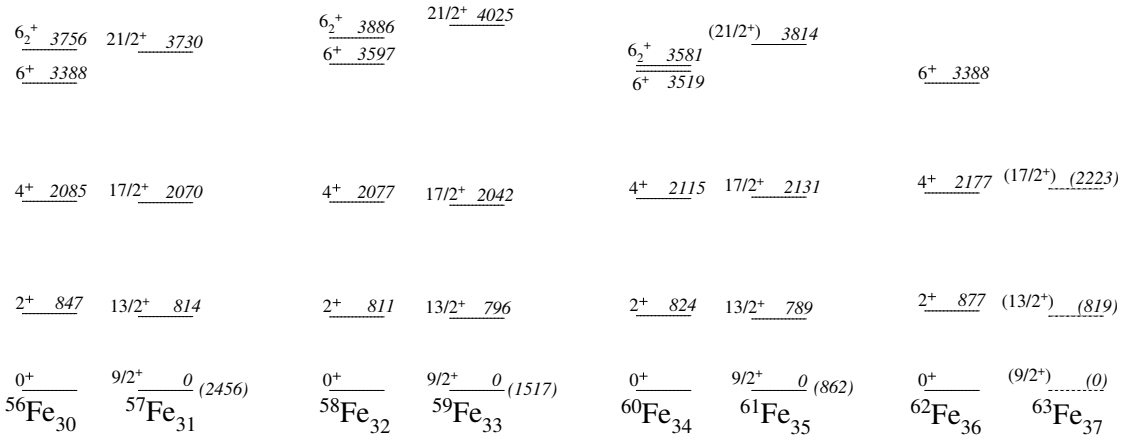

Figure 4.4: The yrast levels in even-A Fe isotopes are compared with $9/2^+$ band excitations in the associated $A-1$ isotope. For the odd-A isotopes, energies are given relative to the $9/2^+$ state. Tentative levels in ^{63}Fe are also depicted [81].

orbital decouples from the structure of the odd-A nucleus and resembles rather closely that of the neighboring $A-1$ system. In this case, the decoupled band is formed by a neutron excitation into the $g_{9/2}$ orbital. Since this is an intruder orbital possessing a parity opposite to that of the other pf-shell orbitals, the configurations can remain relatively pure and this weak coupling scheme can be expected to remain valid. Other textbook examples of rotation-aligned coupling have been presented, for example, in the Ba/La nuclei [32, 33], in which case an odd proton excited into the unique-parity $h_{11/2}$ orbital creates a similar decoupling, resulting in a band that closely parallels the yrast levels of the neighboring even Ba isotopes. One of the important consequences of this phenomenon is the implication of a prolate shape. Whereas the formalism associated with rotation-aligned coupling rests on the assumption of a rotational structure for the $A-1$ system, Stephens [32] points out that this phenomenon is present only for moderately-deformed systems with $\beta_2 \sim 0.2$; consequently, the rigid-rotational signature may be absent in the respective $A-1$

nuclei. This is, in fact, the case for ^{60}Fe, where Deacon *et al.* [76] recently presented new results and gave no indication of a rotational structure in their interpretation of this nucleus. It is worth noting, as well, that new results from deep-inelastic work at Legnaro [81] indicate that this trend may extend to ^{63}Fe, as the tentatively-assigned $17/2^+ \rightarrow 13/2^+$ and $13/2^+ \rightarrow 9/2^+$ transition energies appear to closely resemble those of ^{62}Fe yrast transitions (see Fig. 4.4.

In an attempt to reproduce the decoupled band structure in ^{61}Fe, calculations were carried out within the Particle-triaxial-rotor (PTR) model [104]. For these calculations, standard parameters κ and μ of the modified oscillator potential were used, as defined in Ref. [105]. Pairing was treated in the standard BCS approximation with parameters GN0 = 22.0 and GN1 = 8.0 [106], and the core was taken to be ^{60}Fe. The calculations for negative- and positive-parity levels had to be carried out separately and, as such, the relative energy of the $9/2^+$ isomer could not be assessed. Nevertheless, the results of these separate calculations, displayed in Fig. 4.3, appear to be in agreement with experiment. The negative-parity results were obtained under an assumed ground-state deformation $\beta_2 = 0.22$, and the positive-parity results were obtained under an assumed deformation $\beta_2 = 0.25$. Thus, the PTR model predicts a similar prolate shape for both the ground state and the $9/2^+$ isomer. This is consistent with several recent predictions of ground-state deformation in this nucleus calculated from mean-field models including FRDM, ETFSI-1, and RMF, for which the results were 0.20, 0.17, and 0.21 (^{60}Fe), respectively [107–109].

The PTR model was also applied in a calculation of spectroscopic quadrupole and magnetic dipole moments for the $9/2^+$ state as a function of deformation. The

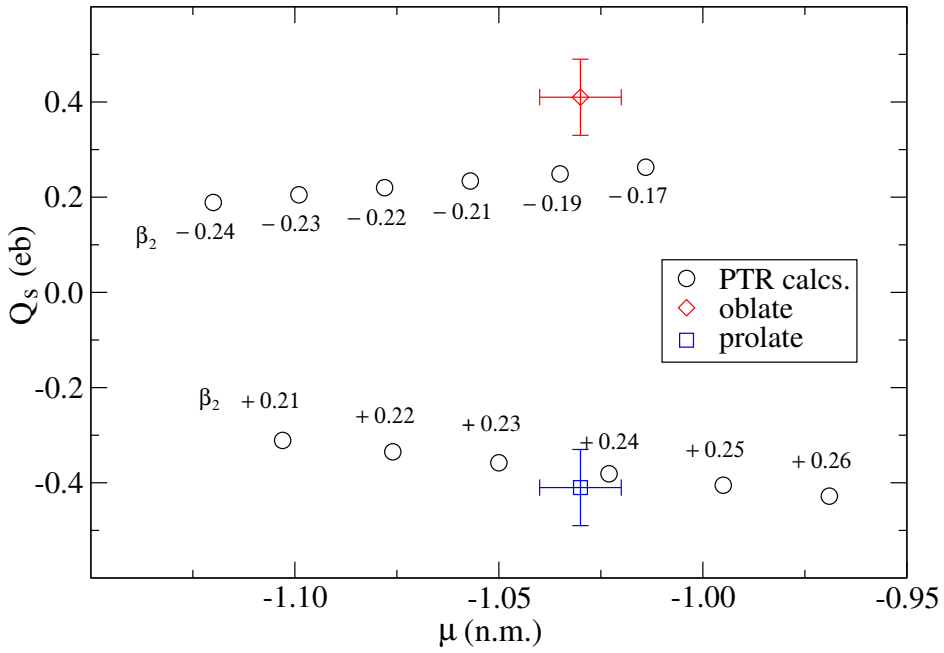

Figure 4.5: Results from the PTR calculations for the cases of prolate (K=1/2) and oblate (K=9/2) deformation. Calculated data points are labeled with the β_2 deformation used in the calculation. The experimental values are consistent with a prolate deformation of $\beta_2 \sim 0.24$.

results of this calculation, illustrated in Figure 4.5, favor a prolate deformation with $\beta_2 \sim 0.24$. Only in this region do the computed values simultaneously lie within the experimental error bars established in Refs. [85] and [96]. For an assumed oblate deformation no such region exists.

To assess the practical feasibility of the interpretation of a prolate band, it is important to consider the lifetimes of excited states within this band with respect to the stopping time of product nuclides in the target. Of primary concern is whether stretched quadrupole transitions in a prolate band would proceed faster than the time it takes for ^{61}Fe to stop in the target. If this were the case, the transitions would be Doppler broadened sufficiently that it would be impossible to observe them in a thick-target deep-inelastic reaction experiment. Given $Q_0 = +115\ e\ \mathrm{fm}^2$, one

can estimate the mean lifetime of the 1342-keV, $17/2^+ \rightarrow 13/2^+$ transition to be $\tau \approx 0.4$ ps according to eqns. (2.8) and (2.12). This compares to a stopping time of ^{61}Fe in ^{238}U on the order of 1 ps. As the two values are comparable in magnitude, one would expect some degree of broadening in the 1342-keV peak. In fact, some Doppler broadening is evident in the spectra of Figs. 3.7 and 3.8, so the contention of a deformed band with stretched quadrupole transitions is not unreasonable. Not only that, but the absence of any transitions beyond $J^\pi = 21/2^+$ might be attributed to the fact that the transition rate increases further up the band rendering all higher spin transitions impossible to observe due to severe Doppler broadening.

To summarize, the shell model, PTR model and the rotation-aligned coupling scheme all appear to favor the interpretation of a prolate shape for the $9/2^+$ isomer in ^{61}Fe. Shell model calculations indicated a deformation $\beta_2 = 0.23$ and the PTR model $\beta_2 = 0.24$. These values are in agreement with the value $\beta_2 = 0.24$, derived from the measured quadrupole moment of Ref. [96] if $K = 1/2$ is assumed. However, all this is particularly intriguing in view of the recent interpretation of mild oblate shapes characterizing ^{59}Cr [110] and ^{60}Cr [100], derived from comparisons with total routhian surface (TRS) calculations. Since ^{61}Fe and ^{59}Cr are isotones separated by only two protons, it is surprising that such a change in structure would occur for two nuclei so close. To better address this issue, a further elucidation of excited states in ^{59}Cr is necessary so that characteristics of the band built on top of the $9/2^+$ state can be determined. It may also prove important to identify additional levels on top of the $9/2^+$ isomer in ^{61}Fe; for example, a weakly-populated $11/2^+$ state between $9/2^+$ and $13/2^+$ states would provide further confirmation of the rotation-aligned

coupling scheme. More sophisticated "beyond the mean field" calculations might also shed some light on this issue.

4.3 Parallel trends and systematics

It is often useful to compare the systematic behavior of nuclei spanning across shells or entire regions of the nuclear chart. Such a global approach can often reveal subtle features and structural similarities in nuclei. With this in mind, the 2^+ energies of several nuclei on both sides of the $Z = 28$ magic number are plotted in Figure 4.6a. It is remarkable to note the similar trends of Cr/Kr, Fe/Se, and Zn/Ge isotopic chains that are emphasized in this picture. An *ad hoc* explanation for this might relate the interaction between the respective valence proton orbitals and the $g_{9/2}$ neutron orbital. In this spirit, one would propose that the 2^+ energies in the $_{30}$Zn and $_{32}$Ge nuclides reflect the filling of the $p_{3/2}$ proton orbital, and, therefore, the trends of Fig. 4.6a reflect the interaction between $p_{3/2}$ protons and $g_{9/2}$ neutrons. Similarly, the presence of two holes in the $f_{7/2}$ and two particles in the $f_{5/2}$ proton orbitals manifests itself in the $_{26}$Fe and $_{34}$Se nuclei, respectively, while the $_{24}$Cr and $_{36}$Kr nuclides represent four holes in the $f_{7/2}$ and four particles in the $f_{5/2}$ orbitals.

The above interpretation may appear somewhat whimsical, but with the application of new data obtained in this work, it is revealed that the 2^+, 4^+, 6^+, 8^+, and 10^+ level sequence of $^{64}Fe_{38}$ appears to compare rather well to that of $^{72}Se_{38}$, with only the difference in 6^+ energies exceeding 200 keV. This energy difference might be explained, at least qualitatively, as arising from the fact that the 6^+ state

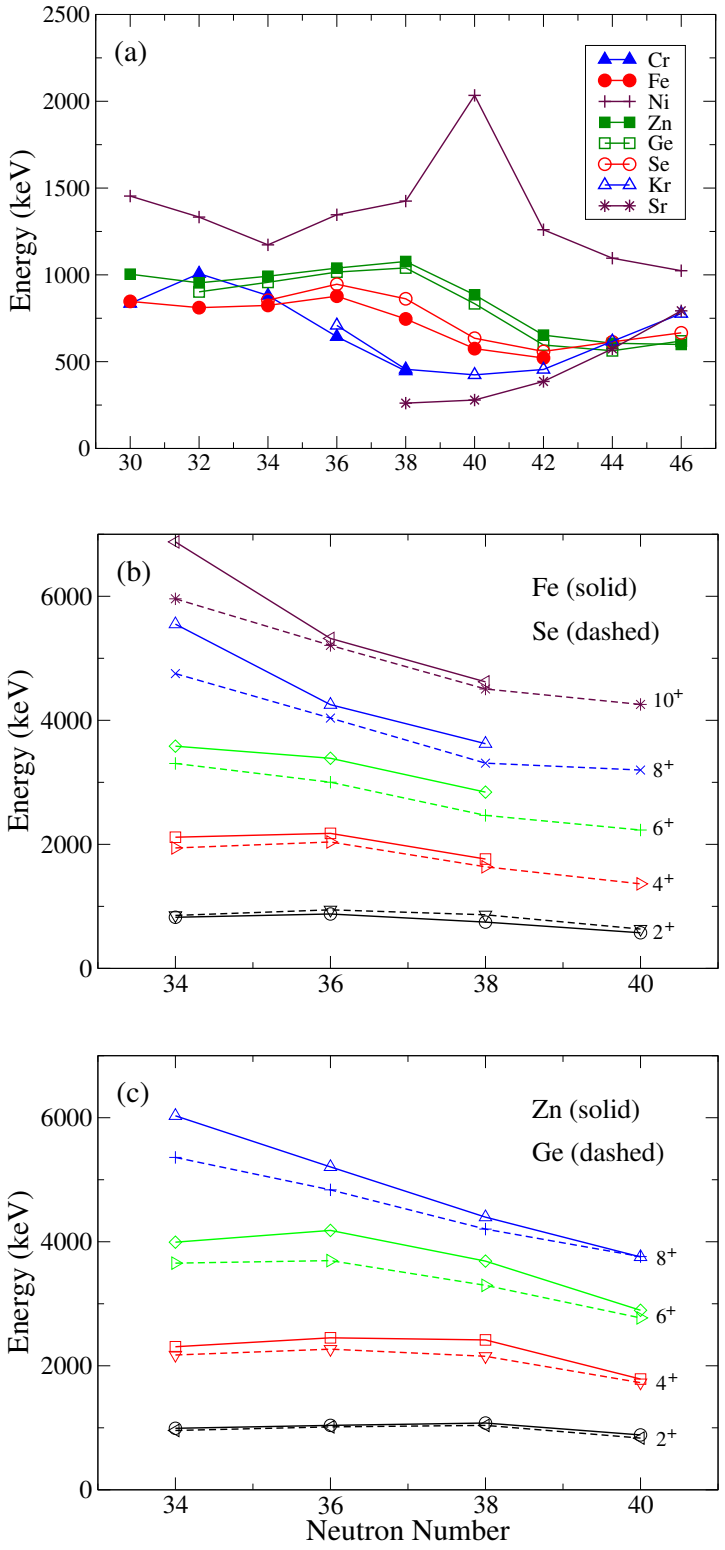

Figure 4.6: (a) The 2^+ energy trends for selected nuclides around ^{68}Ni exhibit intriguing parallels. This comparison is extended to higher spin in (b) Fe/Se and (c) Zn/Ge isotopes.

in ^{64}Fe is likely dominated by the maximally aligned two-proton hole configuration from the $f_{7/2}$ orbital, whereas the analogous configuration with $f_{5/2}$ protons in Se can only reach 4^+. Despite this single nonconcurrence, the rather extensive similarity between the yrast states of these two nuclei can be viewed as an indication that the underlying configuration and structural characteristics are comparable, at least to first order. An extension to this idea is depicted in Figure 4.6b where a similar agreement appears in ^{62}Fe/^{70}Se, but a breakdown of this scheme is presented in the higher-lying states of ^{60}Fe/^{68}Se. A comparison of the Zn and Ge isotopes in Fig. 4.6c gives a striking result for the 2^+, 4^+, 6^+ and 8^+ levels at $N = 40$, which differ by only 51, 58, 123, and 6 keV, respectively.

In an effort to extract some predictability out of the above trends, one can estimate the anticipated energies for ^{66}Fe beyond the 2^+ state. In fact, the recent results of Refs. [101, 102] have indicated two new γ rays in this nucleus at 834 and 957 keV which likely belong to the $6^+ \rightarrow 4^+$ and $4^+ \rightarrow 2^+$ transitions (actually, the 834-keV transition was previously reported in Ref. [50]). The corresponding energies in ^{74}Se imply a deviation of the order 50 keV if the 834-keV γ ray depopulates the 4^+ state and the 957-keV γ ray the 6^+. It should also be noted that these energies compare favorably with the shell model calculation depicted in Fig. 4.2.

4.4 On the issue of deformation

The 2^+ energy trends for Fe isotopes provided one of the primary motivations for this work. In particular, the downward trend exhibited for ^{64}Fe$_{38}$ and ^{66}Fe$_{40}$

stimulated much discussion about a possible new region of deformation. As this speculation has been almost exclusively based on 2^+ energy trends, the main focus of this project was to expand the known level schemes for Fe isotopes near $N = 40$ with the idea that this data would be sufficient to firmly characterize the structures of these isotopes. Unfortunately, the theoretical work presented here is somewhat limited so that a thorough assessment of deformation in the Fe isotopes cannot be presented with rigor. In principle, one can draw upon the success of shell model calculations by applying the computed wave functions to the determination of transition rates and, consequently, the deformation similar to the manner in which the quadrupole moment was computed for the $9/2^+$ state in ^{61}Fe. It would then be important to compare these values with experimental measurements, which are currently unavailable (although there are currently plans to carry out such measurements [111]). This being said, the experimental data made available in this work, along with an array of complementary work carried out prior to, in parallel with, and subsequently to this work, should provide the data necessary for a proper theoretical assessment in terms of the shell model. With a semi-empirical effective interaction derived in the spirit of successful interactions like *GXPF1*, the issue of monopole shift can be reliably addressed; namely, one can test the hypothesis that a reduced occupation of the $\pi f_{7/2}$ orbital results in a weakened tensor interaction with the $\nu f_{5/2}$ which then lessens the $N = 40$ subshell gap. The ESPE for this orbital can already be traced with the *GXPF1* interaction, but it is important to expand this to include also the $\nu g_{9/2}$ orbital so that the features of the $N = 40$ gap can be characterized.

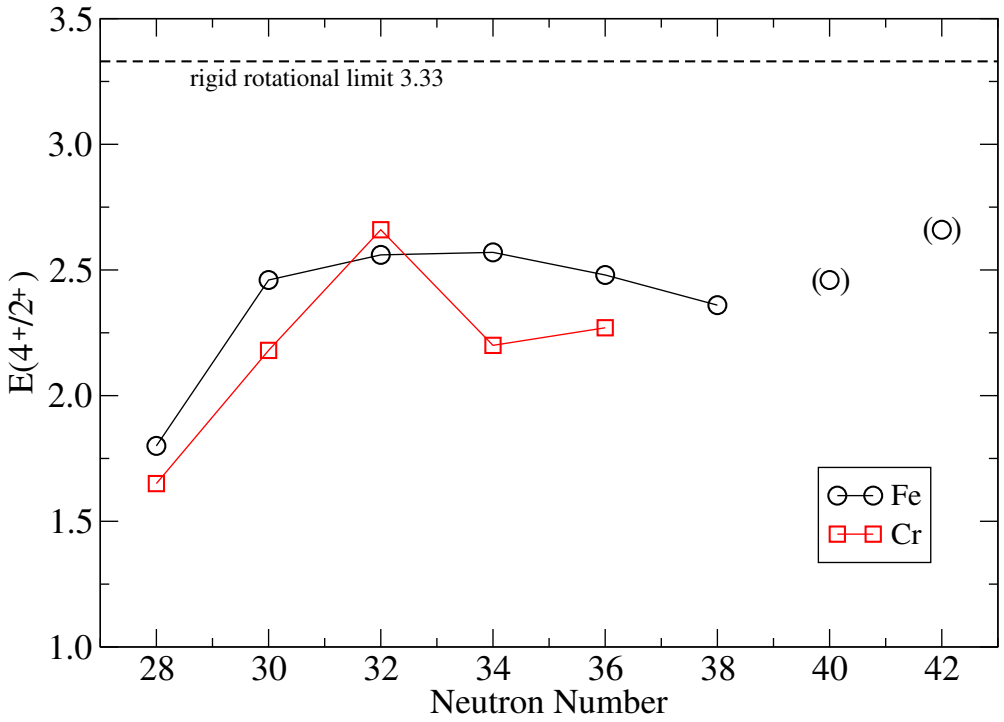

Figure 4.7: The 4^+ to 2^+ energy ratios for Fe and Cr isotopes do not approach the rigid rotational limit 3.33. Rather, these ratios appear to trend in the opposite direction up to $N = 38$. Additional data points at $N = 40$ and 42 are proposed on the basis of data from Refs. [101, 102].

One important feature that can be addressed directly with the data obtained in this work is the progression of 4^+ to 2^+ energy ratios which can provide a signature for the presence of deformed rotational nuclei, as discussed in section 1.1.4. With the 4^+ state in ^{64}Fe now established at 1763 keV, this ratio turns out to be 2.36, which is significantly lower than the value 3.33 expected for a rigid rotor. In fact, the systematic trajectory exhibited by the Fe isotopes up to $N = 38$ shows a downward trend in this ratio away from the rigid rotational limit, as illustrated in Figure 4.7. This appears to be in direct contrast with what might be expected if the neutron-rich Fe isotopes were members of a new region of deformation as N approaches 40. An initial report of new γ rays in ^{66,68}Fe from the group at Legnaro [101] was recently

confirmed in two-proton transfer experiments performed at the NSCL [102]. Based on these data, tentative ratios for these isotopes are also included in this figure, where the trend now appears to be rising.

4.5 Conclusion

The influence of the $g_{9/2}$ neutron orbital on the structure of even-A Fe isotopes has been uniquely traced by comparison of new data obtained in this work with shell model calculations within both *pf* and truncated *pfg* configuration spaces. Although the shell model interaction applied in this work should be viewed as somewhat preliminary, the results paint a clear picture of the growing importance of the $g_{9/2}$ orbital as neutron number 40 is approached. New levels identified on top of the isomeric $9/2^+$ state in ^{61}Fe complement previous measurements of the magnetic and quadrupole moments for this state. Comparisons within the rotation-aligned coupling scheme, and calculations within the scope of the shell model and Particle triaxial rotor model each support the assignment of prolate shape to this state and the band built on top of it, with $\beta \approx 0.24$.

One should not lose sight of the importance of data obtained from this experiment which have not received a great deal of discussion in the present chapter. For instance, the confirmation of numerous spin assignments described in Chapter 3 has provided a small, but crucial contribution to the accumulated data in this region of the nuclear chart, which is absolutely necessary for testing new shell model interactions. In addition, much new data obtained from the off-beam coincidence spectra

has been used to confirm and to expand known β-decay level schemes. The best example of this comes from the greatly expanded decay scheme deduced for ^{62}Mn to levels in ^{62}Fe. Most of the transitions identified in the triple coincidence data were, subsequently, confirmed in the analysis of an older dataset from an experiment carried out at ISOLDE. The few peaks that could not be confirmed in that dataset were either doublet transitions or very weak even in the coincidence data. The presence of many of the states implied by these data indicate the presence of a β-decaying isomer in ^{62}Mn.

One of the primary objectives of this work was to shed further light on the contention of a growing nuclear deformation in the Fe isotopes near $N = 40$. It was demonstrated that the 4^+ to 2^+ energy ratios do not conform to the rigid rotational limit often seen in deformed nuclei, although this is certainly not the last word on the matter. On the other hand, strong evidence has been provided for the rotation-aligned coupling scheme and small deformation in the $9/2^+$ bands of odd-A Fe isotopes. Still, the question of how and why the structures of these nuclei exhibit the observed behavior is not entirely resolved. To reach this goal, further experimentation and more sophisticated calculations will be necessary.

Appendix A

Isomeric decay of ^{128}Cd

In addition to the experiment described in the main part of this thesis, another was carried out at the National Superconducting Cyclotron Laboratory (NSCL) at Michigan State University in an effort to study isomeric decay of ^{128}Cd. This nucleus, like ^{64}Fe, can be viewed as two proton holes and two neutron holes in a double-magic system, except that in this case the double-magic system,^{132}Sn, has magic number 50 protons and magic number 82 neutrons. In contrast, the double-magic nucleus ^{68}Ni has semi-magic number 40 neutrons, which might be expected to be less robust once the proton magic number is removed. Surprisingly, a somewhat similar weakening of the $N = 82$ magic number was recently postulated for the Cd isotopes [112].

Whereas the primary goal of the experiment described in this section was to study ^{128}Cd, this project is a part of a larger campaign to study the neutron-rich Cd isotopes at the NSCL. This includes an experiment which employed a similar setup and which gave rise to new data for ^{125,126,127}Cd isomeric decay. Thus, the experimental details have already been described in Ref. [113] and the discussion

here will focus primarily on the analysis and results obtained specifically for ^{128}Cd, and the experiment will be described only very briefly.

A.1 Motivation

Interest in nuclei around closed shells generally focuses on whether or not the magic numbers persist away from stability. In the study of Fe isotopes described in the body of this thesis, the $N = 40$ subshell closure clearly dissolved when the magic proton number was changed. Since ^{132}Sn possesses two rigid magic numbers, such a sudden weakening in the shell closures is not expected. However, the reported 2^+ and 4^+ energies of ^{126,128}Cd$_{78,80}$ indicated lower values at $N = 80$ [112], contrary to the standard notion that these energies would rise as magic number $N = 82$ is approached. Hence, this was interpreted as a possible sign that the $N = 82$ shell closure had weakened.

These notions have been accompanied by specific failures in shell model calculations for this region of nuclei. For example, Korgul *et al.* [114] noted that shell model calculations for ^{134}Sn and ^{136}Te using the Kuo-Herling interaction [115] produced energies 40% higher than experimental observations; hence, the authors emphasized the need to apply a reduction factor of 0.6 to the calculated level energies in order to achieve better agreement with their data even after six $T = 1$ diagonal matrix elements had already been reduced by the same factor. Similarly, Terasaki *et al.* [116, 117] proposed a weakened neutron pairing interaction (again, reduced by a factor of 0.6) as the source of anomalous *B(E2)* and *E(2$^+$)* trends in $^{132-136}$Te.

Below the $Z = 50$ gap, Dillmann *et al.* [118] attribute the large discrepancy between the experimentally determined 1^+ level and the shell model calculations for ^{130}In to a weakened proton-neutron interaction.

The failures of shell model calculations could be a sign of unusual structural behavior, complementary to the puzzling 2^+ and 4^+ energy trends in the Cd isotopes, or it could simply reflect a deficiency in available shell model effective interactions in this region. In any case, the study of levels in ^{128}Cd is important to both confirm the previous measurement of the 2^+ energy and to provide additional levels for comparison with theoretical predictions. This nucleus is particularly important to the latter since it represents only four holes in double-magic ^{132}Sn, so dimensionality problems are less likely to affect the results (*ie:* there would be no need for truncations). However, if the $N = 82$ shell closure is found to be weakened, then the validity of ^{132}Sn as a shell model core could come into question.

A.2 Experimental setup

Neutron-rich Cd isotopes were produced in the fragmentation of a 120 MeV/u ^{136}Xe beam at the NSCL. The primary beam was made incident on a 188 mg/cm^2 Be target at the object position of the A1900 fragment separator [119], with primary focus on ^{128}Cd. A plastic scintillator was located at the intermediate image position of the A1900 separator and was used to correct the fragment time-of-flight.

The "cocktail" beam that reached the final counting position included both fully stripped fragments and fragments with one electron. Therefore, the typical

energy-loss versus time-of-flight spectrum used for particle identification will have charge ambiguities; specifically, nuclei with one electron and mass $A-3$ have approximately the same time-of-flight and energy loss values as their fully stripped counterparts with mass A. These species are separated by total kinetic energy as demonstrated in Ref. [120].

The final counting position was composed of a stack of Si detectors: three Si PIN detectors of thickness 991, 997, and 309 μm, a 979-μm thick double-sided (40 x 40 strips) Si detector (DSSD), and six single-sided (16 strips) Si detectors of 1 mm nominal thickness [121]. γ rays emitted by fragments reaching the Si stack were measured with 16 detectors from the MSU Segmented Germanium Array [122] arranged in two concentric rings around the vacuum beam line surrounding the stack. The γ-ray peak detection efficiency was $\sim$7% at 1 MeV, and the energy resolution for each of the Ge detectors was $\sim$ 3.5 keV for the 1.3 MeV γ-ray transition in ^{60}Co.

A.3 Data analysis

Data were sorted and analyzed in an event-by-event basis within the program *root* [68]. For the analysis of isomeric transitions, an event was required to produce a signal in the PIN detector directly in front of the DSSD and in both the front and back of the DSSD. This type of event was labeled an implant, and any γ rays detected within 15 μs of an implant were presumed to arise from isomeric decay.

Particle identification (PID) was obtained with a plot of energy loss versus time-of-flight, as depicted in the upper panel of Figure A.1. Here, the energy loss

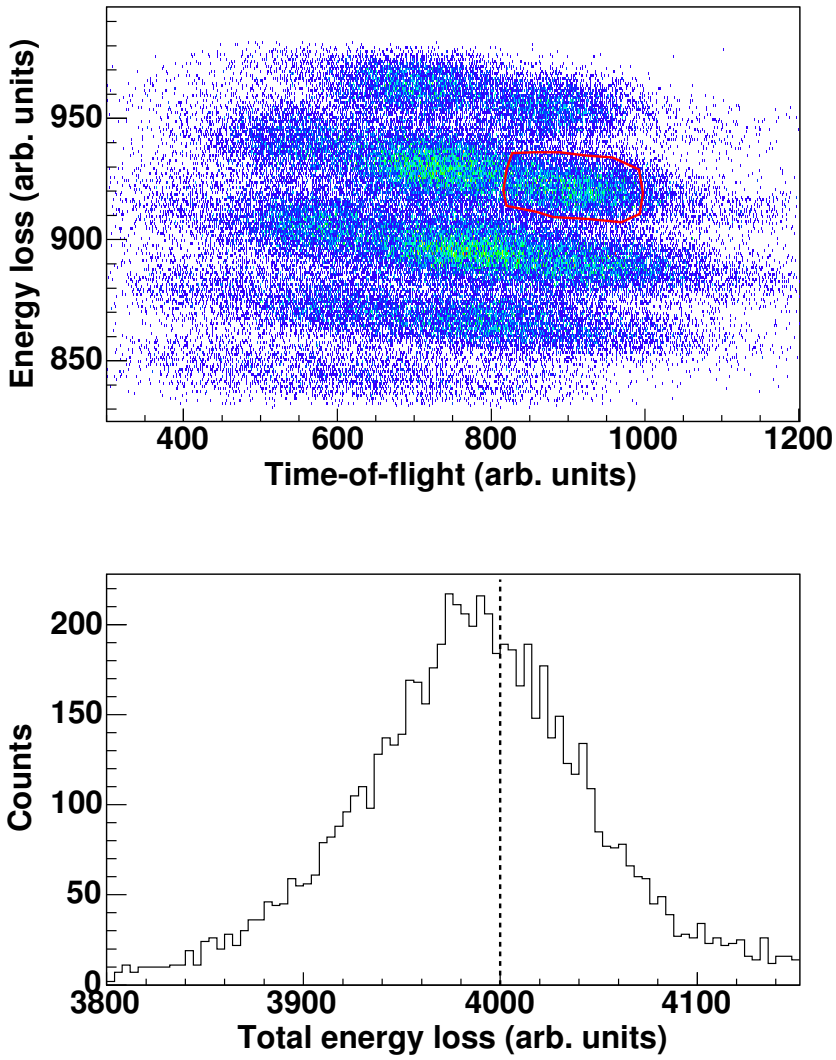

Figure A.1: (Upper panel) Particle identification plot with the ^{128}Cd region depicted, and (lower panel) the projection of energy loss within the ^{128}Cd region. The dotted line in the latter represents the charge-state cutoff to separate $^{128}Cd^{48+}$ and $^{125}Cd^{47+}$.

is the signal from the first PIN detector, and the time-of-flight is determined from an RF pulse that starts and stops according to signals in the first PIN detector and the scintillator, respectively (note that the RF pulse from the scintillator is delayed so that it provides the stop signal). The PID plot thus produces discrete regions which correspond to specific nuclides and their $A - 3$ charge-state contaminants.

Each region could be identified on the basis of the γ rays correlated with the events within that region, and charge-state separation was obtained by dividing the nuclide-gated energy loss projection into two regions (lower panel of Fig. A.1). The γ-ray background is further reduced by gating on the Cd region of a PIN01 versus PIN02 plot. The result is presented in Figure A.2.

A.4 Results

The five γ rays observed in Figure A.2 are arranged into two proposed level schemes depicted in Figure A.3. The two γ rays at 645 and 783 keV were reported previously by Kautszch *et al.* [112, 123] from the β decay of ^{128}Ag and proposed as the $2^+ \rightarrow 0^+$ and $4^+ \rightarrow 2^+$ transitions, respectively, based on the relative intensities of Ref. [124]. The remaining γ rays identified in this work were not seen in β decay, and are arranged in Fig. A.3 according to comparisons with ^{126}Cd, which is

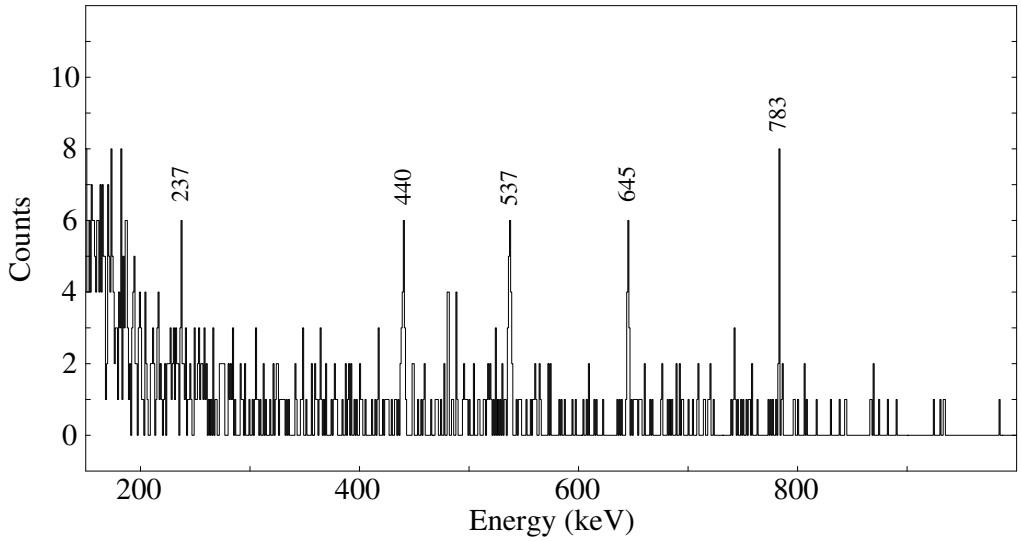

Figure A.2: The isomeric γ ray spectrum for ^{128}Cd obtained from this work.

also depicted in this figure along with partial level schemes for ^{122,124}Cd. Whereas isomeric decay in ^{126}Cd exhibits two pathways to the 4^+ level, only one such pathway appears to be present in ^{128}Cd. With only five observed γ rays, the decay path of the isomer appears to be limited either to the negative-parity path (arrangement A) that could include a low-energy $7^- \rightarrow 5^-$ transition that does not appear in the spectrum of Fig. A.2 or through a positive-parity path (arrangement B) including 8^+ and 6^+ levels. For arrangement A, the 434-keV γ ray is placed as the $5^- \rightarrow 4^+$ transition in order to bring the 5^- state close to that proposed in ^{126}Cd. Likewise, in arrangement B, the 540-keV γ ray is assigned as the $6^+ \rightarrow 4^+$ transition to bring the position of the 6^+ state close to the positions of the 6^+ states in the lighter Cd isotopes. In both cases the 237-keV γ-ray transition has been placed in a position depopulating a proposed 10^+ level, similar to the transitions in that energy range in ^{122,124,126}Cd. The relative intensities for the four highest-energy transitions are approximately equal to within one standard deviation. For the 237-keV transition the relative intensity is somewhat lower than the other four transitions and the possibility of other isomeric decays cannot be ruled out.

A.5 Discussion

The observation of 2^+ and 4^+ states in ^{128}Cd confirm the values proposed in Ref. [112]. A similar confirmation of these states in ^{126}Cd was given from isomeric decay reported in Ref. [113]. Scherillo *et al.* [125] were not able to identify these isomers from neutron-induced fission, but did report some shell model calculations

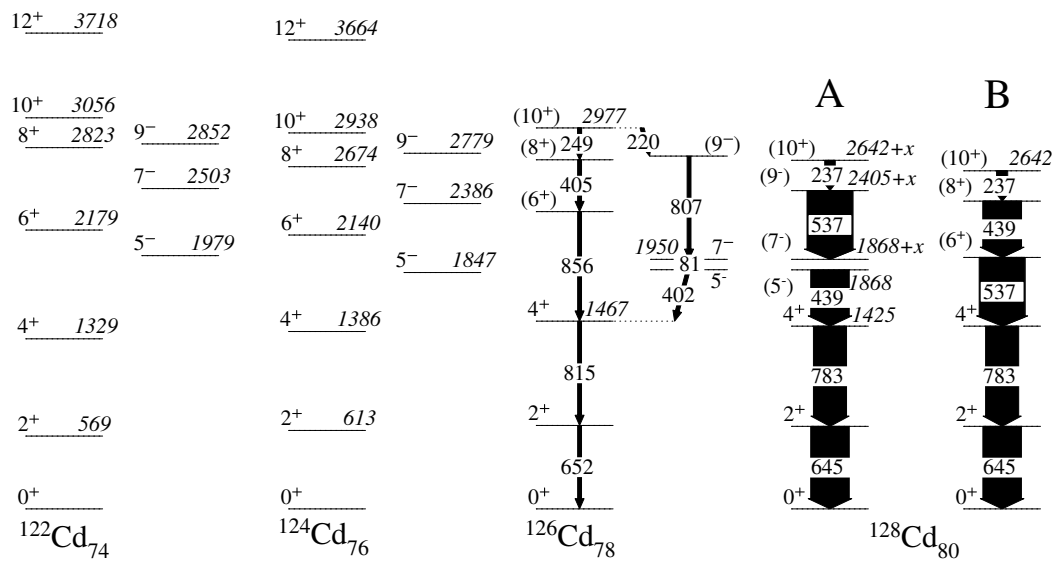

Figure A.3: Two possible level schemes are proposed for ^{128}Cd, based primarily on systematic comparisons with ^{122,124,126}Cd.

for ^{126,128}Cd, which are compared to the experimental results in Figure A.4. The authors of Ref. [125] noted the overestimated values for 2^+ and 4^+ states, but remarked that the $4^+ \rightarrow 2^+$ separation was reproduced quite well. In Fig. A.4, a similar trend can be seen for the relative spacing of higher-lying states in ^{126}Cd. With the new states proposed here, it is noted that the shell model results for ^{128}Cd appear to compare fairly well to arrangement B proposed in this work, although those authors did not report their results for the negative-parity states. Also included with Fig. A.4 are more recent shell model results [126], which exhibit somewhat better agreement with ^{126}Cd, but do not fare well for ^{128}Cd.

In a similar experiment recently reported by Jungclaus *et al.* [127], γ-ray transitions arising from isomeric decay of ^{130}Cd have led to the identification of several excited states in that nucleus. The adopted 2^+ energy of 1325 keV would seem to imply a persistent shell closure at $N = 82$, and shell model calculations in

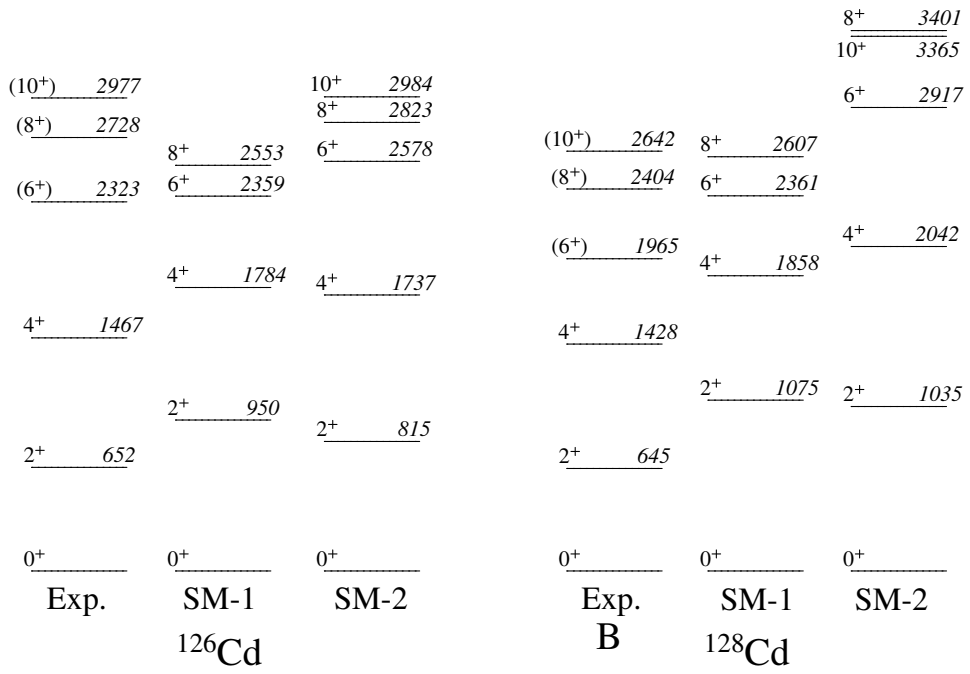

Figure A.4: Shell model calculations for ^{126,128}Cd. In the figure, *SM-1* were obtained from Ref. [125] and *SM-2* from Ref. [126]. Arrangement *B* is included for ^{128}Cd for convenience since negative-parity states were not reported in Ref. [125].

that report reproduce the results quite well (although those calculations have been explicitly "tuned" for use around ^{132}Sn).

In light of the results from Ref. [127], it is clear that the shell closure at $N = 82$ has not weakened substantially in ^{130}Cd. A similar conclusion appears to be unfolding in terms of the *B(E2)* values, where a downward trend up to ^{126}Cd has been observed [128–130]. However, the intriguing downward turn in the 2^+ and 4^+ energies of ^{128}Cd with respect to ^{126}Cd, which was confirmed here, remains to be sufficiently explained (although one possible interpretation of weakened *nn* and *pn* interactions was recently proposed in Ref. [131]).

Appendix B

Analysis of ^{62}Mn decay

In an experiment carried out prior to the work described here, the β decay of neutron-rich isotopes of Mn was studied using the ISOLDE facility at CERN. In this experiment, exotic nuclides were produced in reactions from a high-energy proton beam impingent on a thick uranium carbide target. The nuclides of interest were selectively ionized by applying a laser ionization scheme specifically tailored to Mn, and the ionized species were accelerated down a mass separator. The experimental setup included a moving tape collector, onto which the radioactive nuclides were implanted, and four Ge detectors for the identification of β-delayed γ rays. Further details pertaining to the experimental setup can be found in Refs. [50, 93]. However, it should be noted that, in spite of their being four detectors used for the experiment, the analysis carried out here has been applied to the spectra from a single detector only.

Whereas Refs. [50, 93] have described in detail the analysis in regards to decay of ^{64,66}Mn, the same experimental run provided data for ^{58}Mn and ^{62}Mn that

were never reported in the literature. Since the data at mass 62 is complementary to the coincidence data analyzed from the off-beam spectra for ^{62}Fe in the current experiment, it was of interest to complete the analysis of the older experiment so that the results could be compared with those of the present work.

The data obtained from the older experiment were available as raw spectrum files distinguished by the mass setting and run number. Energy and efficiency calibrations were performed by comparing spectra obtained at mass setting $A = 58$ with data from Ref. [72]. In that work, a rather complete assessment of β-delayed γ radiation from ^{58}Mn was described, and suitable calibrations could be determined by comparison to those data. In particular, the energy calibration involved a four-point fit to γ rays at 459, 811, 1323, and 1675 keV whereas the efficiency calibration included a fit to ten γ-ray peaks ranging in energy from 459 to 1790 keV. A comparison of energy centroids and efficiency-corrected relative intensities with known data from the literature for both ^{58}Fe and ^{62}Fe data is given in Tables B.1 and B.2.

Table B.1: γ-ray energies and relative intensities determined for ^{58}Fe from the ISOLDE data compared with data available in the literature.

This work		Ref. [72]	
E_γ (keV)	I_γ	E_γ (keV)	I_γ
459.2	2627(50)	459.2	2430(70)
524.0	454(30)	523.9	420(13)
632.9	38(17)	632.7	64(6)
810.8	10000(121)	810.8	10000(300)
864.0	1654(45)	863.9	1680(50)
925.7	156(23)	925.7	191(7)
1156.4	78(21)	1156.8	119(5)
1265.4	943(37)	1265.7	1030(30)
1323.1	6541(96)	1323.1	6730(200)
1674.7	1379(44)	1674.7	1320(40)
1767.8	377(28)	1767.7	360(15)
1789.5	290(25)	1789.6	325(10)
2421.1	107(20)	2422.5	127(3)
2637.7	215(21)	2638.2	151(4)
2818.0	59(14)	2818.5	96(3)

Table B.2: γ-ray energies and relative intensities determined for ^{62}Fe from the ISOLDE data compared with data available in the literature.

This work		Ref. [87]	
E_γ (keV)	I_γ	E_γ (keV)	I_γ
295.2	261(96)		
673.6	1406(117)		
831.6	289(71)		
838.0	146(71)		
877.1	10000(314)	876.8	10000
941.9	2868(155)	942.1	2560
1139.2	1072(108)		
1201.6	322(88)		
1299.0	3702(181)	1299.0	2780
1457.3	1633(125)	1457.4	1560
1538.8	262(94)		
1616.7	581(94)		
1814.2	2562(158)	1815.0	2560
2016.1	217(71)	2016.0	1110
2755.8	689(98)		
3172.3	104(51)		

Appendix C

Sample output from Oslo shell model code

```
\* Shell model calculation of proton/neutron system -- title: 62Fe_0p

<The basic shell data:>

\* The proton number: 6

\* The neutron number: 8

\* Total angular momentum J is (even, odd): even
\* Twice total projection of angular momentum: 0
\* Total parity (+, -): +

\* The number of proton particle j-orbits: 4

              <n  l  2*j    min_part   max_part  energy:>
\* Orbit_Z:    0  3   5        0          2     4.072
\* Orbit_Z:    1  1   3        0          4     3.087
```

```
\* Orbit_Z:   1  1   1        0          2     4.493
\* Orbit_Z:   0  3   7        0          6     0.000

\* The number of neutron particle j-orbits: 4

              <n   l  2*j    min_part   max_part energy:>
\* Orbit_N:   0   4   9        0          2      4.072
\* Orbit_N:   0   3   5        0          6      3.585
\* Orbit_N:   1   1   3        4          4      0.000
\* Orbit_N:   1   1   1        0          2      2.023

<The data files>
\* Input proton-proton v_effective in J-scheme:   v_pp_48Ca_pfg.dat
\* Input neutron-neutron v_effective in J-scheme: v_nn_48Ca_pfg.dat
\* Input proton-neutron v_effective in J-scheme:  v_pn_48Ca_pfg.dat

<Memory and file limitations - set >= ZERO>
wildenthal.pn
\* Memory to store nondiag <SD(Z)SD(N)|OP|SD(Z)SD(N)>(in Kb): 1000
\* File size to store nondiag <SD(Z)SD(N)|OP|SD(Z)SD(N)>(in Mb); 200

<Energy eigenvalue parameters>
\* Maximum Lanczos iterations: 95
\* Wanted number of converged eigenstates: 8

    *            Type of process                              Symbol
    * Lanczos iteration based on random initial
    * vector with global orthogonalization            -->random-start
    * Continue a previous random-start process        -->random-continue
    * Lanczos iteration based on generalized seniority
    * initial vector with global orthogonalization    -->fixed-J-start
    * Continue a previous fixed-start process         -->fixed-J-continue

\* Type of calculation process: random-start
```

<In case of fixed-J the following data must be specified>

* Total 2J value:

* Init vector file:

* Number of start vectors:

* List of vector no:

* END_OF_INPUT_FILE:

----- Results ----

Proton single-particle orbits for m >= 1/2 (symmetric around zero)

m_orb	j_orb	osc	l	par	2*j	2*m	energy	*	m_orb	j_orb	osc	l	par	2*j	2*m	energy
0	0	0	3	-	7	7	0.00	*	5	2	1	1	-	3	3	3.09
1	0	0	3	-	7	5	0.00	*	6	0	0	3	-	7	1	0.00
2	1	0	3	-	5	5	4.07	*	7	1	0	3	-	5	1	4.07
3	0	0	3	-	7	3	0.00	*	8	2	1	1	-	3	1	3.09
4	1	0	3	-	5	3	4.07	*	9	3	1	1	-	1	1	4.49

Neutron single-particle orbits for m >= 1/2 (symmetric around zero)

m_orb	j_orb	osc	l	par	2*j	2*m	energy	*	m_orb	j_orb	osc	l	par	2*j	2*m	energy
0	0	0	4	+	9	9	4.07	*	6	2	1	1	-	3	3	0.00
1	0	0	4	+	9	7	4.07	*	7	0	0	4	+	9	1	4.07
2	0	0	4	+	9	5	4.07	*	8	1	0	3	-	5	1	3.58
3	1	0	3	-	5	5	3.58	*	9	2	1	1	-	3	1	0.00
4	0	0	4	+	9	3	4.07	*	10	3	1	1	-	1	1	2.02
5	1	0	3	-	5	3	3.58	*								

Number of proton |SD> configurations = 30028

Number of neutron |SD> configurations = 1330

Total number of proton−neutron |SD> configurations = 2739128

******* Group data *******

k	parZ	parN	2*M_Z	2*M_N	numSD_Z	num_SD_N	tot_SD	sect
0	+	+	26	−26	0	0	0	
1	+	+	24	−24	10	1	10	
2	+	+	22	−22	32	3	96	
3	+	+	20	−20	90	8	720	
4	+	+	18	−18	194	14	2716	
5	+	+	16	−16	376	25	9400	
6	+	+	14	−14	633	35	22155	
7	+	+	12	−12	991	50	49550	
8	+	+	10	−10	1402	63	88326	
9	+	+	8	−8	1869	82	153258	
10	+	+	6	−6	2301	94	216294	
11	+	+	4	−4	2685	111	298035	
12	+	+	2	−2	2920	117	341640	
13	+	+	0	0	3022	124	374728	
14	+	+	−2	2	2920	117	341640	
15	+	+	−4	4	2685	111	298035	
16	+	+	−6	6	2301	94	216294	
17	+	+	−8	8	1869	82	153258	
18	+	+	−10	10	1402	63	88326	
19	+	+	−12	12	991	50	49550	
20	+	+	−14	14	633	35	22155	
21	+	+	−16	16	376	25	9400	
22	+	+	−18	18	194	14	2716	
23	+	+	−20	20	90	8	720	
24	+	+	−22	22	32	3	96	
25	+	+	−24	24	10	1	10	
26	+	+	−26	26	0	0	0	

```
The Lanczos iteration process has reached  maximum iterations
= 95 - specified in input data

Final Eigenvalues
The total parity is positive

E(0)=  -48.9856  <J**2> =  0.0000
Proton single-part. distrib.  :   7/2    5/2    3/2    1/2
                          N(j):   3.505  0.349  1.778  0.368
Neutron single-part. distrib. :   9/2    5/2    3/2    1/2
                          N(j):   0.693  1.893  4.000  1.413

E(1)=  -48.1580  <J**2> =  6.0000
Proton single-part. distrib.  :   7/2    5/2    3/2    1/2
                          N(j):   3.524  0.382  1.702  0.391
Neutron single-part. distrib. :   9/2    5/2    3/2    1/2
                          N(j):   0.890  1.799  4.000  1.312

E(2)=  -47.7733  <J**2> =  6.0000
Proton single-part. distrib.  :   7/2    5/2    3/2    1/2
                          N(j):   3.523  0.384  1.714  0.378
Neutron single-part. distrib. :   9/2    5/2    3/2    1/2
                          N(j):   0.882  1.808  4.000  1.310

E(3)=  -47.4935  <J**2> =  0.0000
Proton single-part. distrib.  :   7/2    5/2    3/2    1/2
                          N(j):   3.410  0.464  1.680  0.446
Neutron single-part. distrib. :   9/2    5/2    3/2    1/2
                          N(j):   1.319  1.562  4.000  1.119

E(4)=  -47.0709  <J**2> = 11.9999
Proton single-part. distrib.  :   7/2    5/2    3/2    1/2
                          N(j):   3.572  0.428  1.619  0.380
```

```
Neutron single-part. distrib. :   9/2    5/2    3/2    1/2
                          N(j):   1.103  1.699  4.000  1.198

E(5)=  -46.8909  <J**2> =  6.0069
Proton single-part. distrib.  :   7/2    5/2    3/2    1/2
                          N(j):   3.460  0.434  1.673  0.433
Neutron single-part. distrib. :   9/2    5/2    3/2    1/2
                          N(j):   1.164  1.641  4.000  1.196

E(6)=  -46.8096  <J**2> = 19.9982
Proton single-part. distrib.  :   7/2    5/2    3/2    1/2
                          N(j):   3.537  0.460  1.542  0.461
Neutron single-part. distrib. :   9/2    5/2    3/2    1/2
                          N(j):   1.420  1.519  4.000  1.061

E(7)=  -46.4029  <J**2> =  7.0914
Proton single-part. distrib.  :   7/2    5/2    3/2    1/2
                          N(j):   3.280  0.268  1.868  0.584
Neutron single-part. distrib. :   9/2    5/2    3/2    1/2
                          N(j):   0.751  1.789  4.000  1.460
```

Bibliography

[1] M. G. Mayer, Phys. Rev. **75**, 1969 (1949).

[2] O. Haxel, J. H. D. Jensen, and H. E. Seuss, Phys. Rev. **75**, 1766 (1949).

[3] S. Raman, C. W. N. Jr., and P. Tikkanen, At. Data Nucl. Dat. Tab. **78**, 1 (2001).

[4] www.webelements.com.

[5] I. N. Levine, *Quantum Chemistry* (Prentice Hall, 2000), 5th ed.

[6] A. Bohr and B. Mottelson, *Nuclear Structure, Vol. 2 Reissue* (World Scientific, 1998).

[7] P. J. Brussaard and P. W. M. Glaudemans, *Shell-Model Applications in Nuclear Spectroscopy* (North-Holland, 1977).

[8] B. A. Brown, Prog. Part. Nucl. Phys. **47**, 517 (2001).

[9] M. Hjorth-Jensen, T. T. S. Kuo, and E. Osnes, Phys. Rep. **261**, 125 (1995).

[10] D. J. Dean, T. Engeland, M. Hjorth-Jensen, M. P. Kartamyshev, and E. Osnes, Prog. Part. Nucl. Phys. **53**, 419 (2004).

[11] P. J. Ellis and E. Osnes, Rev. Mod. Phys. **49**, 777 (1977).

[12] W. A. Richter, M. G. V. D. Merwe, R. E. Julies, and B. A. Brown, Nucl. Phys. **A523**, 325 (1991).

[13] B. A. Brown, W. A. Richter, R. E. Julies, and B. H. Wildenthal, Ann. Phys. **182**, 191 (1988).

[14] S. Froneman, W. J. Naudé, W. A. Richter, J. A. Stander, and J. W. Koen, Z. Phys. **A327**, 469 (1987).

[15] M. Honma, T. Otsuka, B. A. Brown, and T. Mizusaki, Phys. Rev. C **65**, 061301(R) (2002).

[16] M. Honma, T. Otsuka, B. A. Brown, and T. Mizusaki, Eur. Phys. J. A **25**, 499 (2005).

[17] T. T. S. Kuo and G. E. Brown, Nucl. Phys. **85**, 40 (1966).

[18] T. T. S. Kuo, Nucl. Phys. **A90**, 199 (1967).

[19] G. E. Brown and T. T. S. Kuo, Nucl. Phys. **A92**, 481 (1967).

[20] T. T. S. Kuo and G. E. Brown, Nucl. Phys. **A114**, 241 (1968).

[21] T. Hamada and I. D. Johnston, Nucl. Phys. **34**, 382 (1961).

[22] E. Pasquini and A. Zuker, in *Proc. Conf. Physics of Medium-Light Nuclei*, edited by P. Blasi and R. A. Ricci (Florence, 1977), p. 62.

[23] A. Poves and A. Zuker, Phys. Rep. **70**, 235 (1981).

[24] E. Caurier, A. P. Zuker, A. Poves, and G. Martínez-Pinedo, Phys. Rev. C **50**, 225 (1994).

[25] G. Martínez-Pinedo, A. P. Zuker, A. Poves, and E. Caurier, Phys. Rev. C **55**, 187 (1997).

[26] A. Abzouzi, E. Caurier, and A. P. Zuker, Phys. Rev. Lett. **66**, 1134 (1991).

[27] R. Machleidt, F. Sammarruca, and Y. Song, Phys. Rev. C **53**, R1483 (1996).

[28] R. Machleidt, Phys. Rev. C **63**, 024001 (2001).

[29] R. Machleidt and D. R. Entem, J. Phys. G: Nucl. Part. Phys. **31**, S1235 (2005).

[30] D. R. Entem and R. Machleidt, Phys. Rev. C **68**, 041001R (2003).

[31] K. E. G. Löbner, M. Vetter, and V. Hönig, Nuclear Data Tables **A7**, 495 (1970).

[32] F. S. Stephens, Rev. Mod. Phys. **47**, 43 (1975).

[33] R. F. Casten, *Nuclear Structure From a Simple Perspective* (Oxford Science Publications, 2000), 2nd ed.

[34] R. K. Bansal and J. B. French, Phys. Lett. **11**, 145 (1964).

[35] Y. Utsuno, T. Otsuka, T. Mizusaki, and M. Monma, Phys. Rev. C **60**, 054315 (1999).

[36] E. Caurier, G. Martínez-Pinedo, F. Nowacki, A. Poves, and A. P. Zuker, Rev. Mod. Phys. **77**, 427 (2005).

[37] T. Otsuka, T. Suzuki, R. Fujimoto, H. Grawe, and Y. Akaishi, Phys. Rev. Lett. **95**, 232502 (2005).

[38] H. A. Bethe, *Elementary Nuclear Theory* (John Wiley & Sons, 1947).

[39] Blatt and V. Weisskopf, *Theoretical Nuclear Physics* (John Wiley & Sons, 1952).

[40] A. Ozawa, T. Kobayashi, T. Suzuki, K. Yoshida, and I. Tanihata, Phys. Rev. Lett. **84**, 5493 (2000).

[41] S. N. Liddick, P. F. Mantica, R. V. F. Janssens, R. Broda, B. A. Brown, M. P. Carpenter, B. Fornal, M. Honma, T. Mizusaki, A. C. Morton, et al., Phys. Rev. C **92**, 072502 (2004).

[42] J. I. Prisciandaro, P. F. Mantica, B. A. Brown, D. W. Anthony, M. W. Cooper, A. Garcia, D. E. Groh, A. Komives, W. Kumarasiri, P. A. Lofy, et al., Phys. Lett. **B510**, 17 (2001).

[43] D. C. Dinca, R. V. F. Janssens, A. Gade, D. Bazin, R. Broda, B. A. Brown, C. M. Campbell, M. P. Carpenter, P. Chowdhury, J. M. Cook, et al., Phys. Rev. C **71**, 041302(R) (2005).

[44] R. V. F. Janssens, B. Fornal, P. F. Mantica, B. A. Brown, R. Broda, P. Bhattacharyya, M. P. Carpenter, M. Cinausero, P. J. Daly, A. D. Davies, et al., Phys. Lett. B **546**, 55 (2002).

[45] C. Thibault, R. Klapisch, C. Rigaud, A. M. Poskanzer, R. Prieels, L. Lessard, and W. Reisdorf, Phys. Rev. C **12**, 644 (1975).

[46] E. K. Warburton, J. A. Becker, and B. A. Brown, Phys. Rev. C **41**, 1147 (1990).

[47] J. Dobaczewski, I. Hamamoto, W. Nazarewicz, and J. A. Sheikh, Phys. Rev. Lett. **72**, 981 (1994).

[48] R. Broda, B. Fornal, W. Królas, T. Pawłat, D. Bazzacco, S. Lunardi, C. Rossi-Alvarez, R. Menegazzo, G. de Angelis, P. Bednarczyk, et al., Phys. Rev. Lett. **74**, 868 (1995).

[49] O. Sorlin, S. Leehardt, C. Donzaud, J. Duprat, F. Azaiez, F. Nowacki, H. Grawe, Z. Dombrádi, F. Amorini, A. Astier, et al., Phys. Rev. Lett. **88**, 092501 (2002).

[50] M. Hannawald, T. Kautzsch, A. Wöhr, W. B. Walters, K. L. Kratz, V. N. Fedoseyev, V. I. Mishin, W. Böhmer, B. Pfeiffer, V. Sebastian, et al., Phys. Rev. Lett. **82**, 1391 (1999).

[51] O. Sorlin, C. Donzaud, F. Nowacki, J. C. Angélique, F. Azaiez, C. Bourgeois, V. Chiste, Z. Dlouhy, S. Grévy, D. Guillemand-Mueller, et al., Eur. Phys. J. A. **16**, 55 (2003).

[52] W. F. Mueller, B. Bruyneel, S. Franchoo, M. Huyse, J. Kurpeta, K. Kruglov, Y. Kudryavtsev, N. V. S. V. Prasad, R. Raabe, I. Reusen, et al., Phys. Rev. C **61**, 054308 (2000).

[53] H. Grawe, Acta Phys. Pol. **34**, 2267 (2003).

[54] E. Caurier, F. Nowacki, and A. Poves, Eur. Phys. J. A. **15**, 145 (2002).

[55] V. Weisskopf, Phys. Rev. **83**, 1073 (1951).

[56] A. de Shalit and I. Talmi, *Nuclear Shell Theory* (Dover Publications, 2004).

[57] P. Ring and P. Schuck, *The Nuclear Many-Body Problem* (Springer-Verlag, 1980).

[58] I. E. McCarthy, *Introduction to Nuclear Theory* (John Wiley & Sons, 1968).

[59] H. Frauenfelder, R. M. Steffen, S. R. D. Groot, H. A. Tolhoek, and W. J. Huiskamp, in *Alpha-, Beta-, and Gamma-Ray Spectroscopy, Vol. II*, edited by K. Siegbahn (North-Holland, 1965).

[60] G. F. Knoll, *Radiation Detection and Measurement* (John Wiley and Sons, 1979).

[61] I. Y. Lee, Nucl. Phys. A. **520**, 641c (1990).

[62] P. J. Nolan, F. A. Beck, and D. B. Fossan, Annu. Rev. Nucl. Part. Sci. **45**, 561 (1994).

[63] M. P. Carpenter, T. L. Khoo, I. Ahmad, R. V. F. Janssens, T. Lauritsen, G. A. Annan, A. M. Baxter, M. E. Bleich, S. Harfenist, E. F. Moore, et al., Nucl. Instrum. Meth. A **353**, 234 (1994).

[64] M. Lefort, in *Heavy Ion Collisions*, edited by R. Bock (North-Holland, 1980).

[65] R. Broda, B. Fornal, W. Królas, T. Pawłat, J. Wrzesiński, K. H. Maier, H. Grawe, M. Schramm, R. Schubart, D. Bazzacco, et al., in *Sanibel* (1998), p. 202.

[66] R. Broda, J. Phys. G **32**, R151 (2006).

[67] B. Fornal, S. Zhu, R. V. F. Janssens, M. Honma, R. Broda, B. A. Brown, M. P. Carpenter, S. J. Freeman, N. Hammond, F. G. Kondev, et al., Phys. Rev. C **72**, 044315 (2005).

[68] R. Brun and F. Rademakers, Nucl. Instrum. Meth. A **389**, 81 (1996).

[69] D. C. Radford, Nucl. Instrum. Meth. A **361**, 297 (1995).

[70] R. Holzmann, I. Ahmad, R. V. F. Janssens, T. L. Khoo, D. C. Radford, M. W. Drigert, and U. Garg, Nucl. Instr. Meth. A **260**, 153 (1987).

[71] *www.nndc.bnl.gov/ensdf.*

[72] K. Tirsell, L. Multhauf, and S. Raman, Phys. Rev. C **10**, 10 (1974).

[73] E. Warburton, J. Olness, A. Nathan, J. Kolata, and J. McGrory, Phys. Rev. C **16** (1977).

[74] E. Norman, C. Davids, and C. Moss, Phys. Rev. C **18** (1978).

[75] D. Watson and H. Fortune, Nucl. Phys. **A448**, 221 (1986).

[76] A. N. Deacon, S. J. Freeman, R. V. F. Janssens, M. Honma, M. P. Carpenter, P. Chowdhury, T. Lauritsen, C. J. Lister, D. Seweryniak, J. F. Smith, et al., Phys. Rev. C **76**, 054303 (2007).

[77] E. Norman, C. Davids, M. Murphy, and R. Pardo, Phys. Rev. C **17** (1978).

[78] E. Runte, K. l. Gippert, W.-D. Schmidt-Ott, P. Tidemand-Petersson, L. Ziegeler, R. Kirchner, O. Klepper, P. Larsson, E. Roeckl, D. Schardt, et al., Nucl. Phys. **A441**, 237 (1985).

[79] S. Liddick, P. Mantica, B. Brown, M. Carpenter, A. Davies, M. Horoi, R. Janssens, A. Morton, W. Mueller, J. Pavan, et al., Phys. Rev. C **73** (2006).

[80] A. Wilson, C. Beausang, N. Amzal, D. Applebe, S. Asztalos, P. Butler, R. Clark, P. Fallon, and A. Macchiavelli, Eur. Phys. J. A **9**, 183 (2000).

[81] S. Lunardi, S. M. Lenzi, F. D. Vedova, E. Farnea, A. Gadea, N. Mărginean, D. Bazzacco, S. Beghini, P. G. Bizzeti, A. Bizzeti-Sona, et al., Phys. Rev. C **76**, 034303 (2007).

[82] R. Grzywacz, R. Béraud, C. Borcea, A. Emsallem, M. Glogowski, H. Grawe, D. Guillemaud-Mueller, M. Hjorth-Jensen, M. Houry, M. Lewitowicz, et al., Phys. Rev. Lett. **81**, 766 (1998).

[83] T. Pawłat, R. Broda, B. Fornal, W. Królas, D. Bazzacco, S. Lunardi, C. R. Alvarez, G. de Angelis, G. Maron, D. Napoli, et al., LNL Annual Report (1995).

[84] B. Fornal, IFJ Krakow Annual Report (1994).

[85] I. Matea, G. Georgiev, J. M. Daugas, M. Hass, G. Neyens, R. Astabatyan, L. T. Baby, D. L. Balabanski, G. Bélier, D. Borremans, et al., Phys. Rev. Lett. **93**, 142503 (2004).

[86] S. M. Lenzi, S. Lunardi, F. D. Vedova, N. M. Mărginean, A. Gadea, E. Farnea, D. R. Napoli, G. de Angelis, D. Bazzazzo, S. Beghini, et al., Legnaro National Laboratory 2006 Annual Report (2007).

[87] E. Runte, W.-D. Schmidt-Ott, P. Tidemand-Petersson, R. Kirchner, O. Klepper, W. Kurcewicz, E. Roeckl, N. Kaffrell, P. Peuser, K. Rykaczewski, et al., Nucl. Phys. **A399**, 163 (1983).

[88] L. Gaudefroy, O. Sorlin, C. Donzaud, J. C. Angélique, F. Azaiez, C. Bourgeois, V. Chiste, Z. Dlouhy, S. Grévy, D. Guillemaud-Mueller, et al., Eur. Phys. J. A **23**, 41 (2005).

[89] O. Sorlin, C. Donzaud, L. Axelsson, M. Belleguic, R. Béraud, C. Borcea, G. Canchel, E. Chabanat, J. M. Daugas, A. Emsallem, et al., Nucl. Phys. A. **660**, 3 (1999).

[90] I. Matea, Ph.D. thesis, Universite de Caen (2003).

[91] L. Gaudefroy, Ph.D. thesis, Universite Paris XI Orsay (2005).

[92] U. Bosch, W. D. Schmidt-Ott, P. Tidemand-Petersson, R. Runte, W. Hillebrandt, M. Lechle, F. K. Thielemann, R. Kirchner, O. Klepper, R. Roeckl, et al., Phys. Lett. **164B**, 22 (1985).

[93] M. Hannawald, Ph.D. thesis, Johannes Gutenberg-Universität in Mainz (2000).

[94] N. Hoteling, W. B. Walters, R. V. F. Janssens, R. Broda, M. P. Carpenter, B. Fornal, A. A. Hecht, M. Hjorth-Jensen, W. Królas, T. Lauritsen, et al., Phys. Rev. C **74**, 064313 (2006).

[95] K. L. Kratz and the ISOLDE Collaboration, private communication (2005).

[96] N. Vermeulen, S. K. Chamoli, J. M. Daugus, M. Hass, D. L. Balabanski, J. P. Delaroche, F. de Oliviera-Santos, G. Georgiev, M. Girod, G. Goldring, et al., Phys. Rev. C **75**, 051302(R) (2007).

[97] M. Honma, *private communication* (2006).

[98] T. Engeland, M. Hjorth-Jensen, A. Holt, and E. Osnes, Phys. Script. **T56**, 58 (1995).

[99] B. A. Brown, A. Etchegoyen, N. S. Godwin, W. D. M. Rae, W. A. Richter, W. E. Ormand, E. K. Warburton, J. S. Winfield, L. Zhao, and C. H. Zimmerman, *Oxbash for windows*, mSU-NSCL report number 1289.

[100] S. Zhu, A. N. Deacon, S. J. Freeman, R. V. F. Janssens, B. Fornal, M. Honma, F. R. Xu, R. Broda, I. R. Calderin, M. P. Carpenter, et al., Phys. Rev. C **74**, 064315 (2006).

[101] S. M. Lenzi, Legnaro National Laboratory 2007 Annual Report (2008).

[102] P. Adrich, A. M. Amthor, D. Bazin, M. D. Bowen, B. A. Brown, C. M. Campbell, J. M. Cook, A. Gade, D. Galaviz, T. Glasmacher, et al., Phys. Rev. C **77**, 054306 (2008).

[103] M. Hjorth-Jensen, *private communication* (2006).

[104] J. R. Stone, to be published (2007).

[105] T. Bengtsson and I. Ragnarsson, Nucl. Phys. **A436**, 14 (1985).

[106] I. Ragnarsson and R. K. Sheline, Phys. Scripta **29**, 385 (1984).

[107] P. Möller, J. R. Nix, W. D. Myers, and W. J. Swiatecki, At. Data Nucl. Dat. Tables **59**, 185 (1995).

[108] Y. Aboussir, J. M. Pearson, A. K. Dutta, and F. Tondeur, At. Data Nucl. Dat. Tables **61**, 127 (1995).

[109] G. A. Lalazissis, S. Raman, and P. Ring, At. Data Nucl. Dat. Tables **71**, 1 (1999).

[110] S. J. Freeman, R. V. F. Janssens, B. A. Brown, M. P. Carpenter, S. M. Fischer, N. J. Hammond, M. Honma, T. Lauritsen, C. J. Lister, T. L. Khoo, et al., Phys. Rev. C. **69**, 064301 (2004).

[111] G. de Angelis, *Presentation, fourth internation conference on fission and properties of neutron-rich nuclei* (2007).

[112] T. Kautzsch, W. Walters, M. Hannawald, K.-L. Kratz, V. Mishin, V. Fedoseyev, W. Bohmer, Y. Jading, P. V. Duppen, B. Pfeiffer, et al., Eur. Phys. J. A **9**, 291 (2000).

[113] B. Tomlin, Ph.D. thesis, Michigan State University (2006).

[114] A. Korgul, W. Urban, T. Rzaca-Urban, M. Rejmund, J. Durell, M. Leddy, M. Jones, W. Phillips, A. Smith, B. Varley, et al., Eur. Phys. J. A **7**, 167 (2000).

[115] W. T. Chou and E. K. Warburton, Phys. Rev. C **45**, 1720 (1992).

[116] J. Terasaki, J. Engel, W. Nazarewicz, and M. Stoitsov, Phys. Rev. C **66**, 054313 (2002).

[117] J. Terasaki, Nucl. Phys. **A746**, 583c (2004).

[118] I. Dillmann, K.-L. Kratz, A. Wöhr, O. Arndt, B. Brown, P. Hoff, M. Hjorth-Jensen, U. Köster, A. Ostrowski, B. Pfeiffer, et al., Phys. Rev. Lett. **91**, 162503 (2003).

[119] D. Morrissey, B. Sherrill, M. Steiner, A. Stolz, and I. Wiedenhöver, Nucl. Instrum. Methods Phys. Res. B **204**, 90 (2003).

[120] W. Walters, B. Tomlin, P. Mantica, B. Brown, J. R. Stone, A. Davies, A. Estrade, P. Hosmer, N. Hoteling, S. Liddick, et al., Phys. Rev. C **70**, 034314 (2004).

[121] J. Prisciandaro, A. Morton, and P. Mantica, Nucl. Instrum. Methods Phys. Res. A **505**, 140 (2003).

[122] W. Mueller, J. Church, T. Glasmacher, D. Gutknecht, G. Hackman, P. Hansen, Z. Hu, K. Miller, and P. Quirin, Nucl. Instrum. Methods Phys. Res. A **466**, 492 (2001).

[123] T. Kautszch, W. B. Walters, and K. L. Kratz, in *Nuclear Fission and Fission-Product Spectroscopy: Second International Workshop, AIP Conference Proceedings*, edited by G. Fioni, H. Faust, S. Obersted, and F. Hambsch (Seyssins, France, 1998), p. 183.

[124] T. Kautzsch, Ph.D. thesis, University of Mainz (2005).

[125] A. Scherillo, J. Genevey, J. Pinston, A. Covello, H. Faust, A. Gargano, R. Orlandi, G. Simpson, I. Tsekhanovich, and N. Warr, Phys. Rev. C **70**, 054318 (2004).

[126] B. A. Brown, *private communication* (2008).

[127] A. Jungclaus, L. Caceres, M. Gorska, M. Pfutzner, S. Pietri, E. Werner-Malento, H. Grawe, K. Langanke, G. Martinez-Pinedo, F. Nowacki, et al., Physical Review Letters **99**, 132501 (2007).

[128] R. Krüken, Prog. Nucl. Part. Phys. **59**, 321 (2007).

[129] R. Krüken, *Presentation, fourth international conference on fission and properties of neutron-rich nuclei* (2007).

[130] T. Kröll, Phys. of Atomic Nuclei **70**, 1369 (2007).

[131] N. Hoteling, W. B. Walters, B. E. Tomlin, P. F. Mantica, J. Pereira, A. Becerril, T. Fleckenstein, A. A. Hecht, G. Lorusso, M. Quinn, et al., Phys. Rev. C **76**, 044324 (2007).